UNIVERSITY OF CALIFORNIA

Los Angeles

System Performance and Cost Analyses of Sulfur-based Thermal Energy Storage

A dissertation submitted in partial satisfaction of the requirements for the degree Doctor of Philosophy in Mechanical Engineering

by

Yide Wang

ABSTRACT OF THE DISSERTATION

System Performance and Cost Analyses

of Sulfur-based

Thermal Energy Storage

By

Yide Wang

Doctor of Philosophy in Mechanical Engineering

University of California, Los Angeles, 2019

Professor Richard E. Wirz, Chair

Elemental sulfur is a promising storage material for low to high temperature thermal energy storage (TES) applications due to its high chemical stability, high heat transfer rate, and low cost. In this study, we investigate the performance of sulfur-based TES systems (SulfurTES) in the temperature range of 50-600 °C for single-tank and multi-tank configurations, as well as heat transfer fluid options, and have found a wide range of system configurations that provide attractive performance and cost.

For a single-tank thermal battery configuration, a 2D, transient-state numerical model was developed and validated using experimental results obtained from the thermal

cycling of a 10kWh SulfurTES battery. In general, the results show that a moderate shell aspect ratio (i.e., $L/D \sim 4-7$) and standard tube diameters (i.e., diameter $\sim 2-6$ ") can be used to provide a range of high performance and low-cost systems.

Multi-tank configurations were investigated and found to have many attractive aspects. The proposed cascaded configuration with two shell passes boosts system's energetic efficiency, providing a versatile system that accommodates wide selections of applications with low cost.

Effects of heat transfer fluid (HTF) properties on performance parameters were studied using sCO₂ and HITEC Solar salt as HTFs. The large density of sCO₂ leads to negligible compressor work that is beneficial to exergetic efficiency. High thermal conductivity and large energy density of HITEC salt provides promising thermal performance, but its prohibitive cost and limited operating temperature range make it undesirable to use with SulfurTES.

Finally, the cost analysis of SulfurTES system was conducted assuming integration with concentrated solar power plants. The results demonstrate significant cost advantage of SulfurTES over Molten-salt TES. The capital cost of SulfurTES achieves 2020 Sunshot TES cost target of \$15/kWh, providing a levelized cost of energy of less than ¢5/kWh that satisfies the Sunshot cost target of 2030.

The dissertation of Yide Wang is approved.

Adrienne G. Lavine

Laurent G. Pilon

Dante A. Simonetti

Richard E. Wirz, Committee Chair

University of California, Los Angeles

2019

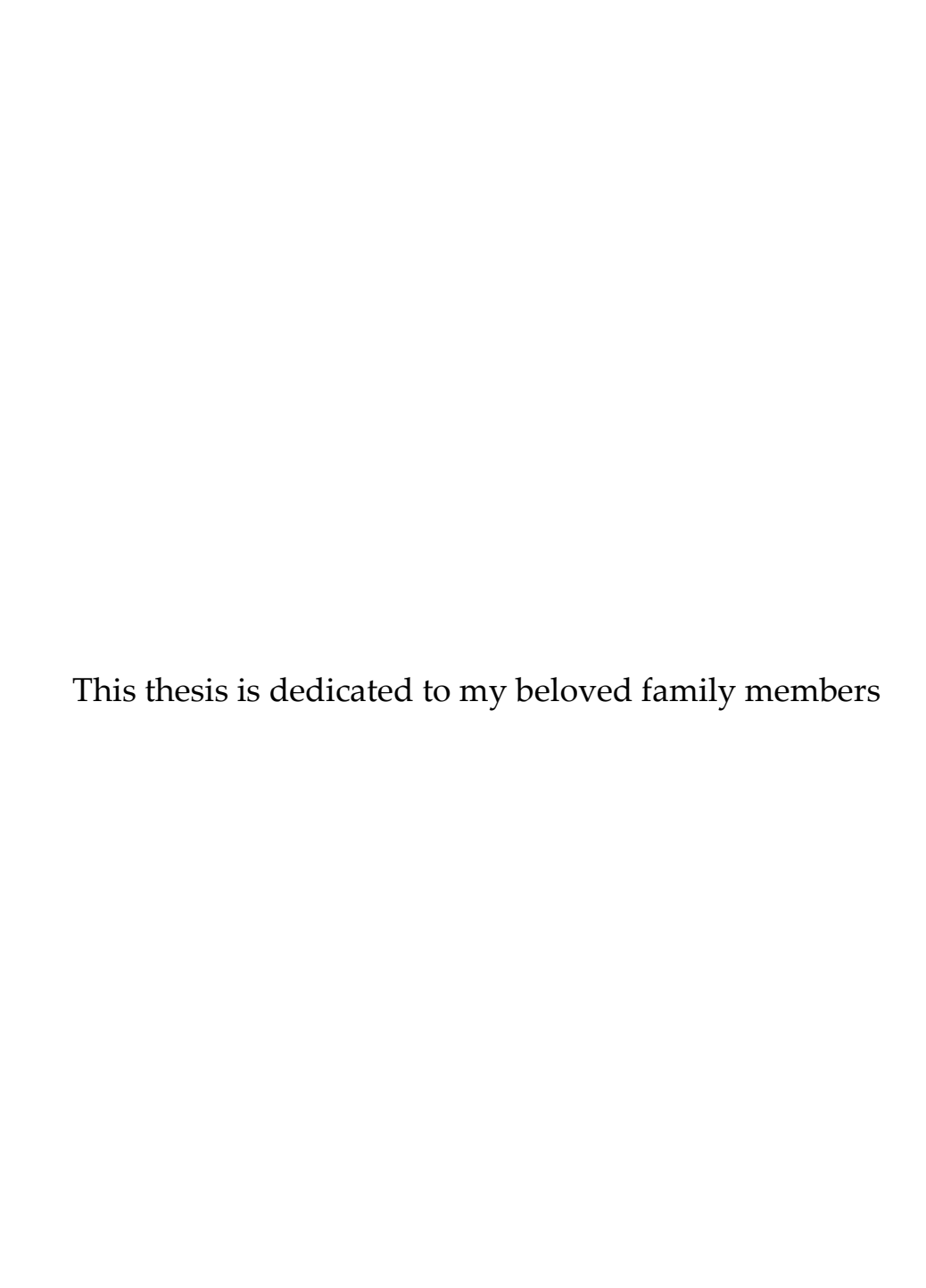


Table of Contents

ABSTRACT OF THE DISSERTATIONii
List of figuresx
List of tablesxvi
Nomenclaturexviii
Acknowledgementxxiii
Biographyxxiv
Chapter 1 Introduction1
1.1. Current TES applications and existing TES technologies
1.2. SulfurTES technology5
1.3. Thesis objective and tasks
1.4. Overview of dissertation
Chapter 2 Background
2.1. State-of-the-Art Thermal Energy Storage (TES)
Sensible heat storage
Latent heat storage

Thermochemical energy storage (TCES)
Cost comparison of current TES technologies
2.2. The SulfurTES Concept
Chemical characteristics of sulfur
Isochoric containment of sulfur
Sulfur heat transfer performance
SulfurTES demonstration
Summary of SulfurTES technology and the need for system performance analyses
34
2.3. System performance and cost analyses of sulfur-based thermal energy storage
2.3. System performance and cost analyses of sulfur-based thermal energy storage
2.3. System performance and cost analyses of sulfur-based thermal energy storage 35
 2.3. System performance and cost analyses of sulfur-based thermal energy storage 35 Chapter 3 System model for SulfurTES performance
2.3. System performance and cost analyses of sulfur-based thermal energy storage 35 Chapter 3 System model for SulfurTES performance

Sulfur side HTC	46
3.4. Thermal properties	51
3.5. Initial and boundary conditions	53
3.6. Time step and grid size dependency study	55
3.7. Model validation	58
Chapter 4 Performance characterization and design strategy of SulfurTES syst	tem 61
4.1. Parametric study of 1 MWh system	62
Performance characterization	65
4.2. System design strategy	77
System design procedure	78
Design space determination	79
4.3. Conclusions	84
Chapter 5 Performance enhancement considerations and cost analysis	87
5.1. System level performance with varying shell configuration	89
Two shell passes	89
Cascaded system	92

Design space variation by enhanced performance
5.2. System level performance with different HTFs
Comparison between air and sCO ₂ 102
Comparison between air and HITEC heat transfer salt
5.3. Cost analysis
Capital cost estimation of SulfurTES system
Levelized cost of energy (LCOE) with Two-tank SulfurTES
5.4. Conclusion
Chapter 6 Conclusions and future study136
Appendix A: Conductive heat transfer coefficient of sulfur conduction
Appendix B: Example usage of system design procedure
Appendix C: Preliminary experimental investigation on performance of lab-scale
SulfurTES thermal battery
Appendix D: On-sun pilot demonstration of SulfurTES system
References

List of figures

FIGURE 1 - SULFURTES SYSTEM WITH APPLICATIONS
FIGURE 2 - SUPPLY AND DEMAND CURVE OF CSP PLANT [1]
FIGURE 3 - TWO-TANK MOLTEN-SALT TES SYSTEM [2]
Figure 4 – Sulfur pile from oil refinement
FIGURE 5 - PACKED BED TES SYSTEM [12]
FIGURE 6 - MACRO-ENCAPSULATED PCM TES SYSTEM [6]
Figure 7 - Ammonia-based TCES system [28]
FIGURE 8 - PRELIMINARY COST COMPARISON BETWEEN DIFFERENT TYPES OF TES SYSTEMS 21
FIGURE 9 - SPECIES CONCENTRATION VARIATION WITH TEMPERATURE [3]
FIGURE 10 - SULFUR VISCOSITY VARIATION WITH TEMPERATURE [31]
FIGURE 11 - SULFUR THERMOPHYSICAL PROPERTY VARIATION WITH TEMPERATURE [30]
FIGURE 12 - APPARATUS OF SULFUR COMPATIBILITY TEST [32]
FIGURE 13 - SULFUR PRESSURE-TEMPERATURE RELATIONSHIP IN ISOCHORIC CONTAINMENT [32]. 28
Figure 14 - Energy storage capacity distribution for sulfur [33]
FIGURE 15 – COMPUTATIONAL DOMAIN OF ISOCHORIC SULFUR CONTAINMENT [34]
Figure 16 - Temperature and velocity distribution during charge/discharge [34] 31
FIGURE 17 - AVERAGE NUSSELT NUMBER WITH CORRESPONDING RAYLEIGH NUMBER [34] 32

FIGURE 18 - LAB-SCALE SULFURTES DEMONSTRATION SYSTEM [35]	. 33
Figure 19 - Pilot scale SulfurTES demonstration system with CSP-dish collector [[33]
	. 33
FIGURE 20 - (A) SULFURTES SYSTEM (B) CONFIGURATION CROSS-SECTIONAL VIEW	. 40
Figure 21 - HTF flow path (e.g., during charging)	. 41
Figure 22- (a) Area-averaged sulfur temperature, (b) corresponding liquid fract	ION
[50]	. 48
FIGURE 23 - THE COMPARISON OF INTEGRATED CORRELATIONS WITH ORIGINAL CORRELATIONS	FOR
(A) CHARGE (B) DISCHARGE OPERATION	. 50
Figure 24 - (a) Liquid fraction and (b) corresponding dimensionless energy content [[50]
	. 52
FIGURE 25 - SYSTEM DISCRETIZATION WITH COORDINATE	. 56
Figure 26 - HTF outlet temperature of the system with varying number of (a) ax	⟨IAL
NODES (B) RADIAL DISCRETIZED NODES	. 56
Figure 27 - Tube temperature distribution at three time instances with varying t	ΊΜΕ
STEP	. 57
FIGURE 28 - LOCATIONS OF TUBE TEMPERATURE MEASUREMENTS ALONG THE AXIS	58
FIGURE 29 - COMPARISON BETWEEN PREDICTED AND MEASURED TUBE TEMPERATURE	59

Figure 30 - Charge utilization for (a) $D_0 = 0.06$ m, (b) $D_0 = 0.114$ m, (c) $D_0 = 0.168$ m and
STORAGE CAPACITY UTILIZATION FOR (D) $D_O = 0.06 \text{ m}$, (E) $D_O = 0.114 \text{ m}$, (F) $D_O = 0.168 \text{ m}$ with
Varying $m *$ 67
Figure 31 - Discharge utilization for (a) do = 0.06 m, (b) do = 0.114 m, (c) do = 0.168 m with
Varying $m *$
Figure 32 – Roundtrip energetic efficiency for (a) D_0 = 0.06 m, (b) D_0 = 0.114 m, (c) D_0 = 0.168
M WITH VARYING $m*$
Figure 33 - Charge exergetic efficiency with varying $m * \text{for (a)} \ D_0 = 0.06 \ \text{m}$, (b) $D_0 = 0.06 \ \text{m}$
$0.114M, (C) D_0 = 0.168 M.$
Figure 34 - Discharge exergetic efficiency for different system configurations with (a)
$D_O = 0.06 \text{ M}$ AND AR = 2.5 (B) $D_O = 0.06 \text{ M}$ AND AR = 9 (C) $D_O = 0.114 \text{ M}$ AND AR = 2.5 (D) $D_O = 0.06 \text{ M}$
= 0.114 m and AR = 9 (E) D_0 = 0.168 m and AR = 2.5 (F) D_0 = 0.168 m and AR = 9 with
VARYING MASS FLOW RATE
FIGURE 35 - FLOW CHART OF SYSTEM DESIGN PROCEDURE
Figure 36 - Storage capacity utilization for systems with $D_{O} = 0.06$ under varying mass
FLOW RATE
Figure 37 - (a) Charge Utilization, (b) Charge exergetic efficiency, (c) Roundtrip
EFFICIENCY FOR SYSTEMS WITH $D_o = 0.06$ m under varying mass flow rate
Figure 38 - Discharge exergetic efficiency of systems with $D_0 = 0.06$ m at 8 hours into
DISCHARGING UNDER VARYING MASS FLOW RATE

Figure 39 - Determined design space unique to performance requirements
Figure 40 - Design space determined for system with large tubes (D_0 =0.168 m)
Figure 41 - Charging flow path of (a) single shell pass (b) two shell passes 90
Figure 42 - Equivalent shell geometry change by having two shell passes
FIGURE 43 - COMPARISON OF (A) HEAT TRANSFER COEFFICIENT (B) CHARGE UTILIZATION BETWEEN
SYSTEMS WITH SINGLE AND TWO SHELL PASSES
FIGURE 44 - CHARGING FLOW PATH OF (A) TWO-SHELL PASS ONE TANK SYSTEM (B) TWO-SHELL PASS
CASCADED SYSTEM93
Figure 45 - Energy content in hot/cold tanks with energy loss of cascaded system
During (a) charging (b) discharging at $m *= 1$ for systems with shell AR from 2.5
то 7
Figure 46 - (a) Charge utilization and (b) roundtrip efficiency comparison between one-
TANK SYSTEM AND CASCADED SYSTEM
Figure 47 - Comparison of (a) compressor work (b) charge exergetic efficiency between
SYSTEMS WITH SINGLE AND TWO SHELL PASSES
Figure 48 – Comparison of updated design space with the original one based on
ENHANCED PERFORMANCE FOR SYSTEMS WITH LARGE TUBES (D_0 =0.168 m)
Figure 49 - Design space of updated performance requirements for systems with large
TUBES (D_0 =0.168 M)

FIGURE 50 - TEMPERATURE-ENTROPY DIAGRAM OF SCO ₂ BRAYTON CYCLE [63]
FIGURE 51 - SCO ₂ THERMOPHYSICAL PROPERTIES AT 20 MPA [50]
Figure 52 - Comparison of (a) shell side heat transfer coefficient during charging (b)
CHARGE UTILIZATION (C) DISCHARGE UTILIZATION WITH SCO_2 AND AIR AS HTFs 106
FIGURE 53 - SCHEMATIC OF ENERGY TRANSFER BETWEEN HTF AND TUBE
Figure 54 – Specific work of Isentropic Compression of Real gas with Corresponding
COMPRESSION RATIO [61]
Figure 55 - Comparison of Charge exergetic efficiency between air and sCO_2
FIGURE 56 - COMPARISON OF SHELL SIDE HEAT TRANSFER COEFFICIENT DURING CHARGING BETWEEN
AIR AND HITEC SALT FOR SYSTEMS WITH (A) AR=2.5 (B) AR=7
FIGURE 57 - COMPARISON OF CHARGE UTILIZATION AND AMOUNT OF ENERGY STORED BETWEEN AIR
AND HITEC SALT FOR SYSTEMS WITH (A) AR=2.5 (B) AR=7
Figure 58 – Comparison of axial temperature distribution within HTFs at the end of
Charging for systems with (a) AR= 2.5 (b) AR= 7 between air and HITEC salt 114
Figure 59 – Comparison of energy distribution within system at the end of charging
WITH $m *= 1$ BETWEEN AIR AND HITEC SALT
Figure 60 – Gross electricity output from power block with corresponding turbine
INLET TEMPERATURE AND AMOUNT OF INPUT THERMAL ENERGY [73]

FIGURE 61 – CAPITAL COSTS OF SINGLE-TANK SULFURIES SYSTEMS INTEGRATED WITH CSP-
POWER TOWER AND TROUGH PLANT
Figure 62 - (a) Capital cost comparison between systems using air and HITEC salt as
HTFs (B) Cost distribution within system and HTF
FIGURE 63 - CONCEPTUAL TWO-TANK SULFURTES SYSTEM
Figure 64 - Tank Thickness of Two-tank SulfurTES systems with varying storage
CAPACITY
FIGURE 65 - CAPITAL COST OF TWO-TANK SULFURTES SYSTEMS WITH VARYING STORAGE CAPACITY
Figure 66 - Capital Cost Comparison between Single-Tank/Two-Tank SulfurTES and
MOLTEN-SALT TES SYSTEMS WITH (A) PARABOLIC TROUGH PLANT ($250-550^{ m o}{ m C}$) (B) SOLAR
POWER TOWER (250 – 650 °C)
FIGURE 67 – COMPARISON OF LCOE OF (A) TROUGH PLANT (B) POWER TOWER WITH 12-HOUR TWO-
TANK SULFURTES AND MOLTEN-SALT TES SYSTEMS

List of tables

TABLE 1: THERMAL PROPERTIES OF HTF (AIR)
TABLE 2: THERMAL PROPERTIES OF SULFUR
TABLE 3: VARIED DESIGN PARAMETERS OF SULFURTES BATTERY
TABLE 4: CONSTANT DESIGN PARAMETERS OF SULFURTES BATTERY
TABLE 5: NON-DIMENSIONAL PARAMETERS OF SULFUR SIDE AND SHELL SIDE HEAT TRANSFER 65
TABLE 6: EXAMPLE SET OF PERFORMANCE REQUIREMENTS
Table 7 – Comparison of Hoop and yield stress by sulfur vapor pressure at $600^{\circ}\mathrm{C}$ 94
TABLE 8: TUBE SURFACE AREA COMPARISON BETWEEN ONE-TANK AND CASCADED TANKS 96
Table 9: Updated performance requirements
TABLE 10: THERMAL PROPERTIES OF HTF (SCO ₂)
TABLE 11: THERMAL PROPERTIES OF HTF (HITEC SALT [71])
Table 12: Turbine thermal to electric energy conversion efficiency
TABLE 13: OPERATING TEMPERATURE RANGES AND CONVERSION EFFICIENCIES OF SULFURTES
SYSTEMS IN SINGLE/TWO-TANK CONFIGURATIONS FOR CSP-TROUGH AND CSP-POWER TOWER
Table 14: Storage capacities determined for selected plant capacities
TABLE 15: COMPONENT PRICE OF SINGLE-TANK SULFURTES

TABLE 16: STORAGE CAPACITY COMPARISON USING HITEC SALT AND AIR AS HTF FOR TROUGH
PLANT
TABLE 17: TANK GEOMETRY OF SYSTEMS WITH SELECTED PLANT CAPACITIES
TABLE 18: COMPONENT PRICE OF TWO-TANK SULFURTES SYSTEM

Nomenclature

C_p	Specific heat [J/kg-K]
D	Diameter of shell [m]
d	Diameter of steel tube [m]
Bs	Baffle spacing [m]
Bc	Baffle cut [%]
P_t	Tube pitch [m]
P_r	Tube pitch ratio
I	Pressure drop correction factor
J	Heat transfer coefficient correction factor
j	Colbern factor
S_m	Crossflow area across shell centerline [m ²]
S_w	Crossflow area through one baffle window [m²]
N	Number of
8	Gravitational acceleration [m/s²]
h	Heat transfer coefficient [W/m²-K]
k	Thermal conductivity [W/m-K]
L	Length [m]
l	Latent heat of solid-liquid phase change [J/kg]
P	Pressure [Pa]

m Mass [kg]

n Number of grids

A Cross-sectional area [m²]

V Volume [m³]

Rayleigh number

Re Reynolds number

Nu Nusselt number

Pr Prandtl number

R Radius of the tube [m]

Time [s]

Temperature [°C]

*T** Non-dimensional temperature

v Axial velocity [m/s]

z Axis of axial coordinate

j Axial coordinate

i Time step

r Axis of radial coordinate

Q Storage capacity [kWh]

*Q** Non-dimensional energy content

AR Aspect ratio

 \dot{m} Mass flow rate [kg/s]

xix

 \dot{m}^* Non-dimensional mass flow rate

U Utilization [%]

W Compressor work [J]

C Cost [\$]

LCOE Levelized Cost of Energy [C/kWh]

Subscripts and Superscripts

o Outer

i Inner, or initial

s Sulfur

t Tube

f Heat transfer fluid

c Crossflow

cr Cross-sectional

w Baffle window

e Entrance/Exist

b Baffle

tc Tube rows between baffle tips

tcw Tube rows between baffle window

ins Insulation

sh Shell

I Ideal

C Charge

D Discharge

s-l Solid-liquid

eff Effective

NC Natural convection

rad Radiation

H Horizontal

V Vertical

ref Reference

#-pass Number of shell passes

Greek Letters

 α Thermal diffusivity [m²/s]

 β Thermal expansion coefficient [1/K]

μ Viscosity [Pa-s]

 δ Viscosity correction factor

 ρ Density [kg/m³]

 γ Liquid fraction

Emissivity

 σ Stefan-Boltzmann constant [W/m²/K⁴]

xxi

 θ Tube layout (deg angle)

 η Compressor efficiency

Acronyms

CSP Concentrated solar power

CHP Combined heat and power

PCM Phase-change material

NPS Nominal pipe size

OD Outer diameter

TES Thermal energy storage

HTF Heat transfer fluid

DOE Department of Energy

TEMA Tubular Exchanger Manufacturers Association, Inc.

Acknowledgement

My strongest gratefulness to many wonderful people that helped me with this thesis and other important achievements during my Ph.D. life. Firstly, I sincerely appreciate the help from my advisor, Prof. Richard Wirz, who endeavored endless effort in guiding my way to knowledge and preparing me for real-world challenges. His patience and wisdom of life changed me from a child to a man who is ready to take on the real world. What he taught me was not only knowledge, but also the method and mindset to obtain knowledge myself, and to finish tasks professionally. With his help, I'm ready to be out there and change a small piece of the world to the greatest extent of my ability.

I would also like to thank Prof. Adrienne, Prof. Laurent Pilon, and Prof. Dante Simonetti for serving on my doctoral committee and providing constructive comments on my thesis. Moreover, I must say thanks to Dr. Amey Barde, Dr. Karthik Nithyanandam, Dr. Zhitong Chen, Kaiyuan Jin, Siddhesh Naik, Parker Wells, as well as the entire plasma and propulsion group, for providing me suggestions or even solutions to numerous problems. Last but not least, I would like to thank my family members. Their love and encouragement drive me forward and become a better person. To all the people who have ever helped me, please remember, rock never dies, let's keep on rolling!

Biography

Prior to the current Ph.D. degree, Yide Wang obtained his bachelor's degree in mechanical engineering from Purdue University in the year of 2015. He then joined University of California, Los Angeles for a master's degree in mechanical engineering, focused on research related to power consumption and heat transfer characterization of piezoelectric fan cooling, under the guidance of Professor Yongho Sungtaek Ju. After completing his master's degree, he joined the Wirz Research Group's to do his Ph.D. research in the UCLA Energy Innovation Laboratory under the guidance of Professor Richard Wirz.

Chapter 1 Introduction

Thermal energy storage (TES) system bridges the gap between thermal energy supply and demand by providing dispatchability and stability to intermittent energy sources including renewable energy and excessive thermal energy generation from industrial applications. TES system stores heat when extra amount of thermal energy is available and provides power to thermal loads to enable a continuous power generation. Successful implementation of TES systems into concentrated solar power (CSP) plants enables Rankine electricity generation during times of intermittency. Investigations on coupling TES system with combined heat and power (CHP) system demonstrate improved plant performance with a boost in energy conversion efficiency, and a reduction in system cost. Previous studies show that, with high-temperature stability and low cost, elemental sulfur serves as a promising storage medium. However, understanding of performance and cost characteristics of sulfur-based TES systems (SulfurTES) is still limited. Therefore, a comprehensive investigation is necessary in advising future design of industrial-scaled applications of SulfurTES systems.

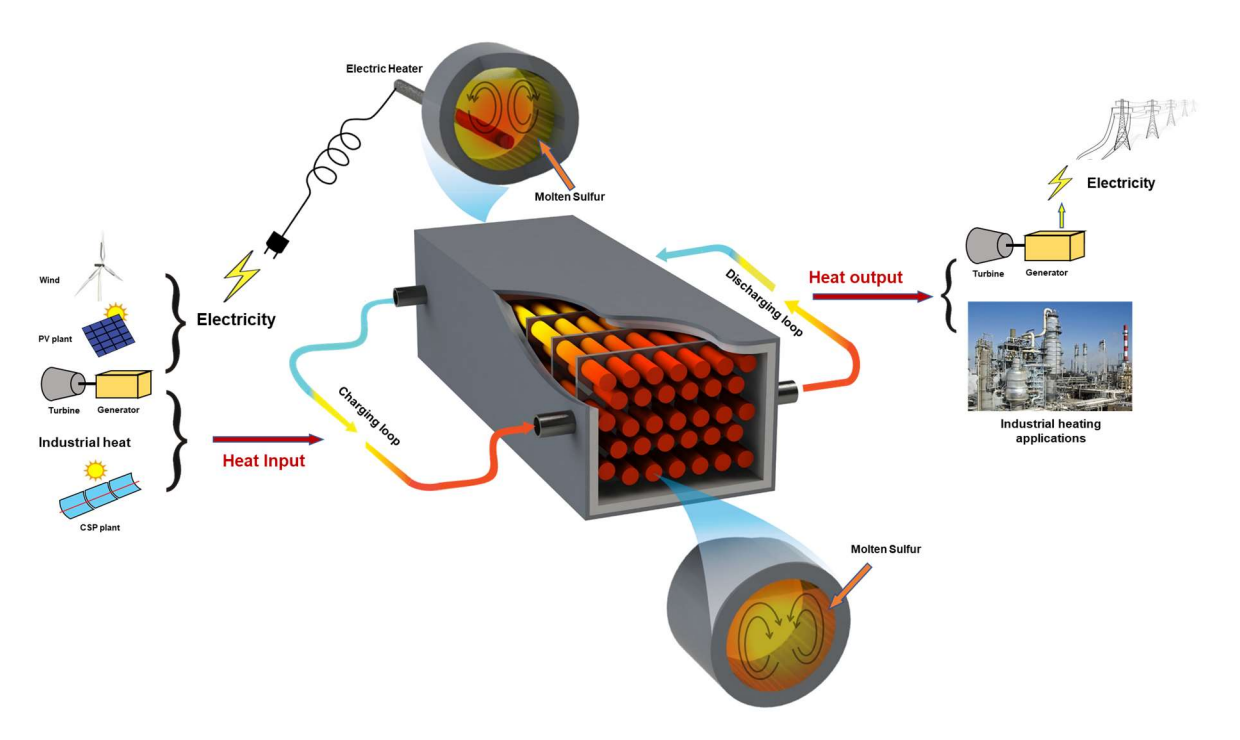


Figure 1 - SulfurTES system with applications

This chapter provides motivation of this dissertation by identifying advantages of SulfurTES system over the state-of-the-art TES systems and the need of further investigation on system level performance and cost. Section 1.1 presents current applications of TES systems with existing technologies in thermal energy storage. Section 1.2 discusses SulfurTES technology with its benefits and challenges. Section 1.3 presents the main objective of this study and tasks that compose the pathway to achieve the objective. Section 1.4 provides an overview of the dissertation and illustrates how each task work coherently to help obtain the understanding of performance and cost of SulfurTES systems.

1.1. Current TES applications and existing TES technologies

Recent deployment of power generation with renewable energy draws tremendous amount of attention in academic researches and industrial applications. One of the major applications of TES system is in CSP plant. Unlike traditional power plant driven by fossil fuel, CSP plant obtains heat from solar energy, and generates electricity by Rankine steam turbine. Due to intermittency of solar energy, TES system is integrated to store heat during peak energy supply hours (10 AM to 3 PM) and to provide grid stability during peak electricity demand hours (5 PM to 9 PM). Another application of TES system is in CHP plant where exhaust heat from fossil fuel power generation is recycled for heating applications, such as residential heating. Clearly, implementation of TES into CHP plant adds flexibility to the energy utilization, and benefits to the overall energy efficiency and economics.

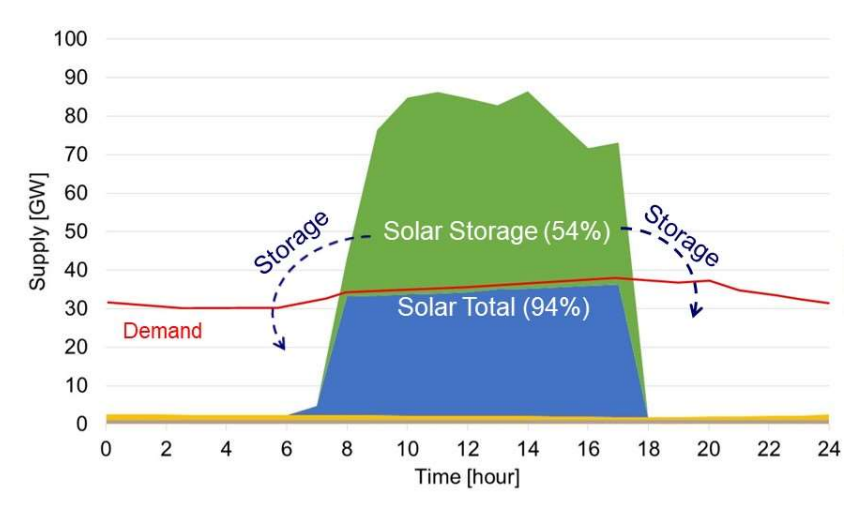


Figure 2 - Supply and demand curve of CSP plant [1]

The state-of-the-art TES system utilizes molten salt as storage medium to store energy in the form of sensible heat. The system consists of a hot and a cold storage tank, shown in Figure 3. During charging, cold molten salt is pumped out from the cold tank, absorb heat from energy source, and is stored at the hot tank. The flow path is reversed during discharging where all thermal energy is extracted and supplied to the thermal load. Current research efforts have also focused on storing thermal energy as latent heat and chemical energy. Details can be found in the next chapter.

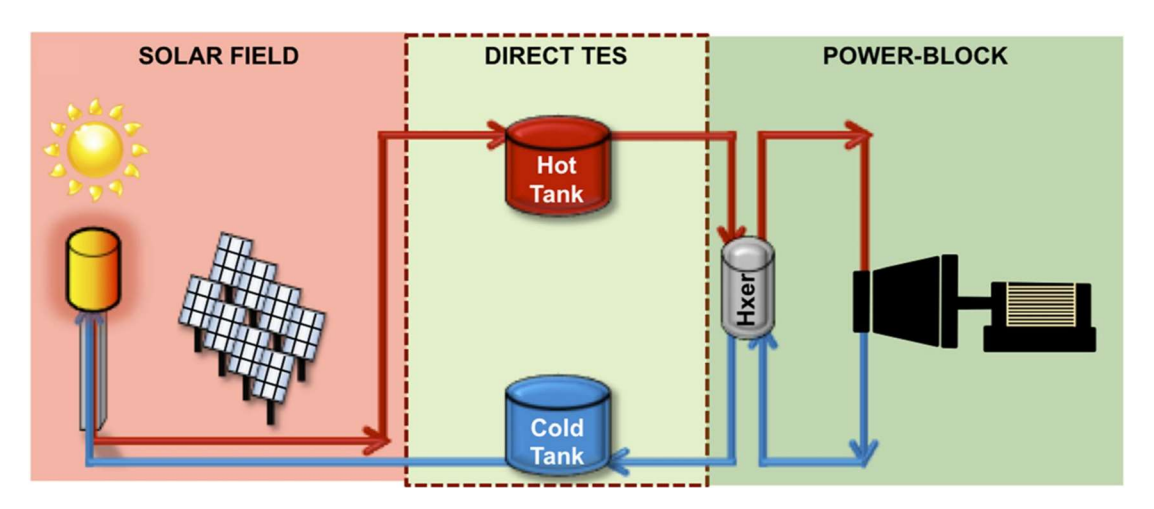


Figure 3 - Two-tank molten-salt TES system [2]

1.2. SulfurTES technology

UCLA researchers proposed and presented promising features of sulfur as storage medium. As an elemental material, sulfur has very good thermal stability, and can withstand up to 1000 °C [3] without thermal degradation. Furthermore, due to its abundant reserve on this planet, and its presence as a biproduct of petroleum refinement process, sulfur is extremely cheap, costing around \$0.04-0.1/kg[4], whereas the price of molten salt is in the range of \$1/kg [5].



Figure 4 – sulfur pile from oil refinement

The proposed SulfurTES system is in a single-tank, thermal battery configuration where sulfur is isochorically contained in a bundle of tubes. Analogues to shell-and-tube heat exchanger, the tube bundle is enclosed by a shell, so that the heat transfer fluid (HTF) can flow along the tube bundle to provide or extract heat from sulfur. The group studied heat transfer behavior of sulfur in isochoric containment. The study provides Nusselt number correlation to determine heat transfer coefficient and confirms sulfur's fast

thermal responsiveness that is 3-14 times faster than conduction. A pilot scale system is designed and fabricated in house with 30-kWh storage capacity. The on-sun demonstration of the pilot system successfully proves the feasibility of capturing solar thermal energy at high temperature within the desired time frame. All previous works show low-cost and high-performance characteristics of SulfurTES in component level with pilot scale demonstration. An urging demand of confirming those characteristics in industrial scales (commercial and utility scales) draws research focus and is discussed in this thesis.

1.3. Thesis objective and tasks

The objective of this thesis is to numerically investigate the performance of large-scale SulfurTES thermal battery in a systematic approach within a comprehensive parametric space, establish basis for industrial-scale SulfurTES system design, propose methods in performance enhancement, and estimate both capital cost and levelized cost of energy (LCOE) based on the system level performance.

The following tasks are completed in order to achieve the main objective:

 Develop an experimentally validated 2D numerical system model with short run time to enable a comprehensive parametric study with broad geometric parameters and operation conditions.

- Perform a parametric study on a 1-MWh system to observe change in system level performance with varying geometric parameters and operating conditions.
- Suggest a design procedure considering unique user desired performance metrics
- Discuss additional performance considerations with multiple shell passes,
 cascaded configuration, and various heat transfer fluids.
- Estimate capital cost of SulfurTES system and LCOE, assuming integrating with CSP trough plant and CSP power tower.

1.4. Overview of dissertation

Chapter 2 of the dissertation introduces background associated with existing TES technologies and provide a more in-depth discussion on characteristics of elemental sulfur as storage medium. In addition, previous efforts in modeling and performance characterization of TES system is discussed.

Chapter 3 presents the development of 2D system model. Section 3.1-3.2 describes the modeled system, provides assumptions and associated coupled energy equations for each system component. Implemented heat transfer coefficients and thermal properties on both HTF side and sulfur side are presented in section 3.3-3.4. Section 3.5 lists

boundary and initial conditions of the system. Section 3.6 introduces a time step and grid size independent study. Lastly in chapter 3, the model is validated comparing predicted tube temperature at various axial locations with experimental measurements and is shown in section 3.7.

A parametric study on a 1-MWh system and an iterative system design procedure are discussed in chapter 4. Section 4.1 listed parametric space of system geometry and operating conditions. Performance variation of SulfurTES systems within the parametric space is also observed and demonstrated in this section. An iterative system design procedure that helps identify appropriate system geometry and operating condition based on a design space unique to user defined performance requirements is documented in section 4.2. This section articulates the design procedure by a flow chart and presents the determination of the input design space based on example performance metrics.

Chapter 5 discusses performance variation with multiple shell-passes, cascaded configuration and various heat transfer fluids. The effective change in the system geometry by having 2 shell passes and the addition to heat transfer area from cascaded configuration with corresponding performance enhancement are documented in section 5.1. Comparison between system level performances using air, sCO₂ and HITEC solar salt as HTF is introduced in section 5.2. Estimation of capital system cost with storage capacity ranging from 10 MWh to 3 GWh is discussed in section 5.3. LCOE is also estimated by

integrating SulfurTES systems, whose storage capacity fall in the above-mentioned capacity range, with CSP-trough plant and CSP power tower.

Chapter 6 concludes the thesis with key findings from performance characterization and cost estimation of SulfurTES system. The future efforts will focus more on effects of axial convection inside sulfur tube and effects of system orientation on system level performance.

Chapter 2 Background

This chapter discusses existing technologies for thermal energy storage in a more indepth and scientific perspective. Section 2.1 introduces three types of heat storage mechanisms and associated storage media with their advantages and limitations. Section 2.2 introduces characteristics of sulfur as storage medium including pressure-temperature characteristics and corrosion behavior with containment material. Previous efforts on sulfur heat transfer behavior and laboratory-scale system demonstration are presented in this section as well. Following the discussion on SulfurTES technology, this chapter is concluded by a literature review on modeling of TES systems and system level performance investigations.

2.1. State-of-the-Art Thermal Energy Storage (TES)

A desired TES system should be able to have fast thermal responsiveness, high energetic and exergetic efficiency with low system cost. A fast thermal responsiveness ensures adequate storage capacity utilization within a limited time period, as renewable energy sources are intermittent. The determining factor of thermal responsiveness is the heat transfer coefficient of storage medium. Ideally, the heat transfer rate within the storage medium should be high enough to transfer heat from outer surface to bulk volume in a short period of time. It maintains the temperature difference between outer

storage medium surface and heat source, allowing a continuous and steady heat transfer process that provides a high thermal responsiveness.

Energetic efficiency or roundtrip efficiency, defined as energy recovered from TES by energy supplied from source, is an important performance criterion for TES system design. High energetic efficiency indicates that the energy supplied is approaching fully utilized without significant amount of energy waste. However, the quality of energy that is recovered from TES system is also important, as it determines the usefulness of energy, and is presented as exergetic efficiency. A simplified expression of exergy is written as:

$$\Xi = H(1 - \frac{T_0}{T}) \tag{1}$$

where H is the amount of enthalpy the storage medium possess, T is the temperature of the storage medium and T_o is the reference temperature. Clearly, the energy is more useful with higher temperature. Therefore, TES system with high exergetic efficiency, expressed as:

$$\phi = \frac{\Xi_{out}}{\Xi_{in}} = \frac{H_{out}(1 - \frac{T_o}{T_{out}})}{H_{in}(1 - \frac{T_o}{T_{in}})}$$
(2)

provides recovered energy with temperature as close as possible to that of supplied energy, maintaining the usefulness of energy.

The capital cost of TES system is determined by costs of storage medium, containment, and parasitic components such as pumps, pipes, insulation and foundation.

Research efforts are mainly focused on finding suitable storage media that not only have good heat transfer performance, but also are cheap, less corrosive, and have large energy density to reduce containment cost.

Based on desired TES characteristics discussed above, three types of thermal energy storage techniques are available by utilizing: sensible heat, latent heat or thermochemical energy of storage media.

Sensible heat storage

The state-of-the-art molten-salt TES is one application of sensible TES system, where thermal energy is stored as change in the temperature, expressed as:

$$E = \int_{T_i}^{T_f} m c_p dT \tag{3}$$

where T_f is final temperature and T_i is initial temperature for the thermal charging process. m and c_p is the total mass and specific heat of storage the medium respectively. Clearly, based on Eqn. (3), the specific heat and the allowable operating temperature range determine the energy storage capacity. Therefore, for a fixed storage capacity, less amount of storage medium is needed with higher specific heat and larger operating temperature range, reducing the storage medium cost and containment cost. The commonly used molten nitrite salt (Solar SaltTM) is a mixer of 60% NaNO3 and 40% KNO3 with specific heat around 1.5 kJ/kgK and operating temperature range between 290 to 565

°C [6]. Although Solar Salt™ is able to reach 600 °C without chemically decomposing, the highest operating temperature is limited to 565 °C to avoid corrosion with steel container. The lower temperature limit is kept at 290 °C to provide a safety margin from freezing point of 220 °C. Extensive research efforts on varying chemical compositions of molten salts to enlarge the temperature range have been found. Raade et al. [10] reported the experimental finding of a quinary molten salt composition with a melting temperature as low as 65°C and thermally stable above 500 °C. They also found a quinary composition of LiCl, NaCl, KCl, CsCl and SrCl2 with a melting point of 253 °C at ambient pressure with thermal stability up to approximately 750 °C. However, one major limitation of Solar Salt™ is its prohibitively high price, about \$1/kg or \$10/kWh [5], let alone the considerably higher prices of newly developed molten salts.

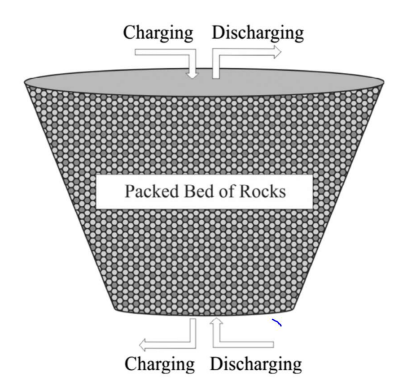


Figure 5 - Packed bed TES system [12]

Considering draw backs of molten salt, small temperature range and high cost, extensive investigations have been conducting on packed bed TES systems, exploiting

sensible heat of rocks with large density, large allowable temperature range and low cost (\$0.05-0.35/lb) [11,12,13,14]. For instance, Magnesia fire bricks has an upper temperature limit of 1200 °C with a density of 3000 kg/m³ and specific heat of 1.15 kJ/kgK, providing large energy density. However, the major challenge associated with TES systems using solid storage media is their slow thermal responsiveness that leads to reduced energy efficiency. Although, forced convection governs the heat transfer between HTF and storage rocks, heat transfer within rocks is conduction only. The surface of storage rock will be easily heated up by HTF, as heat is transferred into inner rock body relatively slowly, reducing temperature difference between HTF and storage medium, and loosing potential of further energy transfer that causes energy waste with reduced energy efficiency. To over come the drawback of reduced energy efficiency, overdesigning the system is one solution that provides large enough area to allow a complete energy transfer into the system. Zanganeh et al. [13] proved this concept by implementing an overdesigned packed bed system for an industrial process heat application. The system with 7.2 GWh of storage capacity undergone 30 thermal cycles between 150-650 °C, utilizing around 8% of storage capacity to ensure around 100% energy efficiency. However, the author dose not discuss the cost associated with an 1250% overdesigned system, leaving doubts on the appropriateness of such significant overdesign. Other researchers considered system cost of concrete-based TES systems. Laing et al [7]

estimated the cost for a 1-GWh system to be around \$38/kWh, while others from ENERGIE Program in European Commission proposed their next generation concrete-based technology with a cost of around \$26/kWh. To date, none of the existing solid-based TES system satisfy the 2020 Sunshot TES cost target of \$15/kWh [8].

The development of one-tank thermocline TES, where both hot and cold molten-salt is stored in the same tank with a filler bed of rocks, has been advanced in recent studies [15,16]. Thermal stratification maintains in the storage tank by buoyancy driven force from density difference, where hot salt stays on top of cold salt. Filler rock bed is added to reduce the amount of molten-salt usage with reduced system cost. Yang et al. [15] showed that the system cost of thermocline TES is 35% lower than the two-tank TES.

Latent heat storage

Latent heat TES system uses phase change materials (PCMs) as storage medium. It operates at temperature near the solid-liquid phase changing point of storage material where the majority of thermal energy is stored in the form of latent heat. The energy stored is calculated as:

$$E = \int_{T_i}^{T_{pc}} mc_{p,1} dT + m\Delta h_l + \int_{T_{pc}}^{T_f} mc_{p,2} dT$$
 (4)

where T_{pc} is the phase change temperature. $c_{p,1}$ and $c_{p,2}$ are the specific heat of the material in solid and liquid phase, respectively. Δh_l is the latent heat of the material. The

main advantage of latent heat TES over sensible heat TES is its ability to operate within a small temperature range near melting point [6]. The storage medium can stay at constant temperature as phase changing proceeds.

Phase-change materials are categorized into three major types: organic, inorganic and eutectic. Organic PCMs (paraffin compounds, fatty acid, etc.) are non-corrosive, no undercooling, and chemically and thermally stable, but suffers from lower latent heat and lower conductivity compared to other types of PCMs [17,18]. Inorganic PCMs (Salt hydrate, Metallics) provides higher latent heat compared to organic PCMs, but corrosion issue, phase separation and low thermal stability limit its utilization in industrial applications [17,19]. Eutectic materials are a combination of two or more low melting materials with similar melting and freezing points. Conductivity is usually high for eutectic materials, and the melting point can be varied by varying weight percentage of each material [20,21].

Special considerations in containment of PCMs are also critical. Proper containment of PCMs helps prevent possible chemical composition variation by interacting with surroundings and provide sufficient surface area for heat transfer. Macro-encapsulation is commonly used where storage materials are contained in tubes, spheres, panels, etc. Capsules are placed in a tank where HTF is passed into the tank and flow across capsules to transfer heat, shown in Figure 6.

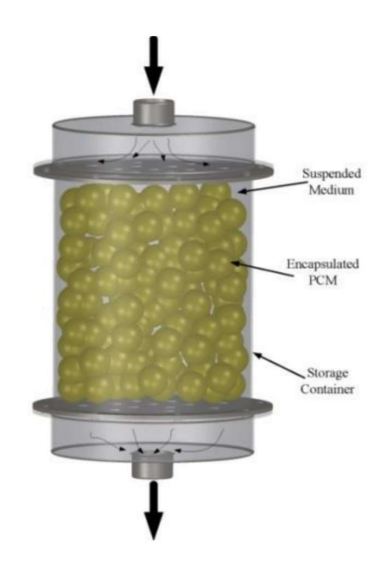


Figure 6 - Macro-encapsulated PCM TES system [6]

Nithyanandam et al. [22] studied the performance and cost of encapsulated PCM TES (EPCM-TES) and PCM TES with embedded heat pipes (HP-TES). PCM is encapsulated by tubes in EPCM-TES, while in HP-TES, heat pipes are inserted into a bath of PCM. The study showed that the system cost is dominated by containment cost and material cost. It identified design parametric space for GWh-scaled systems in both configurations with a cost of 13-17 \$/kWh.

Although, latent heat storage provides impressive energy density, heat transfer enhancement mechanisms are often required to keep the charge/discharge rate in an acceptable range. During discharging, a solid layer forms on the outer surface of PCM near the containment wall and propagates concentrically toward the center. Similar to solid-based sensible storage material, conduction within solid region hampers the heat

transfer. Commonly employed methods in heat transfer enhancement are by using a large quantity of small capsules to increase the heat transfer area, or by applying stationary inserts, such as multiple passages for HTF, or metal fins with higher conductivity to increase the overall conductivity [23,24]. Unavoidably, additional expenditure is required to implement those structures, and PCMs are generally expensive (\$0.24-0.88/kg [22]), so that the system cost becomes an issue.

Thermochemical energy storage (TCES)

Thermochemical energy storage uses a reversible endothermic/exothermic reaction of thermo-chemical materials to store and release energy. Energy storage by thermal decomposition of metal oxides has been extensively investigated [26,27]. Ammonia dissociation reaction serves as an example, where thermal energy is absorbed to facilitate the reaction of $2NH_3 \rightarrow N_2 + 3H_2$ and released during the reverse reaction of $N_2 + 3H_2 \rightarrow 2NH_3$, at around $400\text{-}500\,^{\circ}\text{C}$ with an energy density of 3.9 MJ/kg. Chen et al. [29] designed and fabricated an ammonia-based TCES that can be implemented to the CSP applications with supercritical Rankine stream cycle at 650 °C, as shown in Figure 7. Liquid ammonia and gaseous products are stored in a salt caverns or underground storage tank and separated by chilled separator. During charging, liquid ammonia is transported to the receiver where endothermic dissociation is triggered. The gaseous products return to the

storage tank and supplied to ammonia synthesizer where heat is released to generate steam for the power block. Heat exchangers are added to utilize the waste heat from both reactions. This ammonia-based system has no side reaction, uses inexpensive reactants, and can easily separate the reactants and products. In addition, the exothermic reactor can be directly used as a steam generator, which decreases the total cost of the CSP plant to be around \$13-\$18/kWh [28]. Other reactions such as decompositions of potassium oxide at 300-800 °C and lead oxide at 300-350 °C also yield promising energy density, 2.1 MJ/kg and 0.26 MJ/kg respectively [26]. In general, the main challenge that all TCES systems face is the parasitic production of high-temperature and high-pressure gas. It imposes great burden on containment materials that could potentially elevates the system cost with high risk in operation safety.

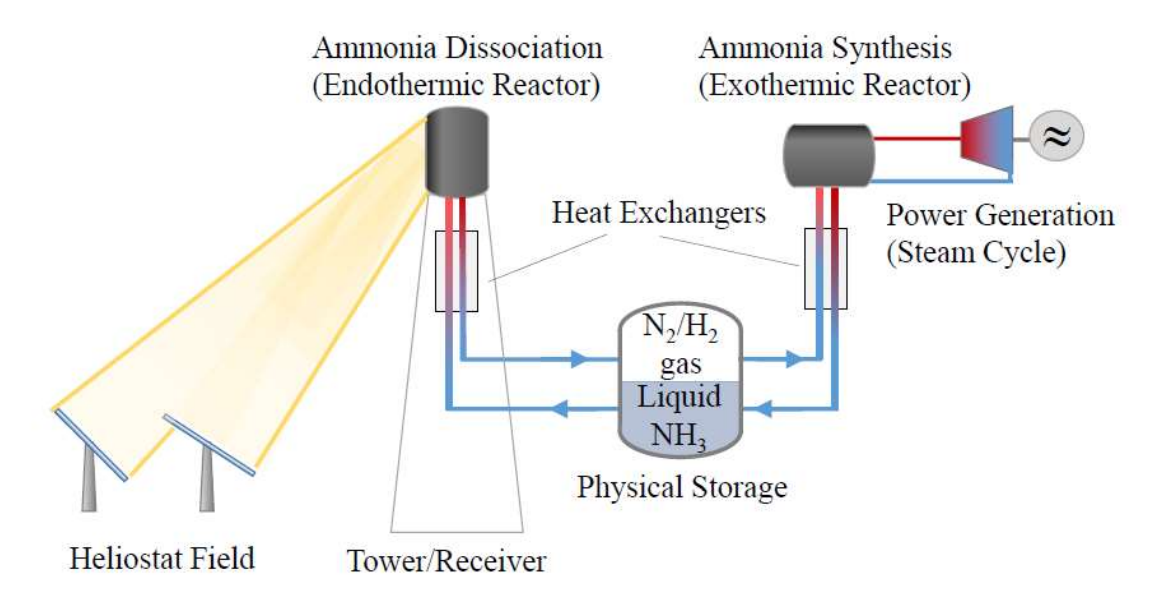


Figure 7 - Ammonia-based TCES system [28]

Cost comparison of current TES technologies

A preliminary cost comparison between different TES technologies is conducted based on available data from literature [5,6,12,13,22,25,28]. System cost shown in Figure 8 considers cost only for storage medium, containment and necessary heat transfer enhancement structures for PCM TES and reaction related components for TCES. Additional costs of insulation, foundation, valving and piping are not included.

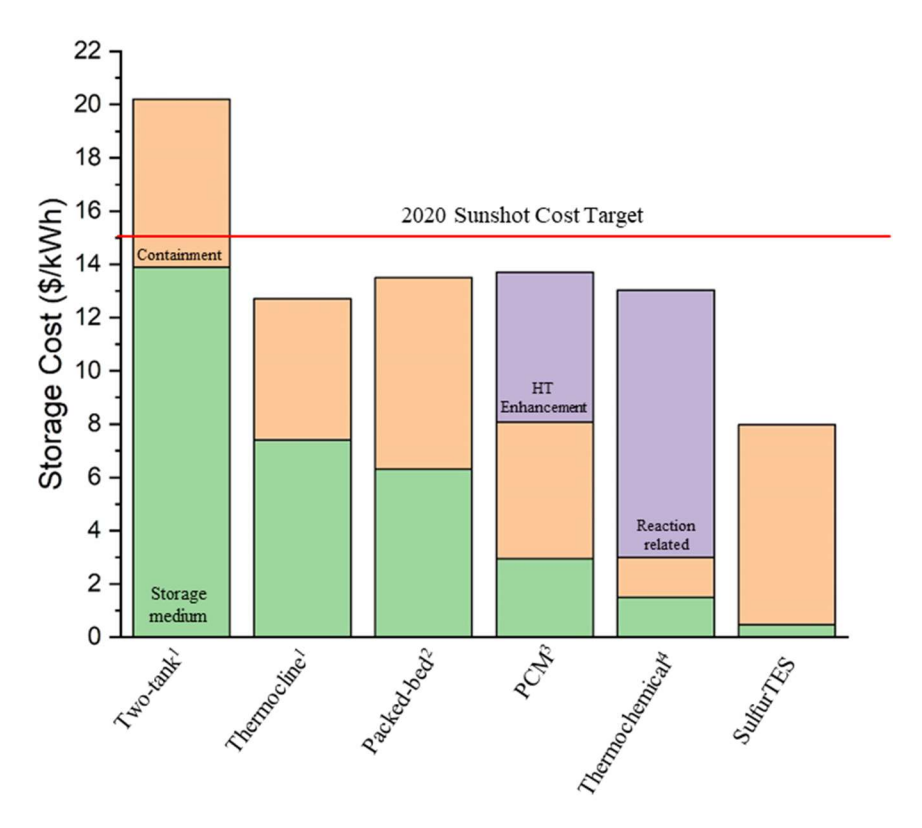


Figure 8 - Preliminary cost comparison between different types of TES systems

As seen from Figure 8, the cost of two-tank molten salt TES is around \$20/kWh with salt (\$10-13/kWh [5]) and containment (~\$6.5/kWh [6]). The cost of rock-based packed bed TES is not available in the literature. The author estimated the cost based on material list presented in ref. [12,13], with a 1250% over design in storage capacity and components' current market prices from ref. [14]. The estimated cost is around \$13.5/kWh, spending about half of the cost on storage medium. PCM TES cost is obtained from ref. [22,25]. The cost distribution is about \$3/kWh for storage medium, around \$5/kWh for container and around \$6/kWh for HTF passage tubes. Based on ref. [28], the storage medium cost of

TCES is around \$1.5/kWh with \$1.5/kWh containment cost. \$14.5/kWh is spent on reaction related components. However, since steam generator is automatically included in TCES, a \$4.4/kWh is deducted from the reactor cost, leaving a final cost of \$10.1/kWh for reactors.

Clearly, all TES systems under development show potential of achieving the Sunshot cost target of \$15/kWh. Especially in SulfurTES system, the cost of sulfur is almost unnoticeable, reducing the system cost to a great extent that provides the largest margin in achieving the target. An in-depth cost analysis of SulfurTES system is available in chapter 5.

2.2. The SulfurTES Concept

Comparing advantages and challenges of existing TES technologies, UCLA researchers proposed and evaluated the use of elemental sulfur as storage medium in high-temperature applications with potentially significant reduction in system cost. As an elemental material, sulfur is chemically stable up to 1000 °C [3], providing large operating temperature range for medium to high temperature sensible heat applications. This section discusses variation of physical and chemical properties of sulfur with varying temperature.

Chemical characteristics of sulfur

Sulfur is supplied from two main sources: natural mineral deposition and petroleum refinery industry, where sulfur is produced from crude oil desulfurization. Thanks to the abundant reserve in nature and continuous production, the price is kept extremely low, ranging from \$0.04 to \$0.1/kg [4].

Sulfur exists in solid phase below 113 °C and boils at around 444 °C. Solid Sulfur has two main forms: rhombic sulfur (S_{α}) and monoclinic sulfur (S_{β}) . S_{α} melts at 113 °C, and at temperature above 96 °C, S_{β} generation starts, pushing the melting temperature closer to 119 °C. Both types of sulfur crystalline are composed of one sulfur allotrope, S_{λ} , which is the only stable allotrope of sulfur at solid state. In liquid state, the majority of S_{λ} transforms into S_{μ} with a small amount of S_{π} (~7%) whose melting point is lower. Therefore, liquid sulfur solidifies at around 115 °C. S_{λ} exists as a puckered S_{α} ring, while S_{μ} s are long chains with uncertain number of sulfur atoms (S_{n}) .

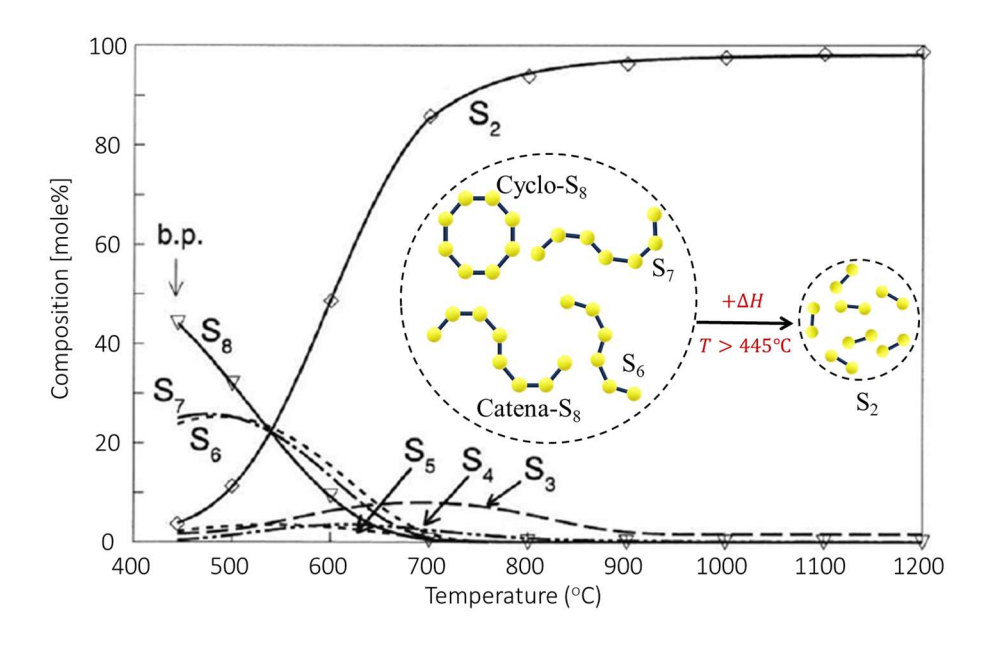


Figure 9 - Species concentration variation with temperature [3]

The species transformation commences at temperature around 160 °C, where S_8 rings break into long S_n chains, leading to a significant increase in viscosity. For pure sulfur, its viscosity peaks at around 188 °C, as further increase in temperature breaks those long chains into shorter chains (S_6 to S_2). At temperature above 1000 °C, all sulfur exists as S_2 .

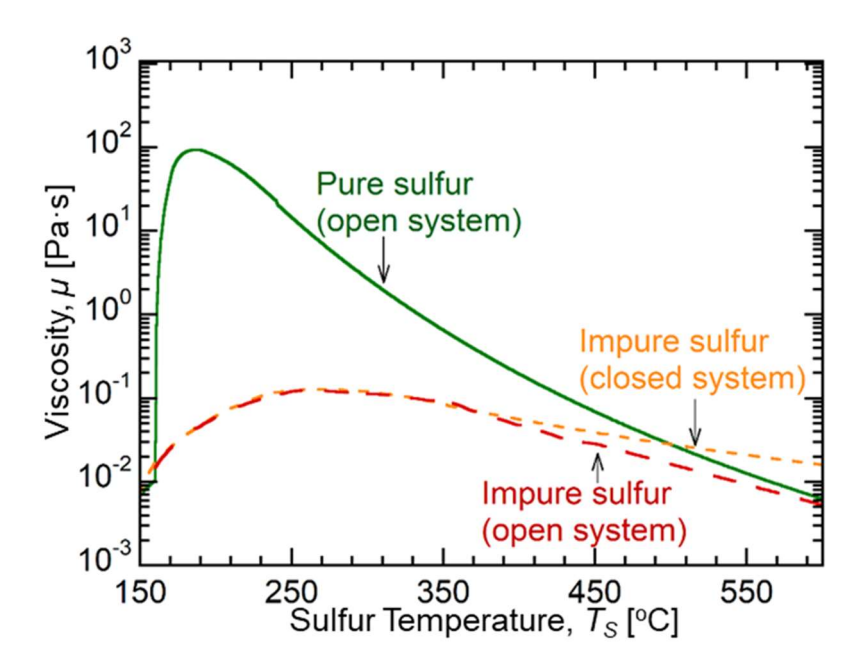


Figure 10 - Sulfur viscosity variation with temperature [31]

One way of preventing the huge viscosity dome is to add impurities, such as hydrogen sulfide and halogens. These impurities can replace some of the sulfur atoms to break the long chain or stay between long chains to lubricate the movement.

Isochoric containment of sulfur

As the first generation of SulfurTES that operates in laboratory environment, safety issues are considered extensively, such as possible leaking of toxic sulfur oxide gas, sulfur self-ignition beyond 200 °C, etc. To avoid these safety issues, the team decided to contain sulfur isochorically in a bundle of sealed tubes. Analogous to shell-and-tube heat exchanger, the tube bundle is enclosed by a shell with HTF flowing across it for heat

exchange. Therefore, it is imperative to understand the variation of sulfur property within the interested temperature range in isochoric tubes. Figure 11 shows thermophysical properties of sulfur under isochoric condition from 120 to around 650 °C.

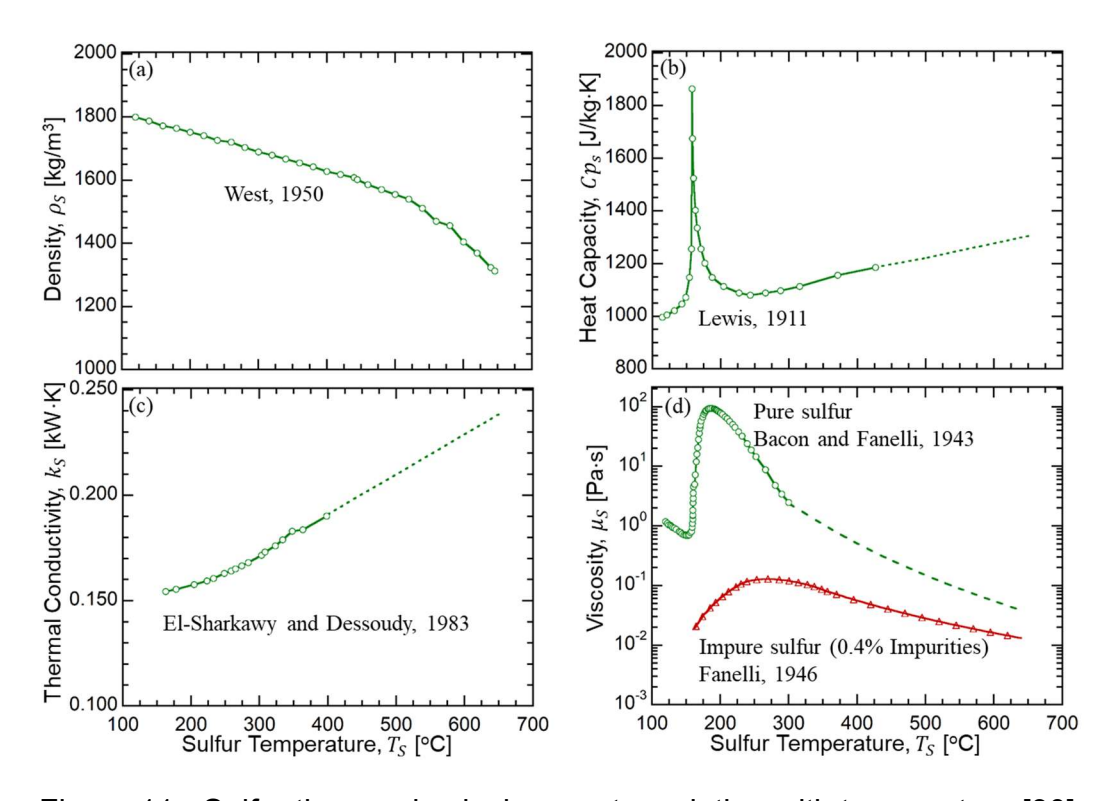


Figure 11 - Sulfur thermophysical property variation with temperature [30]

According to Figure 11 (a) (c), sulfur density and thermal conductivity changes linearly with temperature. A noticeable jump in sulfur heat capacity is observed between 160 to 250 °C, Figure 11 (b), which is caused by reaction among S_{λ} , S_{μ} , and S_{π} . The large viscosity issue with pure sulfur is solved by having impurities such as 0.4% concentration of H₂S, where impure sulfur has viscosity 2 orders of magnitude smaller than that of pure sulfur. Since most of the commercially available sulfur has purity around 99%, it is reasonable

to believe that the sulfur viscosity used for all later studies follow the trend shown by the red line in Figure 11 (d).

The research team also identified key engineering challenges associated with isochoric containment of sulfur. As noted from previous section, for each type of TES system, the containment cost composes a large portion of total system cost. We conducted a study to identify the compatibility between sulfur and a low-cost containment material that can withstand high temperature and corrosion issues associated with it [32]. To resist sulfidation, materials with high chromium content are ideal candidates, where chromium sulfide film is formed to protect the material. Stainless steel 316 (SS316), stainless steel 304 (SS304), and Inconel 625 are three types of material tested. SS 304 was chosen as a baseline case because it is known to be corrosive by sulfur. Inconel 625 and SS316 are resistant to sulfur corrosion, but SS316 is more promising due to its lower cost. The test was conducted by thermal cycling sealed tubes, filled with sulfur, of three materials mentioned above up to 500 °C for a total of 100 hours, 600 hours, 900 hours, and up to 600 °C for a total of 100 hours. The thickness of each tube was measured after the test.

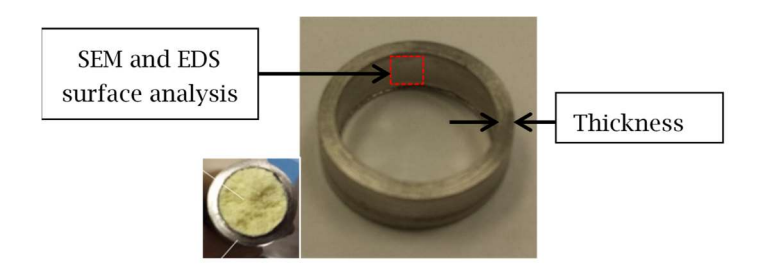


Figure 12 - Apparatus of sulfur compatibility test [32]

SS304 tubes showed significant corrosion as its thickness reduced from 1235 μm to 937 μm after 600 hours. On the other hand, SS316 and Inconel 625 tubes showed an increase in tube wall thickness of around 40 μm , due to the formation of protective sulfide film. The lower-cost SS 316 was finally selected as the containment material of SulfurTES system.

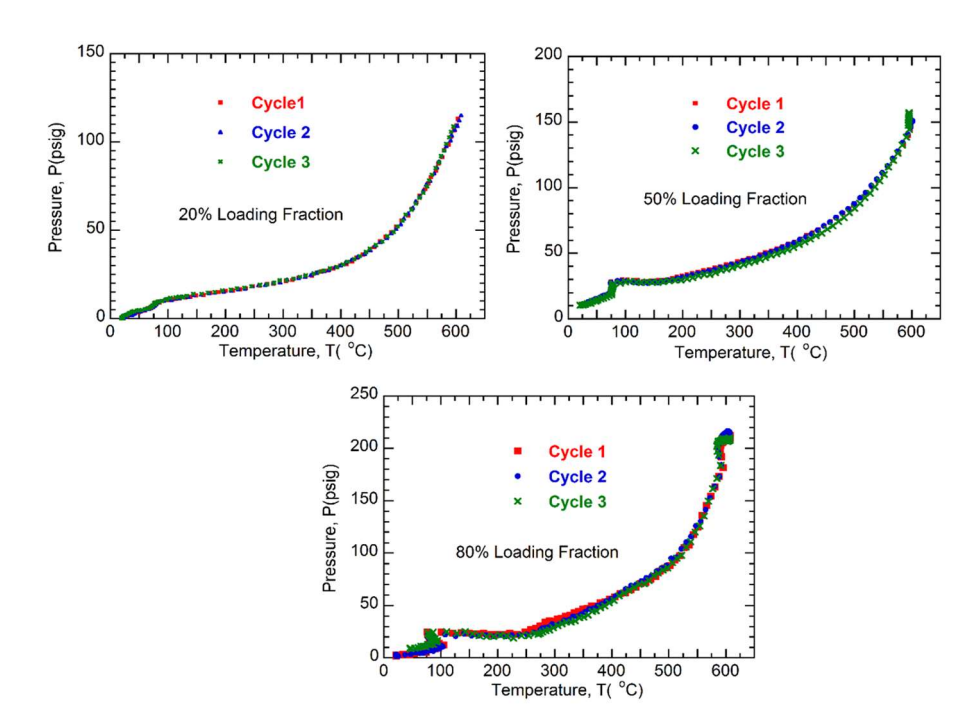


Figure 13 - Sulfur pressure-temperature relationship in isochoric containment [32]

Another major investigation focused on thermodynamic characteristics of sulfur in the temperature range of 25-600 °C [32]. The main objective of this study was to understand the pressure-temperature characteristics of sulfur and to quantify thermochemical benefits. Test were conducted by thermal cycling sulfur filled tubes, with various loading fraction, between room temperature to 600 °C. The sulfur load fraction denotes to the ratio between volume of filled sulfur and volume of the tube. Figure 13 shows the pressure-temperature relationship with 20%,50% and 80% loading fraction. It is observed that the vapor pressure at 600 °C with 80% loading fraction is around 200 psig, small enough to be safely contained by a SS316 pipe with Sch. 10 thickness.

The thermochemical transformation of sulfur due to temperature change was also analyzed to quantify the thermochemical benefit in energy storage capacity [33]. Allotropic transformation in solid sulfur (S_{α} to S_{β}) occurs at 95 °C with an enthalpy of transformation of 12.5 kJ/kg. As temperature increases, solid-liquid phase change takes place at around 119 °C (melting point of S_{β}), producing S_{λ} . At 159 °C, S_{π} starts to appear but with very low concentration ($<\sim7\%$). Transformation from S_{λ} to S_{μ} starts at 170 °C, with an enthalpy of transformation of 587 kJ/kg. By further increasing the temperature, S_{n} long chains break into shorter chains, leading to sulfur species transformation with increasing temperature. Considering all enthalpy of transformation, it is observed that

the total thermochemical energy is around 7% of total sensible energy with temperature range of 25-600 °C, similar to the latent heat of solid-liquid phase change.

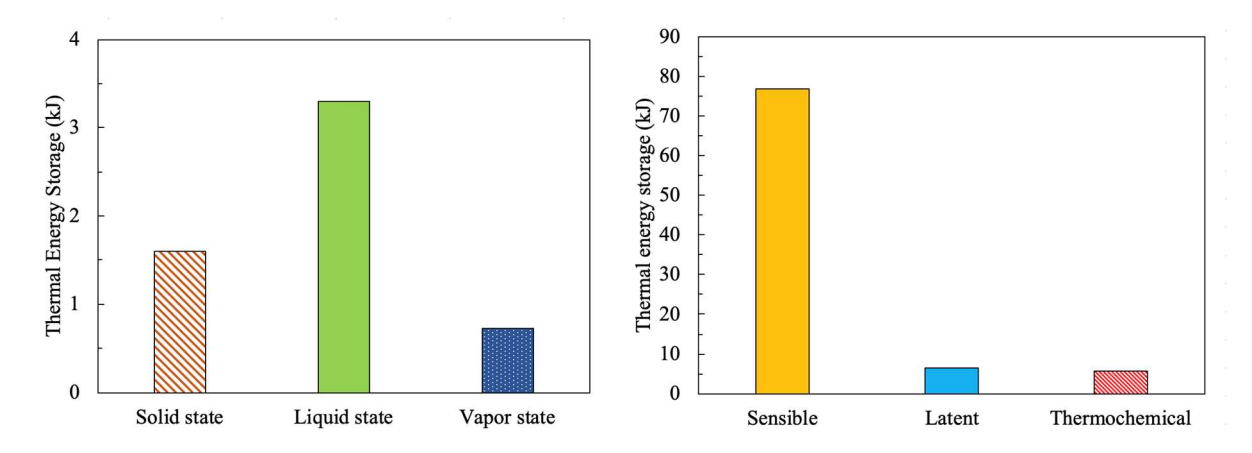


Figure 14 - Energy storage capacity distribution for sulfur [33]

Sulfur heat transfer performance

After understanding the chemical and thermodynamic characteristics of sulfur, the research team proceed to the investigation of sulfur heat transfer behavior in isochoric tube [34]. The goal of this study was to develop an experimentally validated computational model for predicting the heat transfer effectiveness at component level. The computational domain was established by sulfur and enclosing tube with fixed tube temperature as boundary condition.

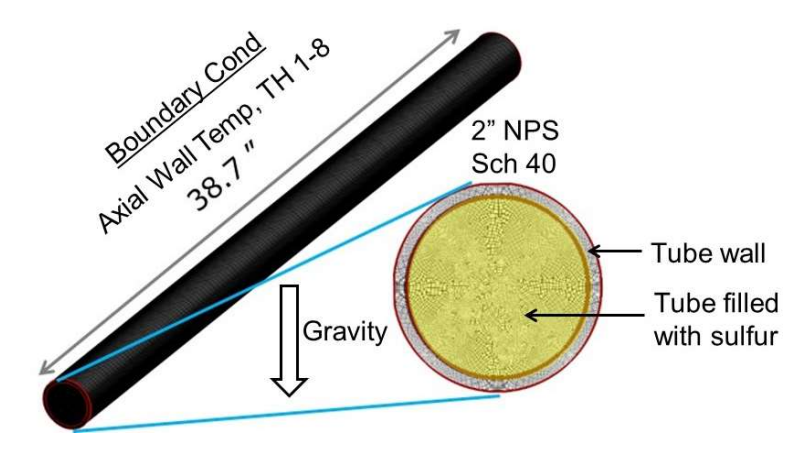


Figure 15 – Computational domain of isochoric sulfur containment [34]

Coupled momentum and energy equations were solved in ANSYS Fluent for tubes with different diameters. The results provided transient temperature and velocity profile where Nusselt number as a function of Rayleigh number was obtained to characterize the natural convective behavior of sulfur.

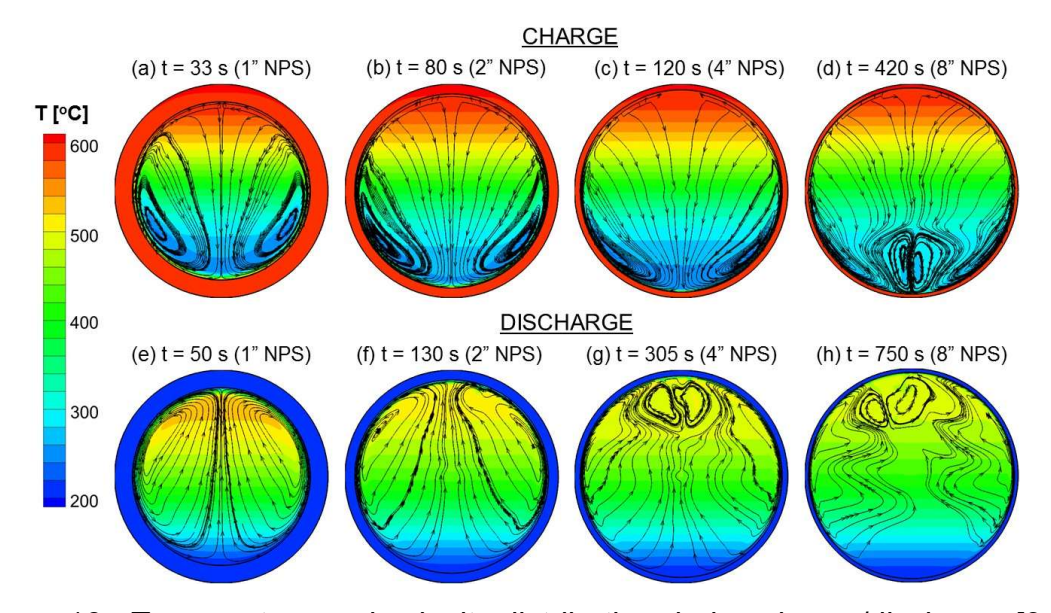


Figure 16 - Temperature and velocity distribution during charge/discharge [34]

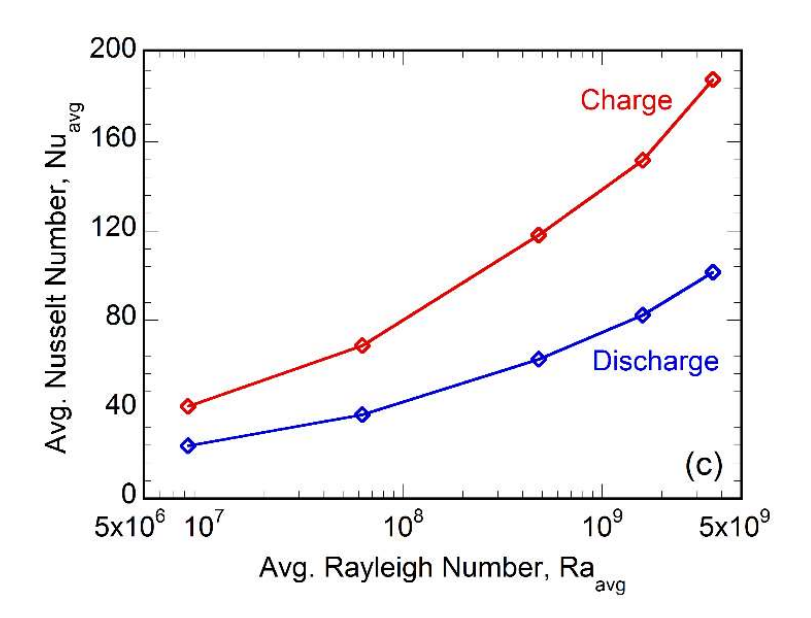


Figure 17 - Average Nusselt number with corresponding Rayleigh number [34]

It was observed that the Nusselt number is about 3 to 14 times larger than that of PCM based technologies ($Nu\# \sim 8$), confirming the superior heat transfer performance of sulfur that ensures high thermal responsiveness.

SulfurTES demonstration

With profound understanding in component level sulfur behavior, the team designed and fabricated a lab-scale, 10-kWh SulfurTES system to demonstrate the concept in system level [35]. Thermal cycles were safely performed, achieving both target operating temperature and amount of energy stored. Following the successful lab demonstration, A pilot-scale, 30-kWh SulfurTES system was built and integrated with real CSP-dish collector for an on-sun demonstration [33]. The system was charged by real solar energy

for around 6 hours, successfully storing more than 30-kWh of energy. More details are available in appendix C and D.

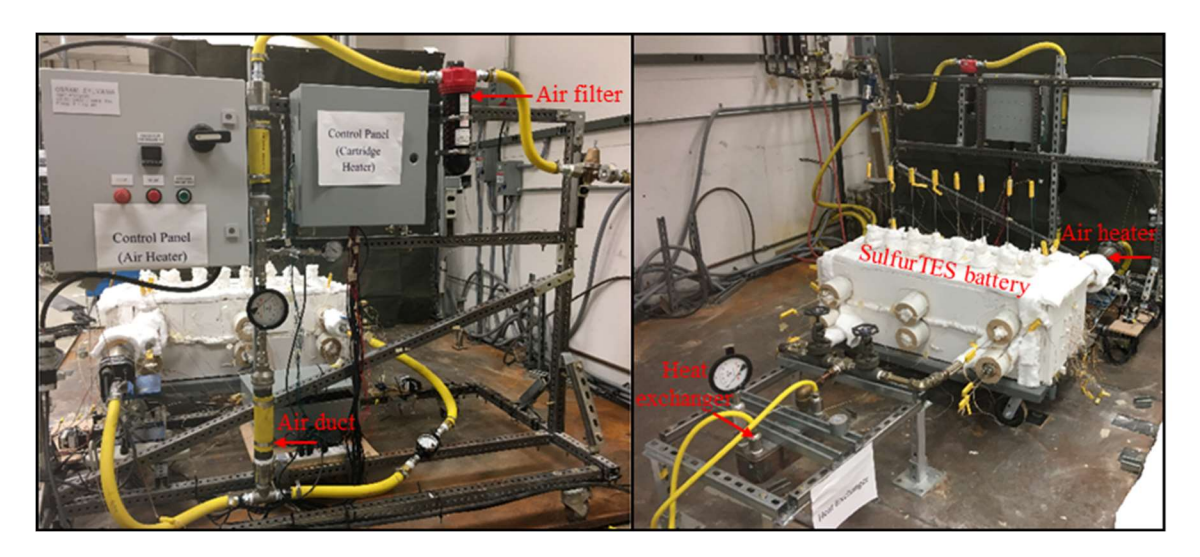


Figure 18 - Lab-scale SulfurTES demonstration system [35]



Figure 19 - Pilot scale SulfurTES demonstration system with CSP-dish collector [33]

Summary of SulfurTES technology and the need for system performance analyses

The research team has proposed the concept of sulfur-based TES system with great potential of reducing the total system cost. We investigated critical characteristics of sulfur as a thermal storage material, including corrosion compatibility with low-cost containment materials, pressure-temperature characteristics, thermochemical reactions with temperature variation, and heat transfer behavior in isochoric tubes. Component level investigations confirmed that sulfur is a promising storage medium thanks to its fast thermal responsiveness and non-corrosive to low-cost SS316 container with small thickness. Lab-scale and pilot-scale systems successfully demonstrated their capability in promptly storing energy near nominal storage capacity, and the possible integration with industrial facility, powered by renewable energy. Despite all successful previous efforts in component level and demonstrative scale, performance and cost of SulfurTES systems in commercial and utility scales are still unknown. To provide a comprehensive investigation on industrial-scaled SulfurTES systems, a system model is developed, enabling a parametric study where variation of system level performance is observed with varying system geometry and operating condition. The following section presents a literature review on system modeling and performance studies of other TES systems.

2.3. System performance and cost analyses of sulfur-based thermal energy storage

Many researchers have developed analytical/numerical models to characterize the thermal performance of TES systems. Mathematical models for TES systems are based on energy interactions between key system components, including the storage medium, HTF, storage container, and insulation. Schumann [36] analytically modeled the packedbed sensible TES using infinite series and Bessel functions. The model assumes storage rocks and HTF are lumped systems with uniform radial temperature profile. The model consists of coupled energy equations for HTF and solid storage medium considering turbulent motion of HTF. The solution to the energy equations provides transient axial temperature distribution in both components. Lacroix [37] developed a model for PCM TES in a shell-and-tube configuration where PCM is isochorically contained in the tube while HTF flows along the tube. The model was based on enthalpy method where transient temperature and liquid fraction of PCM are both included. The liquid fraction was iteratively determined at each time step, providing accurate temperature prediction as well. The enthalpy equation of HTF is similar to energy equation due to the absence of phase-change. Modi et al. [38] modeled molten-salt thermocline TES system with filler bed using a one-dimensional numerical model. The effect of having filler bed was represented by porosity, where a continuity equation was coupled to establish relationship between porosity and HTF velocity. Additionally, heat loss was considered as a heat sink term in the energy equation for HTF with a heat transfer coefficient obtained by empirical correlation. Xu et al. [39] presented the development of a two-dimensional model for a packed-bed molten-salt thermocline TES system. The momentum equation of HTF (molten-salt) is included to provide thermofluidic interaction between HTF and filler material. The energy equation for insulation is also coupled into the model to account for the heat loss.

With high-fidelity computational models, further investigations on system level performance and cost analyses were conducted in many previous efforts. G. Angelini et al. [40] predicted and compared the performance of molten-salt TES in single-tank thermocline and two-tank configurations based on energy generation by continuously operating for a week. It was observed that, in single-tank configuration, due to destruction of thermocline, only 64% of energy can be utilized, compared with 100% energy efficiency in two-tank configuration, requiring overdesign in the storage capacity. Additionally, optimum geometry of storage tank was found to be 14 m in height and 21.2-23.7 m in diameter for a 6-7h storage capacity. The higher storage tank brought better thermal stratification, but heat loss becomes prominent for tanks higher than 30 m. Tehrani et al. [41] compared the annual performance of molten-salt TES systems in

different configurations, including two-tank, single tank and dual-medium thermocline for CSP application. They acknowledged the superior energy efficiency of two-tank configuration and believed that TES systems in single-tank and dual-medium configurations should be discharged as much as possible, in spite of power block part load operating, to achieve techno-economic target. Despite drawbacks of single-tank system in energy utilization, the system cost can still be reduced as less components are required. Strasser et al. [42] compared performance and cost of single-tank thermocline TES systems with packed-bed (PBTC) and structured-concrete (SCTC) filler beds. Two types of concrete structures were of interest: axisymmetrically placed concrete tubes and parallelly placed concrete plates. They discovered that the PBTC system provides better thermal stratification that leads to a higher discharge utilization of around 8% compared to SCTC at cutoff temperature of 500 °C. A cost analysis for a 2-GWh system was conducted including all parasitic components, such as insulation, foundation, pipes, pumps, electrical controlling devises etc. The result showed that the cost of PBTC is \$30/kWh while that of SCTC is \$34/kWh. The difference in cost is caused by difference in discharge utilization, where more storage and containment materials are required to provide same amount of energy with lower discharge utilization. Nithyanandam et al. [22] evaluated the system level performance of latent heat TES systems with encapsulation tubes and PCM bath with heat pipes. The performance is evaluated based

on exergetic efficiency, amount of electricity generation, and levelized cost of energy. Based on a systematic parametric study on tank height, tank radius, channel width, tube radius, feasible system design space and operating conditions were identified to meet SunShot 2020 LCOE target of ¢6/kWh.

Besides performance and cost analyses for utility-scaled TES systems, researches on commercial-scaled TES systems were conducted. Commercial-scaled TES systems are often applied for building heating/cooling. In building heating applications, operating temperature range is relatively small, 25-100 °C, where PCM TES are commonly used. Mahfuz et al. [43] investigated the cost and performance of PCM TES for building solar heating. The storage medium was paraffin wax, operating between 25-80 °C with phase-change temperature of 56 °C. Discharge utilization and exergetic efficiency were obtained with various HTF flow rate. It was concluded that the discharge utilization increases while flow rate increases, but opposite was true for exergetic efficiency. Due to small operating temperature range, the highest exergetic efficiency was around 14%, resulting in an around \$56 of lost exergy in 20-year lifetime where the total life-time cost was around \$600.

Chapter 3 System model for SulfurTES performance

The objective of this study is to investigate the performance of SulfurTES battery with an experimentally validated model and provide a design guideline for the development of industrial scale SulfurTES systems. Initially, we developed a 2D, transient state numerical model to predict the temperature distribution within SulfurTES battery during thermal charge/discharge cycle. This model was validated using the experimental results of the thermal cycling of laboratory-scale SulfurTES battery. The high-fidelity numerical model was then used for the parametric analysis of the 1 MWh SulfurTES system to investigate the effect of geometric parameters and HTF flow conditions on the system thermal performance. This analysis revealed the relationship between design and performance parameters, which was further used to formulate the design strategy to develop SulfurTES system that will meet the specified performance targets. This study has established a framework to develop the SulfurTES systems that will provide a superior thermal performance for medium to high temperature applications.

3.1. System description and model assumption

Figure 20 shows a schematic of the SulfurTES system and its cross-sectional view. Based on the concept of a shell-and-tube heat exchanger, system in thermal battery configuration has a bundle of sulfur-filled steel tubes that are enclosed by a circular shell

with heat transfer fluid (HTF) inlet/outlet placed on either end. The system geometry is specified by an inner shell diameter, $D_{sh,i}$, a shell length L and a tube bundle arrangement. The tube bundle is supported by baffles separated by a baffle spacing, $Bs = 0.2 D_{sh,i}$. The tubes are arranged in a 30° triangular layout, with tube pitch ratio, $P_r = \frac{P_t}{d_o}$ and percent baffle cut, Bc, determined based on TEMA standard [44] and recommendations by heat exchanger design handbook [45]. The system is covered with vertically installed high-temperature insulation on both ends, and horizontal insulation throughout the shell body to minimize the heat loss.

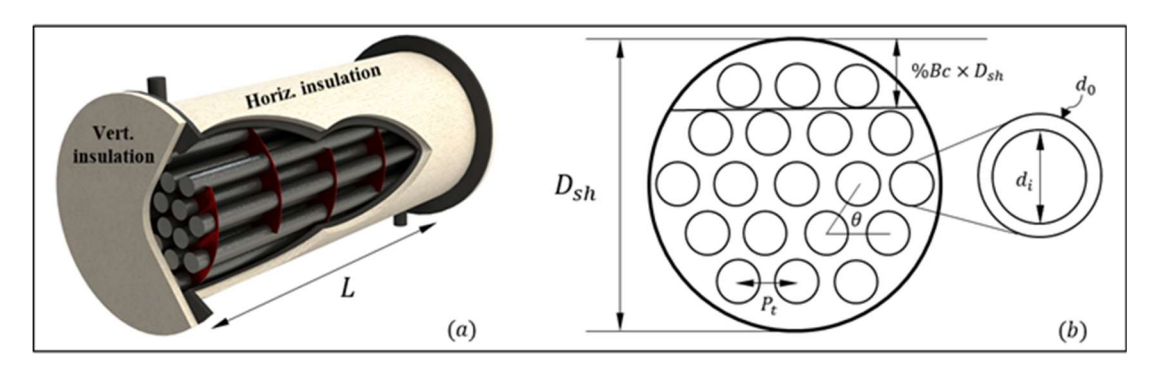


Figure 20 - (a) SulfurTES system (b) configuration cross-sectional view

During thermal charging, the hot HTF enters the system at one end, flows axially along a tortuous path while supplying the heat to the system and leaves the system at the other end. A schematic of flow path of charging is shown in Figure 21. The flow path is reversed during thermal discharging.

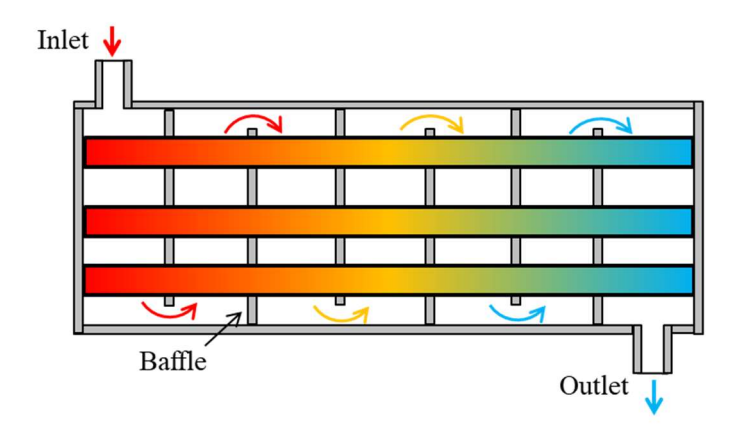


Figure 21 - HTF flow path (e.g., during charging)

In the current model, the HTF temperature is assumed to vary solely along the flow direction (axial direction). Temperatures of shell and tube walls are assumed to be radially invariant at any time instance while varying only in the axial direction. This assumption is valid due to its relatively low conductive resistance [46]. Although temperature variation in sulfur is radially dependent, the ongoing analysis considers volume-averaged sulfur temperature only. Due to the assumption of radial uniformity in HTF temperature, the vertical insulation that is in contact with HTF will only have axial temperature gradient across its thickness. However, for horizontal insulation, both axial and radial temperature gradients coexist, due to the axial temperature variation in HTF and the large temperature difference between the system and ambient environment across its thickness, respectively. The axial conduction within horizontal insulation is

negligibly small compared to radial conduction, due to much larger radial temperature gradient than that in axial direction, and thus, ignored here.

3.2. Governing equations

The thermal behavior of the system is modeled based on the energy transfer between each component, including sulfur, steel tube, heat transfer fluid (HTF), shell, and insulation. The energy conservation principle is applied to each component to predict its transient temperature field during thermal cycling. Eqs. (1)-(6) denote to corresponding energy equations,

Sulfur:
$$\rho_s C_{p,s} \left(\frac{\partial T_s}{\partial t} \right) = \frac{h_s p_i (T_s - T_t)}{A_{cr.s}} + k_s \frac{\partial^2 T_s}{\partial z^2}$$
 (1)

Tube:
$$\rho_t C_{p,t} \left(\frac{\partial T_t}{\partial t} \right) = \frac{h_f p_o(T_t - T_f)}{A_{cr,t}} + \frac{h_s p_i(T_t - T_s)}{A_{cr,t}} + k_t \frac{\partial^2 T_t}{\partial z^2}$$
 (2)

HTF:
$$\rho_f C_{p,f} \left(\frac{\partial T_f}{\partial t} + v \frac{\partial T_f}{\partial z} \right) = \frac{h_f p_o(T_f - T_t)}{A_{cr,f}} + \frac{h_f p_{sh}(T_f - T_{sh})}{A_{cr,f}} + k_f \frac{\partial^2 T_f}{\partial z^2}$$
(3)

Shell:
$$\rho_{sh}C_{p,sh}\left(\frac{\partial T_{sh}}{\partial t}\right) = \frac{h_f p_{sh}(T_{sh} - T_f)}{A_{crsh}} + k_{sh}\frac{\partial^2 T_{sh}}{\partial z^2}$$
 (4)

Vertical insulation:
$$\rho_{ins}C_{p,ins,V}\left(\frac{\partial T_{ins,V}}{\partial t}\right) = k_{ins}\frac{\partial^2 T_{ins,V}}{\partial r^2}$$
 (5)

Horizontal insulation:
$$\rho_{ins}C_{p,ins,H}\left(\frac{\partial T_{ins,H}}{\partial t}\right) = k_{ins}\frac{\partial^2 T_{ins,H}}{\partial r^2}$$
 (6)

where, ρ , C_p , k, T refer to density, constant pressure specific heat, thermal conductivity and temperature of each component. p and A_{cr} denote to axial perimeter and cross section. The subscripts 'f, t, s, sh' denote to HTF, tube, sulfur, and shell, and subscripts

"ins,V" and "ins,H" refer to vertically and horizontally installed insulation respectively. The subscript 'o' and 'i' refer to outer and inner tube diameter. The above coupled governing equations are solved using a finite volume approach. The advection term of HTF in Eq. (3) is solved using a hybrid scheme, and conductive term in all other components are solved via first order central difference scheme, assuming a piece-wise linear profile. First order fully implicit scheme is applied to transient term to ensure the stability of the numerical scheme [47]. The discretized energy equations of Eq. 1-6 are expressed as:

Sulfur:
$$\rho_s C_{p,s} \left(\frac{T_{s,j}^i - T_{s,j}^{i-1}}{\Delta t} \right) = \frac{h_s p_i \left(T_{s,j}^i - T_{t,j}^i \right)}{A_{cr,s}} + k_s \frac{\left(T_{s,j-1}^i - 2T_{s,j}^i + T_{s,j+1}^i \right)}{\Delta z^2}$$
 (7)

Tube:
$$\rho_t C_{p,t} \left(\frac{T_{t,j}^i - T_{t,j}^{i-1}}{\Delta t} \right) = \frac{h_f p_o}{A_{cr,t}} \left(T_{t,j}^i - T_{f,j}^i \right) + \frac{h_s p_i}{A_{cr,t}} \left(T_{t,j}^i - T_{s,j}^i \right) + k_t \frac{(T_{t,j-1}^i - 2T_{t,j}^i + T_{t,j+1}^i)}{\Delta z^2}$$
 (8)

$$\text{HTF:} \quad \rho_f C_{p,f} \frac{(T_{f,j}^i - T_{f,j}^{i-1})}{\Delta t} + max \left[\left(\frac{k_f}{\Delta z^2} + \frac{\rho_f C_{p,f}}{2\Delta t} \right), \frac{\rho_f C_{p,f}}{\Delta t}, 0 \right] \left(T_{f,j}^i - T_{f,j-1}^i \right) + max \left[\left(\frac{k_f}{\Delta z^2} - \frac{\rho_f C_{p,f}}{2\Delta t} \right), \frac{\rho_f C_{p,f}}{\Delta t}, 0 \right] \left(T_{f,j}^i - T_{f,j-1}^i \right) + max \left[\left(\frac{k_f}{\Delta z^2} - \frac{\rho_f C_{p,f}}{2\Delta t} \right), \frac{\rho_f C_{p,f}}{\Delta t}, 0 \right] \left(T_{f,j}^i - T_{f,j-1}^i \right) + max \left[\left(\frac{k_f}{\Delta z^2} - \frac{\rho_f C_{p,f}}{2\Delta t} \right), \frac{\rho_f C_{p,f}}{\Delta t}, 0 \right] \left(T_{f,j}^i - T_{f,j-1}^i \right) + max \left[\left(\frac{k_f}{\Delta z^2} - \frac{\rho_f C_{p,f}}{2\Delta t} \right), \frac{\rho_f C_{p,f}}{\Delta t}, 0 \right] \left(T_{f,j}^i - T_{f,j-1}^i \right) + max \left[\left(\frac{k_f}{\Delta z^2} - \frac{\rho_f C_{p,f}}{2\Delta t} \right), \frac{\rho_f C_{p,f}}{\Delta t}, 0 \right] \left(T_{f,j}^i - T_{f,j-1}^i \right) + max \left[\left(\frac{k_f}{\Delta z^2} - \frac{\rho_f C_{p,f}}{2\Delta t} \right), \frac{\rho_f C_{p,f}}{\Delta t}, 0 \right] \left(T_{f,j}^i - T_{f,j-1}^i \right) + max \left[\left(\frac{k_f}{\Delta z^2} - \frac{\rho_f C_{p,f}}{2\Delta t} \right), \frac{\rho_f C_{p,f}}{\Delta t}, 0 \right] \left(T_{f,j}^i - T_{f,j-1}^i \right) + max \left[\left(\frac{k_f}{\Delta z^2} - \frac{\rho_f C_{p,f}}{2\Delta t} \right), \frac{\rho_f C_{p,f}}{\Delta t}, 0 \right] \left(T_{f,j}^i - T_{f,j-1}^i \right) + max \left[\left(\frac{k_f}{\Delta z^2} - \frac{\rho_f C_{p,f}}{2\Delta t} \right), \frac{\rho_f C_{p,f}}{\Delta t}, 0 \right] \left(T_{f,j}^i - T_{f,j-1}^i \right) + max \left[\left(\frac{k_f}{\Delta z^2} - \frac{\rho_f C_{p,f}}{2\Delta t} \right), \frac{\rho_f C_{p,f}}{\Delta t}, 0 \right] \left(T_{f,j}^i - T_{f,j-1}^i \right) + max \left[\left(\frac{k_f}{\Delta z^2} - \frac{\rho_f C_{p,f}}{2\Delta t} \right), \frac{\rho_f C_{p,f}}{\Delta t}, 0 \right] \left(T_{f,j}^i - T_{f,j-1}^i \right) + max \left[\left(\frac{k_f}{\Delta z^2} - \frac{\rho_f C_{p,f}}{2\Delta t} \right), \frac{\rho_f C_{p,f}}{\Delta t}, 0 \right] \left(T_{f,j}^i - T_{f,j-1}^i \right) + max \left[\left(\frac{k_f}{\Delta z^2} - \frac{\rho_f C_{p,f}}{2\Delta t} \right), \frac{\rho_f C_{p,f}}{\Delta t}, 0 \right] \left(T_{f,j}^i - T_{f,j-1}^i - \frac{\rho_f C_{p,f}}{\Delta t} \right) \right] \left(T_{f,j}^i - T_{f,j-1}^i - \frac{\rho_f C_{p,f}}{\Delta t} \right) \left(T_{f,j}^i - T_{f,j-1}^i - \frac{\rho_f C_{p,f}}{\Delta t} \right) \left(T_{f,j}^i - T_{f,j-1}^i - \frac{\rho_f C_{p,f}}{\Delta t} \right) \right) \left(T_{f,j}^i - T_{f,j-1}^i - \frac{\rho_f C_{p,f}}{\Delta t} \right) \left(T_{f,j}^i - T_{f,j-1}^i - \frac{\rho_f C_{p,f}}{\Delta t} \right) \left(T_{f,j}^i - T_{f,j-1}^i - \frac{\rho_f C_{p,f}}{\Delta t} \right) \left(T_{f,j}^i - T_{f,j-1}^i - \frac{\rho_f C_{p,f}}{\Delta t} \right) \right) \left(T_{f,j}^i - T_{f,j-1}^i - \frac{\rho_f C_{p,f}}{\Delta t} \right) \left(T_{f,j}^i$$

$$\frac{\rho_{f}c_{p,f}}{2\Delta t}, -\frac{\rho_{f}c_{p,f}}{\Delta t}, 0\right] \left(T_{f,j}^{i} - T_{f,j-1}^{i}\right) = \frac{h_{f}p_{o}}{A_{cr,f}} \left(T_{f,j}^{i} - T_{t,j}^{i}\right) + \frac{h_{f}p_{i}}{A_{cr,f}} \left(T_{f,j}^{i} - T_{sh,j}^{i}\right)$$
(9)

Shell:
$$\rho_{sh}C_{p,sh}\left(\frac{(T_{sh,j}^{i}-T_{sh,j}^{i-1})}{\Delta t}\right) = \frac{h_{f}p_{sh}}{A_{cr,sh}}\left(T_{sh,j}^{i}-T_{f,j}^{i}\right) + k_{t}\frac{(T_{sh,j-1}^{i}-2T_{sh,j}^{i}+T_{sh,j+1}^{i})}{\Delta z^{2}}$$
 (10)

Vertical insulation:
$$\rho_{ins}C_{p,ins,V}\left(\frac{(T_{ins,V,j}^{i}-T_{ins,V,j}^{i-1})}{\Delta t}\right) = k_{ins}\frac{(T_{ins,V,j-1}^{i}-2T_{ins,V,j}^{i}+T_{ins,V,j+1}^{i})}{\Delta r^{2}}$$
(11)

Horiz. insulation:
$$\rho_{ins}C_{p,ins,H}\left(\frac{(T_{ins,H,j}^{i}-T_{ins,H,j}^{i-1})}{\Delta t}\right) = k_{ins}\frac{(T_{ins,H,j-n}^{i}-2T_{ins,H,j}^{i}+T_{ins,H,j+n}^{i})}{\Delta r^{2}}$$
 (12)

3.3. Heat transfer Coefficients (HTC)

The interstitial heat transfer coefficients are obtained empirically to avoid complexity of solving moment interaction between each component, providing an acceptable run time that enables a performance study on a large parametric space of geometric parameters and operating conditions. Discussions on empirical correlations for HTF side and sulfur side heat transfer coefficients are presented in the following sections.

Shell side HTC and pressure drop

The design of the system is based on shell-and-tube heat exchanger, which allows the shell side heat transfer coefficient, h_J , be obtained based on Bell-Delaware method [48]. In the current study, the Bell-Delaware method is utilized because it considers the effect of numerous geometric terms affecting the pressure drop and heat transfer performance, which are accounted for via the coefficients R and J respectively. Coefficients R and J are products of multiple correction factors accounting for effects such as baffle leakage, bundle bypass flow etc. Details on determination of each correction factor is presented in [48]. The corrected heat transfer coefficient is expressed as:

$$h_o = h_i J = J \phi c_{p,f} j \frac{\dot{m}_f}{S_m} P r_f^{-2/3} \propto N u^{a_2} P r_f^{1/3} k_f / D$$
 (13)

where h_i is the heat transfer coefficient for flow across the ideal tube bank. S_m is the crossflow area through the shell centerline and is represented by $S_m = b_s \left[\frac{(D_{sh} - d_o)}{P_t/d_o}(P_t/d_o)\right]$, b_s is the spacing between baffles, Pr_f is the Prandtl number for the shell-side fluid, ϕ is the wall viscosity compensation term ($\phi = \left(\frac{\mu(T=T_w)}{\mu(T=T_f)}\right)^{0.14}$), and j is the Colburn factor that are correlated by Taborek [48] where coefficients are dependent on the tube layout, tube pitch ratio ($P_r = P_t/d_o$), and Reynolds number, $j = a_1 \left(\frac{1.33}{P_r}\right)^a Re_D^{a_2}$.

The pressure drop within the system is calculated as the summation of pressure drop from crossflow region, baffle window region and entrance/exist section, expressed as: $\Delta P_S = \Delta P_c + \Delta P_w + \Delta P_e = R \left[(N_b - 1) + \left(1 + \frac{N_{tcw}}{N_{tc}} \right) \right] \left(\frac{2fN_c}{\rho} \left(\frac{m_f}{S_m} \right)^2 \right) + R \left(\frac{(2+0.6N_{cw})m_f^2}{2\rho S_m S_w} \right) \qquad (14)$ where N_{tc} , and N_{tcw} is the effective number of tube rows crossed between baffle tips and in the flow window, respectively, f is the friction factor, and S_w is the net crossflow area through one baffle window given by $S_w = \frac{\pi D_{sh}^2}{4} - \frac{N_t \pi d_0^2}{4} b_c$. Calculations by Bell et al. [49] determine N_c and N_{cw} as $N_{tc} = D_{sh}(1-2b_c)/P_t$ and $N_{tcw} = 0.8b_c D_{sh}/P_t$. The friction factor is correlated with Reynolds number in the form of: $f = b_1 \left(\frac{1.33}{P_r} \right)^b Re_D^{b_2}$. Coefficients in expressions of Colburn factor f and friction factor f are tabulated based on empirical results from testing with shell and tube heat exchangers.

Sulfur side HTC

For the temperature range of 50-600 °C, sulfur exists in different physical states: solid, solid-liquid, and liquid, depending upon the temperature. Therefore, the sulfur heat transfer mechanisms vary significantly with temperature, and their effect is accommodated using appropriate sulfur side heat transfer coefficients for each sulfur phase.

Solid phase

The sulfur exists in solid state at temperatures < 115 °C, and thus, an effective heat transfer coefficient $h_{cond}\left(\frac{w}{m^2K}\right)$ is used to characterize the conduction within sulfur. Initially, a transient temperature distribution within sulfur was obtained by solving a 1D, transient state energy conservation as shown in Eq.(15). Then effective convection coefficient, h_{cond} and effective Nusselt number is computed as shown in Eqs. (16)- (17).

$$\frac{1}{r}\frac{\partial}{\partial r}\left(r\frac{\partial T(r,t)}{\partial r}\right) = \frac{1}{\alpha}\frac{\partial T(r,t)}{\partial t} \tag{15}$$

$$h_{cond}(t) = -k \frac{\left(\frac{\partial T(r,t)}{\partial r}\right)_{r=R}}{T_t - T_s(t)}$$
(16)

$$Nu(t) = \frac{h_{cond}(t)d_i}{k} \tag{17}$$

where, T_s is the cross-sectional area-averaged sulfur temperature at each time instance, α is the thermal diffusivity of sulfur, and R is the inner radius of tube. Solving Eq. (15) with

constant tube wall temperature boundary condition provides sulfur temperature variation with time, $T_s(t)$. However, during thermal charging, tube temperature is a dependent variable that varies with time as well, $T_t(t)$. Thus, to close the problem, a non-dimensional sulfur temperature, $T^*(t)$ is defined to correlate instantaneous $h_{cond}(t)$ with instantaneous sulfur and tube temperature combined:

$$T^*(t) = \frac{T_s(t) - T_{s,i}}{T_t(t) - T_{s,i}} \tag{18}$$

where, $T_{s,i}$ is the initial sulfur temperature, $T_{s,i} = T_D$. In each time step, T^* can be calculated based on T_s and T_t from previous time step, and the corresponding Nusselt number can be obtained based on following correlation.

$$Nu = 3637.596T^{*6} - 12804.29T^{*5} + 18022.76T^{*4} - 12925.86T^{*3} + 4980.08T^{*2} - 992.17T^{*} + 90.54$$
(19)

Details of this analysis are presented in appendix A.

Solid-liquid phase change

During thermal charging, as the steel tube is heated to > 115 °C, sulfur at the tube wall melts. As thermal charging progresses, the sulfur liquid fraction increases, and natural convection becomes a dominant sulfur heat transfer mechanism. Nithyanandam et al. [50] studied sulfur heat transfer performance during thermal cycling in low temperature range of 50-200 °C, to characterize the sulfur heat transfer with phase-change. They

presented the Nusselt number and corresponding solid-liquid Rayleigh number against Fourier number. The Nusselt number correlations in terms of solid-liquid Rayleigh number are obtained by curve-fitting, and their expressions are::

charge:
$$Nu = 2.230Ra_{s-l}^{0.1702} - 0.746$$
 (20)

discharge:
$$Nu = 9.711 \times 10^{-6} Ra_{s-l}^{1.018} + 6.955$$
 (21)

where solid-liquid Rayleigh number is defined as $Ra_{s-l} = \frac{\rho^2 c_p g \beta (T_s - T_t) [d_l (1 - \sqrt{1 - \gamma})^3]}{\mu k}$, d_l is the inner diameter of tube and γ is the liquid fraction that determines the characteristic length during phase-change process. The liquid fraction with corresponding T_s is also provided by Nithyanandam et al. [50], (Figure 22), and their correlation can be obtained by curve fitting, as shown in Eq.22.

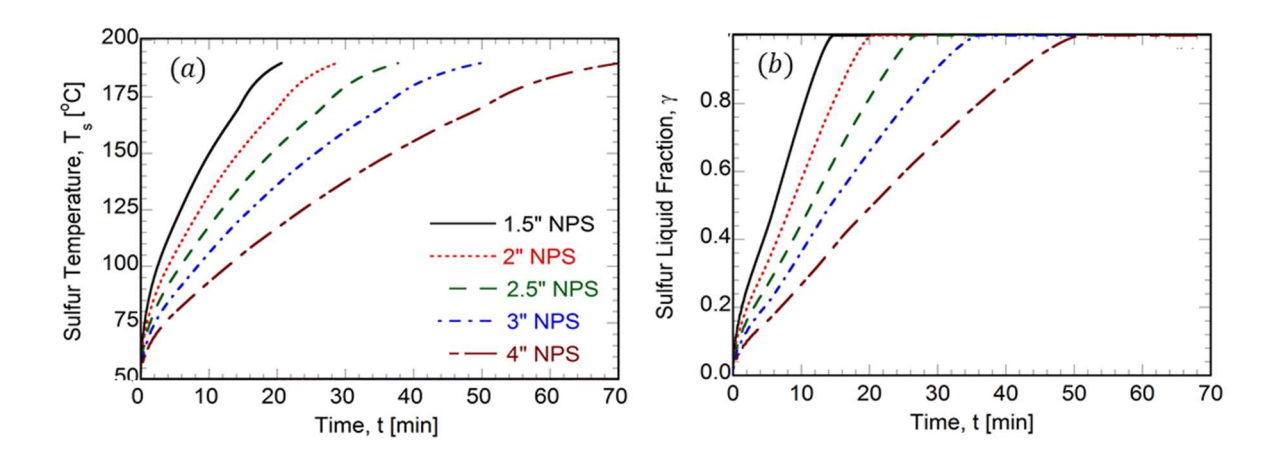


Figure 22- (a) Area-averaged sulfur temperature, (b) corresponding liquid fraction [50]

$$\gamma = -1.44 \times 10^{-8} T_s^4 + 6.73 \times 10^{-6} T_s^3 - 1.12 \times 10^{-3} T_s^2 + 0.087 T_s - 2.5$$
 (22)

Liquid phase

At high temperatures, sulfur exists in a purely liquid phase, wherein heat transfer within sulfur occurs via natural convection. Nithyanandam et al. [34] proposed the Nusselt number correlations for sulfur charge/discharge in high temperature range of 200-600 °C and are presented as:

charge:
$$Nu = 0.909Ra^{0.242} - 1.612$$
 (23)

discharge:
$$Nu = 0.545Ra^{0.238} - 0.79$$
 (24)

where,
$$Ra = \frac{g\beta d_i^3 (T_S - T_t)\rho^2 C_p}{\mu k}$$
.

Integrated correlation for sulfur heat transfer

The Nusselt number correlations developed by Nithyanandam et al.[34,50] for 50-200 °C and 200-600 °C have an artificial temperature break at 200 °C. Therefore, both correlations were integrated to formulate a continuous correlation to characterize the sulfur heat transfer over 50-600 °C. The continuous correlations for sulfur charge/discharge are expressed as:

charge:
$$Nu = 0.6228Ra^{0.2611} - 1.376$$
 (25)

discharge:
$$Nu = 0.4995Ra^{0.2409} + 0.4571$$
 (26)

Figure 23 shows the comparison of continuous Nusselt number correlations with independent Nusselt number correlations developed for low (50-200 °C) and high temperatures (200-600 °C). The continuous correlations are in agreement with the original

correlations with average errors of 5.02% and 6.31% for low-temperature charge/discharge, while 0.58% and 1.42% for high-temperature charge/discharge, respectively.

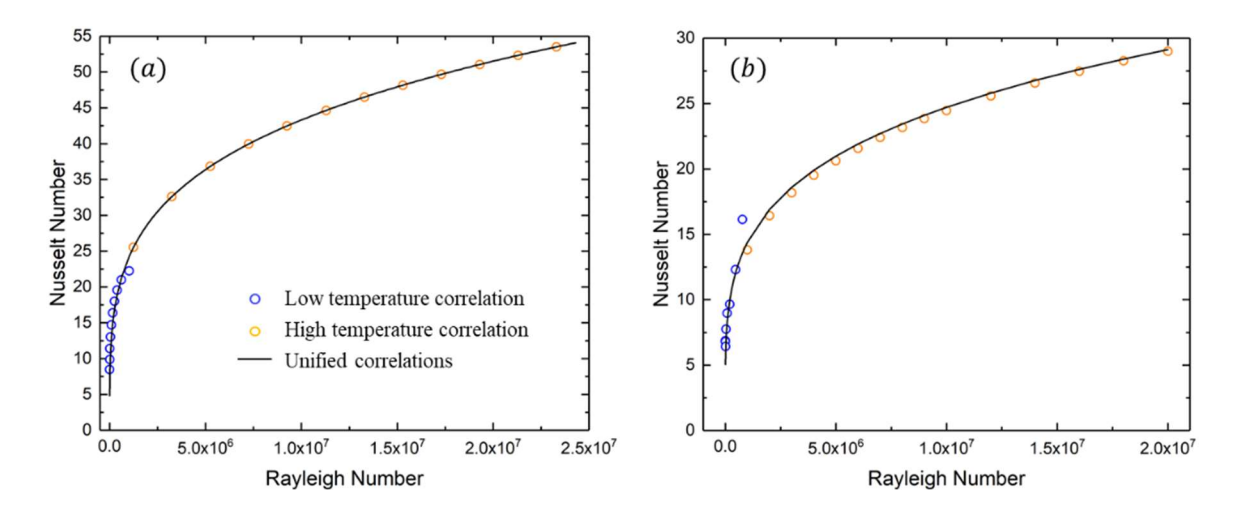


Figure 23 - The comparison of integrated correlations with original correlations for (a) charge (b) discharge operation

However, when sulfur is in solid state or at the beginning of phase-change, conduction is still dominant, where convection effect within molten sulfur is negligible. The liquid fraction and corresponding Ra_{s-l} are close to zero, leading to an unrealistically small heat transfer coefficient using continuous correlation. To avoid this, the effective heat transfer coefficient for conduction will also be evaluated simultaneously and compared to the convective heat transfer coefficient till the volume-averaged sulfur temperature is above sulfur melting temperature. The larger one will be adopted.

3.4. Thermal properties

The thermo-physical properties (C_p , ρ , k) of the HTF (air) are obtained from the NIST Chemistry WebBook Standard Reference Database [50], and those of sulfur are from Sulfur Data Book [31]. Temperature dependencies of air and sulfur properties are obtained by curve fitting and are presented in Table 1 and Table 2, respectively. For stainless steel, temperature averaged constant properties were used as follows: $\rho_t = 8000 \ kg/m^3$, $C_{p,t} = 550 \ J/kg \ K$ and $k_t = 19 \ W/mK$ [52].

Sulfur latent heat incorporation

One special treatment on sulfur specific heat is done to incorporate latent heat of solid-liquid phase change. During phase-change, the melt front starts from the peripheral and concentrically propagates toward the center of the tube. Accurately predicting volumetric-averaged sulfur temperature thus requires the incorporation of latent heat. We have formulated a correlation for effective specific heat capacity to account for the latent heat of sulfur via volumetric liquid fraction and is presented as:

$$C_{p,s,eff} = \frac{C_{p,s}(T_{pc,start} - T_D) + C_{p,s}(T_{pc,end} - T_{pc,start})Q^*(\gamma)}{(T_s - T_D)}$$
(27)

where, $T_{pc,start}$ and $T_{pc,end}$ are volumetric-average sulfur temperature at the beginning and end of solid-liquid phase change respectively. Q^* is a dimensionless energy content, defined as:

$$Q^*(\gamma) = \frac{m_s c_{p,s} (T_C - T_D) + \gamma sl}{m_s c_{p,s} (T_C - T_D)}$$
(28)

where, l is the latent heat of solid-liquid phase change. The correlation between Q^* and γ is obtained from the sulfur heat transfer analysis presented by Nithyanandam et al. [50].

$$Q^* = -0.23\gamma^2 + 1.28\gamma + 0.11 \tag{29}$$

where γ ranges from 0 to 1, and Q^* is observed to increase from 0 to around 1.3, shown in Figure 24.

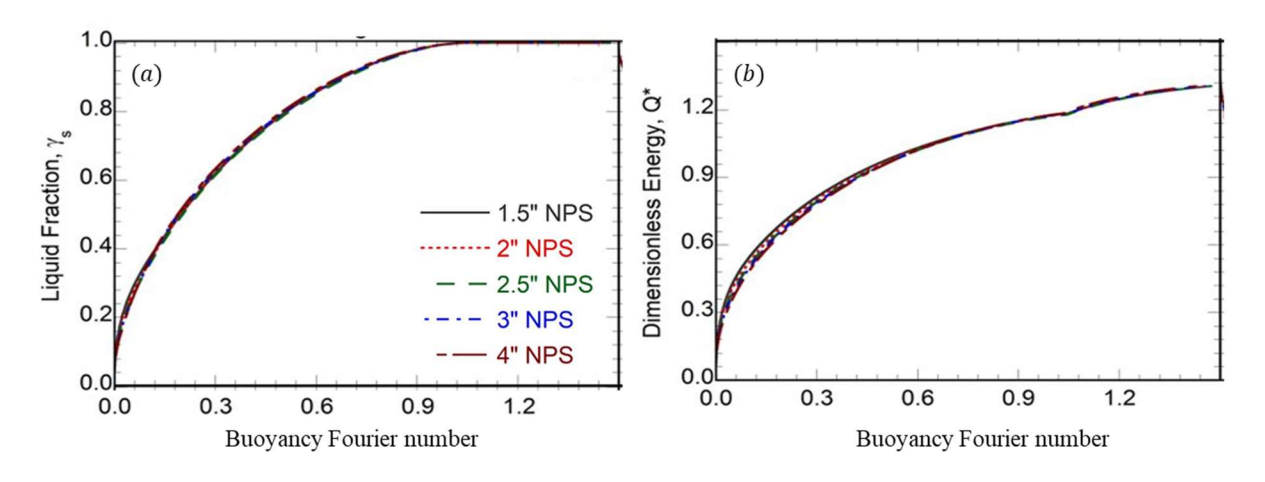


Figure 24 - (a) Liquid fraction and (b) corresponding dimensionless energy content [50]

The model uses sulfur temperature from previous time step to calculate liquid fraction according to Eq.16 and corresponding Q^* with Eq.29. Subsequently, $C_{p,s,eff}is$ acquired based on Eq.27.

Table 1: Thermal properties of HTF (air)

Properties	Air (unit of T: °C)		
Density, ρ [kg/m ³]	$1.52 \times 10^{-12}T^4 - 7.35 \times 10^{-9}T^3 + 1.29 \times 10^{-5}T^2 - 9.91T + 3.243$		
Specific heat, $C_p[J/kgK]$	$1.12 \times 10^{-13} T^4 - 5.35 \times 10^{-10} T^3 + 8.27 \times 10^{-7} T^2 - 2.59 \times 10^{-4} T + 1.032$		
Viscosity, μ [Pa s]	$-3.97 \times 10^{-13}T^4 + 2.15 \times 10^{-9}T^3 - 4.7 \times 10^{-6}T^2 + 6.99 \times 10^{-3}T + 0.109$		
Thermal Conductivity, k [W/mK]	$3.23 \times 10^{-13}T^4 + 1.96 \times 10^{-9}T^3 - 5.16 \times 10^{-6}T^2 + 1.03 \times 10^{-2}T + 0.064$		

Table 2: Thermal properties of Sulfur

Properties	Sulfur (unit of T: °C)		
Density, ρ [kg/m ³]	$-4.55 \times 10^{-6}T^3 + 3.94 \times 10^{-3}T^2 - 1.64T + 1952.43$		
Specific heat, $C_p[J/kgK]$	0.556T + 943		
Viscosity (T < 340 °C), μ [Pa s]	$4.38 \times 10^{-8}T^3 - 4.62 \times 10^{-5}T^2 + 0.015T - 1.53$		
Viscosity ($T > 340$ °C), μ [Pa s]	$e^{-8.74 + \frac{3914.07}{T + 273.15}}$		
Thermal Conductivity, k [W/mK]	$2.15 \times 10^{-4}T + 0.048$		

3.5. Initial and boundary conditions

Following are the boundary conditions used for the numerical analysis of SulfurTES charge/discharge cycle.

Charging:

$$T_f(z=0) = T_C - k_{ins} \frac{\partial T_{ins,V}}{\partial z} (z = L_1 + L_2) = (h_{NC} + h_{rad}) (T_{ins,V} - T_o)$$
 (30)

Discharging:

$$T_f(z = L_1) = T_D, k_{ins} \frac{\partial T_{ins,V}}{\partial z} (z = -L_2) = (h_{NC} + h_{rad}) (T_{ins,V} - T_o)$$
 (31)

where, L_1 is the length of system and L_2 is the thickness of insulation. The coordinate system can be found in section 3.6. h_{NC} and h_{rad} are heat transfer coefficients for natural convection over a horizontal cylinder and effective radiative heat transfer coefficient, respectively. These coefficients are calculated using empirical correlations available in the literature [46].

$$h_{rad} = \varepsilon \sigma (T_{ins}^2 + T_o^2)(T_{ins} + T_o)$$
(32)

$$h_{NC} = \frac{NuL}{k_{ins}} \tag{33}$$

$$Nu = \left\{ 0.6 + \frac{0.387Ra_D^{\frac{1}{6}}}{\left[1 + \left(\frac{0.559}{pr}\right)^{\frac{9}{16}}\right]^{\frac{8}{27}}} \right\}^2$$
 (34)

Initial conditions are expressed as:

Charging:

$$T_s = T_t = T_{sh} = T_{ins} = T_D \tag{35}$$

Discharging:

$$T = T(t = t_C) \tag{36}$$

where, at the beginning of charging, the system temperature is assumed to be uniformly distributed and equals to the discharge temperature, and the initial condition of discharge is set to be the temperature distribution at the end of charging.

3.6. Time step and grid size dependency study

Figure 25 shows a schematic of the discretized system. According to assumptions described in section 3.1, axial discretization (in z direction) is applied to sulfur, tube, HTF, shell and vertical insulation, as their temperature is assumed to be variant in axial direction only. To capture axial and radial temperature variation, discretization in both directions are applied to horizontal insulation. The mesh applied to sulfur, tube, HTF and shell discretizes each component with length L_1 , into n_1 grids, with a size of Δz . A finer mesh is applied to insulation due to large temperature gradient, where insulation with thickness L_2 is discretized across its thickness into n_2 grids with a grid size of Δr .

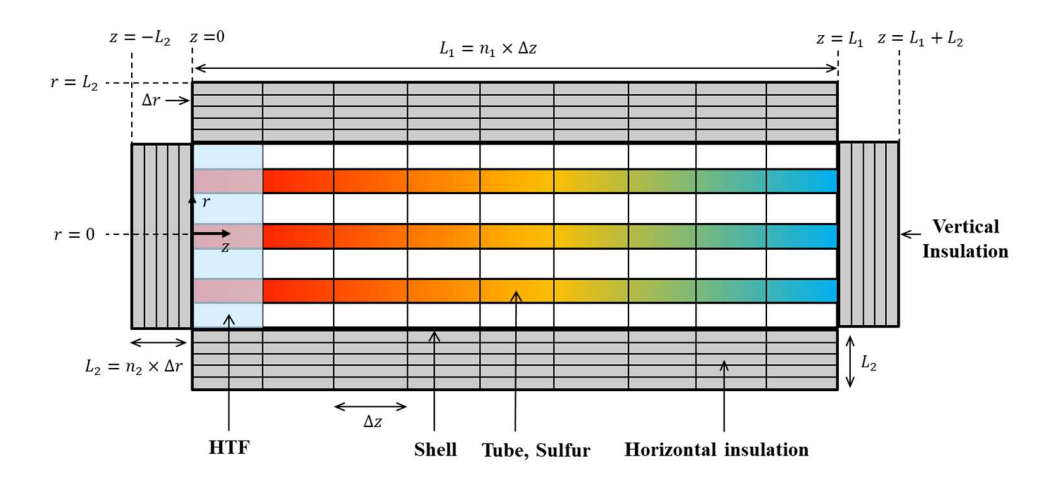


Figure 25 - System discretization with coordinate

We conducted a time step and grid size dependency study to ensure the numerical error is minimum. To accurately capture the axial temperature gradient by HTF flow and radial temperature gradient across the insulation, two grid sizes are of interest: axial grid size Δz and radial grid size Δr . The variation in HTF outlet temperature is used to analyze the effect of grid sizes.

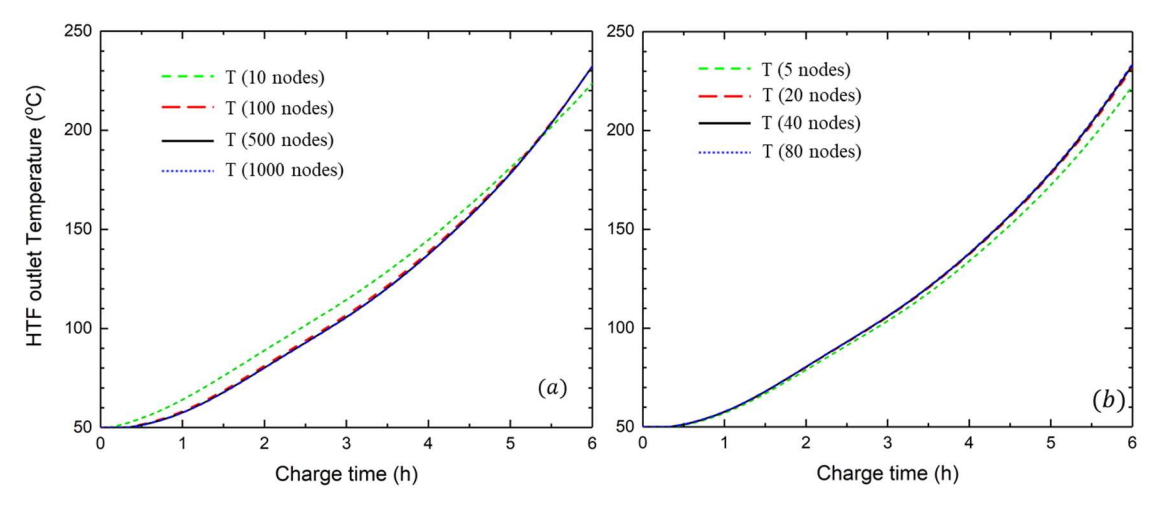


Figure 26 - HTF outlet temperature of the system with varying number of (a) axial nodes (b) radial discretized nodes

Figure 26 (a) and (b) show the results of the grid size study for a system with D_{sh} = 1.2 m, L_1 = 5 m, d_0 = 0.06 m, L_2 = 5.3 cm, and \dot{m}_f = 0.29 kg/s. The average relative error between HTF temperatures for axial nodes of 500 and 1000 is 0.097%, while the average relative error between HTF temperatures for radial nodes of 40 and 80 is 0.14%. Therefore, numbers of axial and radial grids are chosen as 500 nodes and 40 nodes, respectively. The corresponding axial and radial grid sizes are 1 cm and 1.3 mm, respectively.

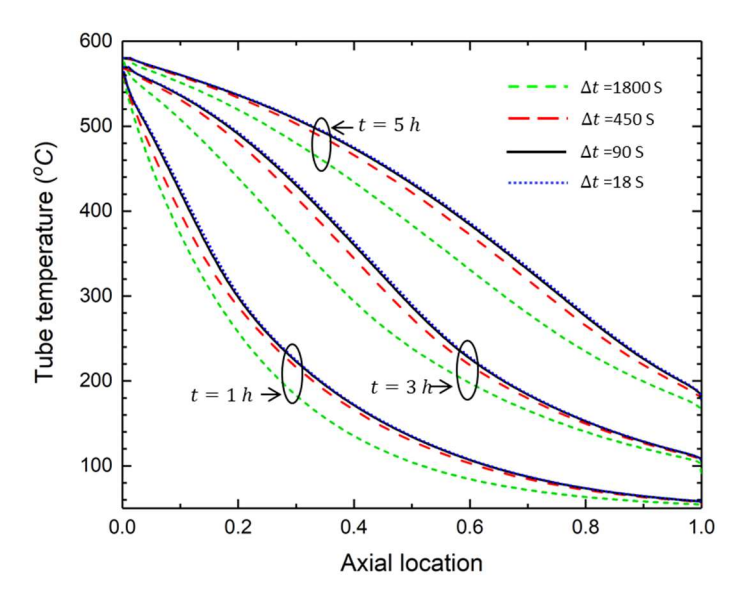


Figure 27 - Tube temperature distribution at three time instances with varying time step

The effect of time step is presented by tube temperature distribution at three time instances during charging, as shown in Figure 27. The result of time step study shows that the average relative error is 0.53% between time step of 90 seconds and 18 seconds. Therefore, 90 seconds was set as the size of each time step.

3.7. Model validation

Barde et al [35] developed the laboratory-scale SulfurTES battery to demonstrate the viability of SulfurTES technology for medium-high temperature applications. The numerical model is validated using experimental results from the thermal cycling of the laboratory-scale SulfurTES battery. Temperature measurements were taken at 6 axial positions, shown in Figure 28, each with 3-4 radial temperature measurements, to capture the axial temporal profile based on cross-sectional averaged temperatures. Position of T_1 is the charge inlet/discharge outlet of the 10-kWh lab demonstration system and position of T_2 corresponds to the charge outlet/discharge inlet. More details of the system and experimental procedure are presented in [35]. The numerical model was used to predict the temperature distribution within the SulfurTES battery for the identical initial and boundary conditions as observed during the experimental analysis.

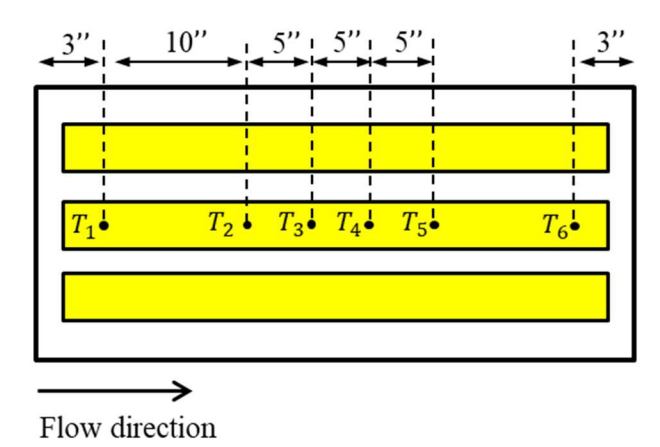


Figure 28 - Locations of tube temperature measurements along the axis

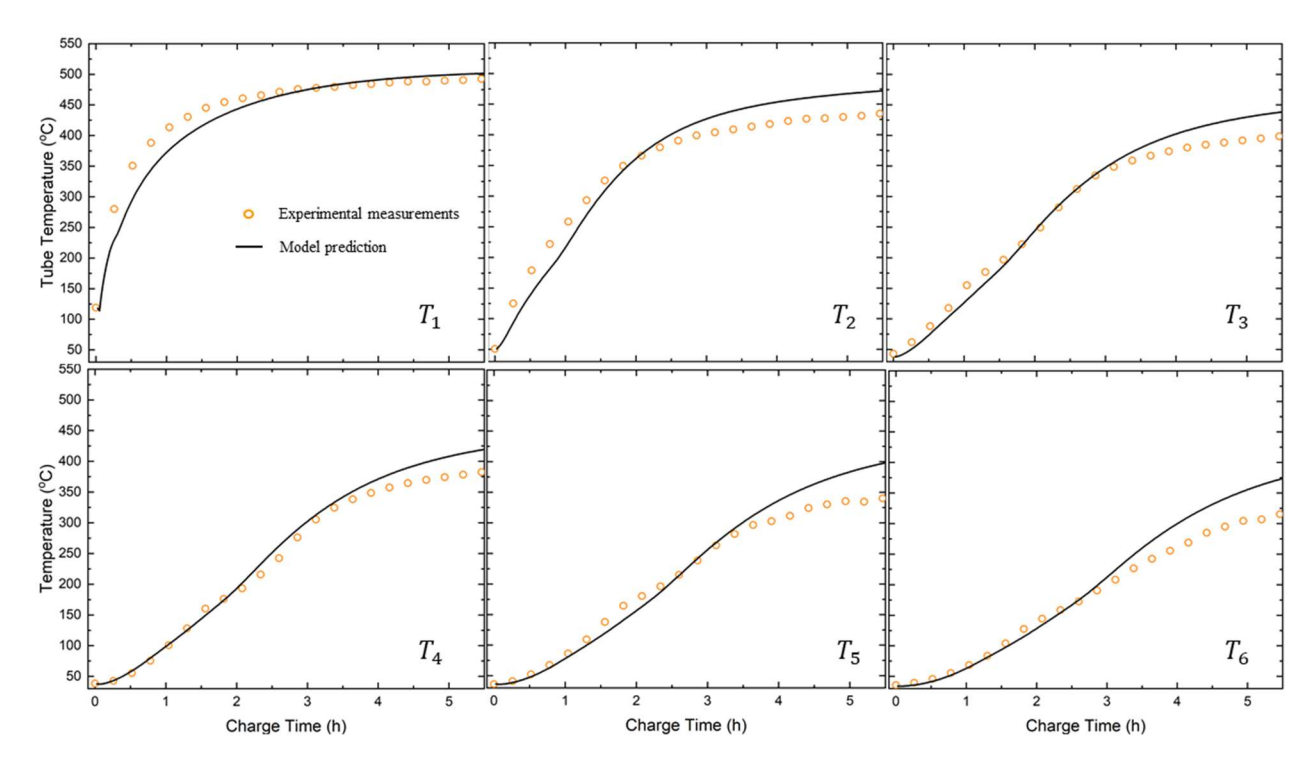


Figure 29 - Comparison between predicted and measured tube temperature

Figure 29 shows the comparison of measured and predicted tube temperature at locations shown in Figure 28 during thermal charging. The relative error for T_1 to T_6 are 2.9%, 4.5%, 4.1%, 3.2%, 6.9%, and 8.7% respectively. The predicted results compare well with experimental results in earlier stage of charging (before 3.5 hours), while the model overpredicts the tube temperatures later (> 3.5hrs.) into the charging process. The overprediction of tube temperatures could be the result of the additional heat loss during experiments, due to imperfect installation of insulation panels. These imperfections provide pathways with higher effective conductivity for heat to escape to the ambient, and such practical imperfections could not be accurately incorporated in the numerical

model. These effects become prominent at later stages during thermal charging due to higher system temperatures and accumulation of the total heat loss. Despite these practical limitations, ~5% average error shows that the model can well predict the temperature distribution within SulfurTES battery and can be used for the parametric study of the SulfurTES systems.

Chapter 4 Performance characterization and design strategy of SulfurTES system

The numerical model developed in the previous chapter was employed to perform a parametric study, establishing basis in advising design of industrial-scale TES systems with superior thermal performance. In the study, SulfurTES system was agnostic to heat source and heat load to enable a comprehensive observation of system level performance without limitations on geometric design and operating conditions. The parametric study assumed fixed storage capacity of 1-MWh, but with varying design parameters and operating under different mass flow rates. A system design strategy could thus be developed based on the outcomes of the parametric study.

The numerical model was validated using a 10-kWh system, while it was used to characterize the performance of the 1-MWh systems. Although, these systems significantly vary in size, their thermal and flow characteristics are comparable, and thus governing mechanisms are similar. These similarities allow use of the numerical model, validated using a laboratory-scale SulfurTES battery, to characterize the performance of a 1-MWh SulfurTES system. The comparison of important non-dimensional parameters for both systems is presented later (section 4.1) to demonstrate the similarity between them.

4.1. Parametric study of 1 MWh system

To avoid arbitrarily selecting design parameters and operating conditions, a systematic approach was adopted here, where design parameters varied with regularity and operating mass flow rate was chosen so that the amount of energy provided was in the vicinity of storage capacity.

The design parameters of SulfurTES battery are selected based on TEMA standards [44] and recommendations from heat exchanger design hand book [45] to match with standardized design convention. According to heat exchanger design handbook [45], shell inner diameter, $D_{sh,i}$, and tube outer dimeter, d_0 are two independent design variables that are often user defined. Thus, they are selected for the parametric study. The presentation of shell geometry is simplified using shell aspect ratio, AR, where $AR = \frac{L}{D_{sh,i}}$.

The range of variable design parameters is listed in Table 3 and the constant design parameters are listed in Table 4.

Table 3: Varied design parameters of SulfurTES battery

$d_o(\mathbf{m})$	$d_i(\mathbf{m})$	$D_{sh,i}(\mathbf{m})$	# of tube	L(m)	Shell AR	<i>Bs</i> (m)
0.06 (2")		0.93	114	8.52	9.00	0.186
	0.055	1.0	133	7.31	7.00	0.2
	0.055	1.2	198	4.91	4.00	0.24
		1.4	275	3.53	2.5	0.28
		1.05	36	9.61	9.00	0.21
0.114 (4")	0.100	1.2	50	6.92	7.00	0.24
	0.108	1.4	70	4.94	4.00	0.28
		1.55	88	3.93	2.5	0.31
0.168 (6")	0.162	1.11	17	9.82	9.00	0.22
		1.2	20	8.35	7.00	0.24
		1.4	29	5.76	4.00	0.28
		1.6	40	4.17	2.50	0.32

Table 4: Constant design parameters of SulfurTES battery

ca	torage pacity MWh)	P_r	Tube layout angle (°)	% <i>Bc</i>	Diametral clearance in baffle hole (mm)	Inside shell to baffle clearance (mm)	Tube bundle to shell clearance (mm)
	1	1.25	30	30	0.8	0	20

The performance of SulfurTES battery was investigated for specific operating conditions of the charge/discharge temperature, T_C/T_D , charge/discharge period and mass flow rate of HTF. The charge/discharge temperatures were selected as 600 °C and 50 °C, respectively, to investigate the SulfurTES performance for the temperatures relevant for low to high temperature applications. A 6-hour charge period was selected for all test cases, to simulate the average time period available for the solar thermal charging,

followed by a 12-hour discharging. Since the parametric study was conducted independent of any specific heat source and/or application, selection of an appropriate range of operating HTF mass flow rate relevant to the 1-MWh storage capacity was necessary. Initially, we defined a reference mass flow rate as:

$$\dot{m}_{ref} = \frac{Q_{store}}{C_{p,f}(T_C - T_D)t} \tag{1}$$

where Q_{store} is the storage capacity and t refers to the charge/discharge time. For a 1-MWh system, $\dot{m}_{ref} = 0.276 \, kg/s$ for 6-hour charging and 0.138 kg/s during 12-hour discharging. The actual mass flow rate was determined based on the \dot{m}_{ref} . A non-dimensional mass flow rate, \dot{m}^* , was defined to represent the actual mass flow rate, wherein, $\dot{m}^* = \dot{m}_{act}/\dot{m}_{ref}$, and \dot{m}_{act} stands for the actual mass flow rate used for that specific test case. For this study, we selected \dot{m}^* in the range of 0.5-1.5, which corresponds to the of energy supply of 0.5 to 1.5 times of the storage capacity.

Within the parametric space consisting above discussed design parameters and mass flow rates, the comparison of important non-dimensional parameters for 10-kWh and 1-MWh system, is presented in Table 5. This comparison demonstrates the operational similarity between these systems.

Table 5: Non-dimensional parameters of sulfur side and shell side heat transfer

	Sulfu	r <i>Ra</i> #	HTF Re #
Applicable range of used correlations	0 - 3.6	1 - 10 ⁵	
10 kWh system	0 - 1.38	6.26×10^3 - 1.16×10^4	
1 MW/s most one	$d_0 = 0.06 \ m$	$d_0 = 0.168 m$	$- 5.97 \times 10^3 - 1.78 \times 10^4$
1 MWh system	$0 - 1.99 \times 10^7$	$0 - 8.56 \times 10^{8}$	- 5.97 x 10°- 1.78 x 10°

Table 5 shows that ranges of sulfur Rayleigh number for both systems are within the allowable range of correlations provided by Nithyanandam et al. [34,50], and are all in laminar regime ($Ra < 10^{11}$ [53]). The HTF flow in both systems is laminar based on the Reynolds numbers ($Re < 10^5$ [46]), and is in the allowable range of Reynolds number for the Bell-Delaware method [45]. The slowest HTF flow appears in the system with $d_o = 0.168 \ m$, $AR = 2.5 \ and \ \dot{m}^* = 0.5$, yielding the lower bound on HTF Reynolds number ($Re = 5.97 \times 10^3$). The upper bound ($Re \# = 1.78 \times 10^4$) is obtained from system with $d_o = 0.06 \ m$, AR = 9 and $\dot{m}^* = 1.5$.

Performance characterization

The system level performance is represented by a set of energetic efficiencies, including storage capacity utilization, charge/discharge utilization, roundtrip efficiency, and charge/discharge exergetic efficiency. The performance of systems within the design space discussed in the previous section were obtained with varying \dot{m}^* . Such analysis

provided an assessment on SulfurTES performance with different design configurations, under varied operating conditions.

Energetic efficiencies

Energetic efficiency during charging is characterized by storage capacity utilization and charge utilization. The storage capacity utilization shows the percentage of storage capacity that has been utilized at the end of charging, expressed as:

$$U_{Capacity} = \frac{Energy stored in sulfur and tube}{Energy storage capacity} = \frac{m_s C_{p,s} (T_s - T_D) + m_t C_{p,t} (T_t - T_D)}{m_s C_{p,s} (T_C - T_D) + m_t C_{p,t} (T_C - T_D)}$$
(2)

And charge utilization is expressed as:

$$U_C = \frac{Net \ stored \ energy}{Energy \ supplied} = \frac{\int_0^{t_C} m_f C_{p,f} (T_c - T_{out,c}) dt - \int_0^{t_C} h_{loss} A_{surf} (T_{ins} - T_o) dt}{\int_0^{t_C} m_f C_{p,f} (T_C - T_D) dt}$$
(3)

which is the ratio between net stored energy (energy absorbed minus heat loss) and energy provided by HTF [54].

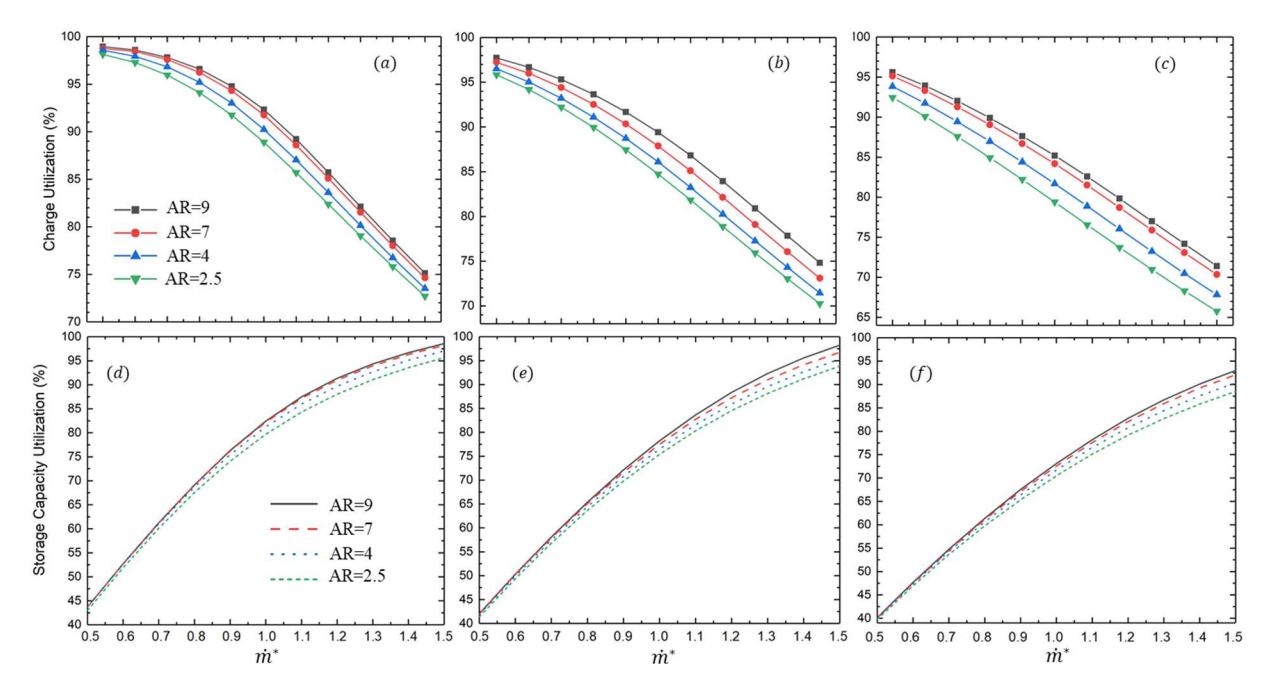


Figure 30 - Charge utilization for (a) $d_o = 0.06$ m, (b) $d_o = 0.114$ m, (c) $d_o = 0.168$ m and storage capacity utilization for (d) $d_o = 0.06$ m, (e) $d_o = 0.114$ m, (f) $d_o = 0.168$ m with varying \dot{m}^*

As shown in Figure 30, with increase in \dot{m}^* from 0.5 to 1.5, the charge utilization decreases from near 100% to around 70% while storage capacity utilization increases from about 40% and approaches 100%. Such observation is explained in the perspective of energy supply, where low mass flow rate provides small amount of energy, keeping the system at low capacity utilization and low temperature. Therefore, because of the low system temperature, a relatively large temperature difference stays between HTF and the system, providing high potential for energy transfer, so that a higher charge utilization can be achieved. The charge utilization keeps decreasing with increasing \dot{m}^* as system

approaching saturation (storage capacity utilization approaches 100%), additional energy supply becomes difficult to absorb.

Geometric dependency is also observed here where longer AR yields higher charge utilization and a higher capacity utilization, around 5%. Because system with longer AR has smaller flow area and higher flow velocity, producing a higher shell side heat transfer coefficient that leads to better thermal performance. Systems with smaller tubes ($d_0 = 0.06$ m) show better thermal performance comparing to ones with larger tubes ($d_0 = 0.168$ m). It is because an increased amount of tubes is required for a system with smaller tubes that provides a larger interface area for the heat transfer between HTF and tube/sulfur to occur.

In general, capacity utilization is positively related to mass flow rate (amount of energy supply), while the opposite is true for charge utilization. System geometry that produces superior shell side heat transfer performance (long shell *AR* or small tube size) are beneficial to thermal performance during charging.

Energetic performance of discharging is quantified by the discharge utilization, which refers to the percentage of energy recovered from discharging by net stored energy from charging, expressed as:

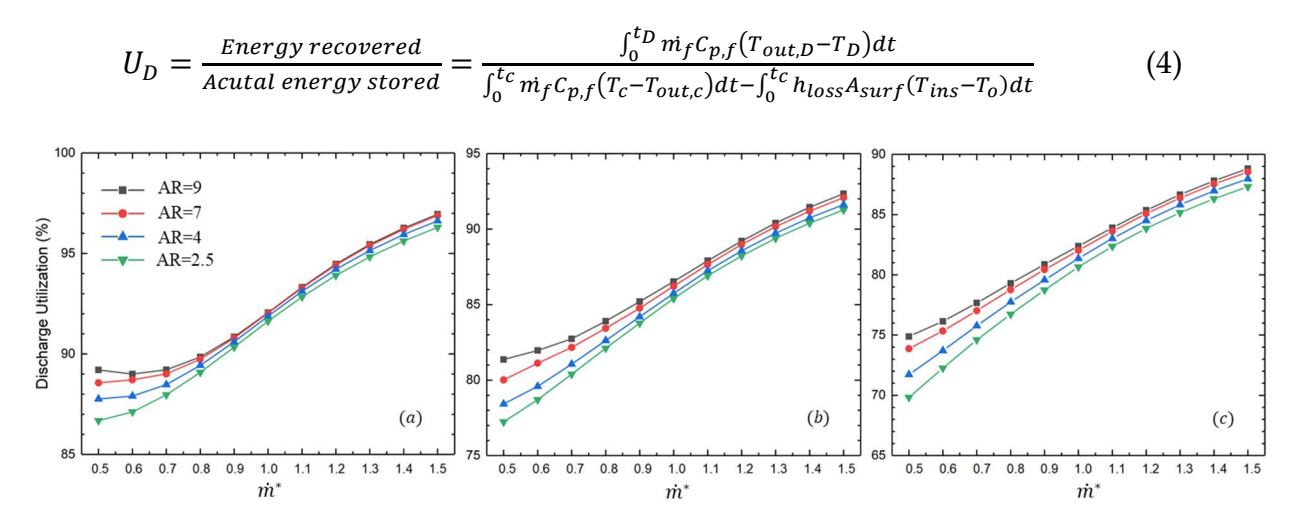


Figure 31 - Discharge utilization for (a) do =0.06 m, (b) do =0.114 m, (c) do =0.168 m with varying \dot{m}^*

Discharge utilization for all configurations with varying mass flow rates are presented in Figure 31. Variation in discharge utilization with varying shell aspect ratio and tube diameter follows a similar trend as what has been observed for charge utilization. Opposite to charge utilization, discharge utilization varies positively with increasing mass flow rate. It is because that higher mass flow rate leads to higher rate of energy recovery, extracting larger amount of stored energy within the same time span.

The roundtrip efficiency provides insight into the system's energetic performance of the complete thermal cycle. It is defined as the ratio of energy recovered from discharging to energy supplied during charging. Mathematically, it is also the product of charge and discharge utilization with the following expression [54]:

$$U_{roundtrip} = U_c \times U_D = \frac{Energy\ recovered}{Energy\ supplied} = \frac{\int_0^{t_D} m_f C_{p,f}(T_{out,D} - T_D)dt}{\int_0^{t_C} m_f C_{p,f}(T_C - T_D)dt}$$
(5)

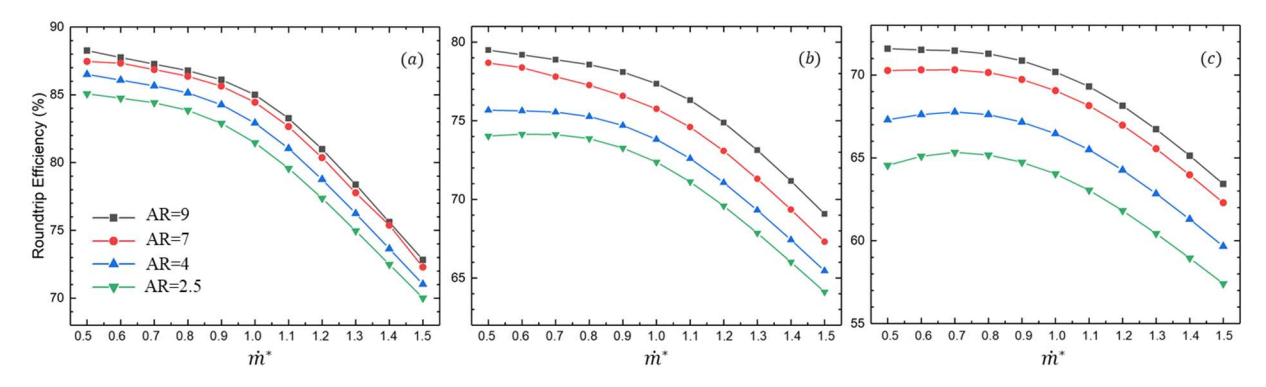


Figure 32 – Roundtrip energetic efficiency for (a) d_0 =0.06 m, (b) d_0 =0.114 m, (c) d_0 =0.168 m with varying \dot{m}^*

As seen in Figure 32, roundtrip efficiency stays relatively constant when \dot{m}^* is less than 1, followed by a drop as \dot{m}^* increasing beyond 1. Since the charge/discharge utilization is negatively/positively related to mass flow rate respectively, their combined effect yields a somewhat similar roundtrip efficiency with \dot{m}^* less than 1. As \dot{m}^* increasing beyond 1, the system is highly charged ($U_{Capacity} > \sim 75\%$), prominent decrease in charge utilization dominates the change in roundtrip efficiency, causing the drop. Geometric dependency of roundtrip efficiency shows similar trend to that of charge/discharge utilization as expected, where larger AR and smaller tube size bring higher roundtrip efficiency.

In summary, the increase in mass flow rate provides improved discharge utilization, but the energetic efficiency of thermal cycle may be restricted by energy waste during charging that lowers the charge utilization and thus, lowers the roundtrip efficiency. Discharge performance

Exergetic efficiencies

The exergetic efficiency provides an assessment on how closely the system operates near ideal condition where all useful work can be acquired [56,57]. The definition of charge exergetic efficiency is analogous to that of charge utilization, presenting the ratio of exergy stored, equivalent to exergy absorbed minus exergy destruction, and exergy provided, expressed as [54]:

$$\phi_{c} = \frac{Acutal\ exergy\ stored}{Exergy\ supplied} = \frac{\int_{0}^{t_{C}} \dot{m_{f}} C_{p,f} \left(\left(T_{C} - T_{out,c} \right) - T_{O} \ln \left(\frac{T_{C}}{T_{out,c}} \right) \right) dt - \frac{\dot{m_{f}} W}{\eta} t_{C}}{\int_{0}^{t_{C}} \dot{m_{f}} C_{P,f} \left(\left(T_{C} - T_{O} \right) - T_{O} \ln \left(\frac{T_{C}}{T_{O}} \right) \right) dt}$$
(6)

The term, $\frac{m_f W}{\eta} t_C$ represents the amount of exergy destruction by compressor work. The work required in compressing air, W, can be calculated as the specific work of isentropic compression of an ideal gas from 1 atm to 1 atm + ΔP_{sh} . η is the product of

compressor efficiency and energy conversion efficiency. Detailed derivation of exergy destruction due to pump work can be found in reference [55,57].

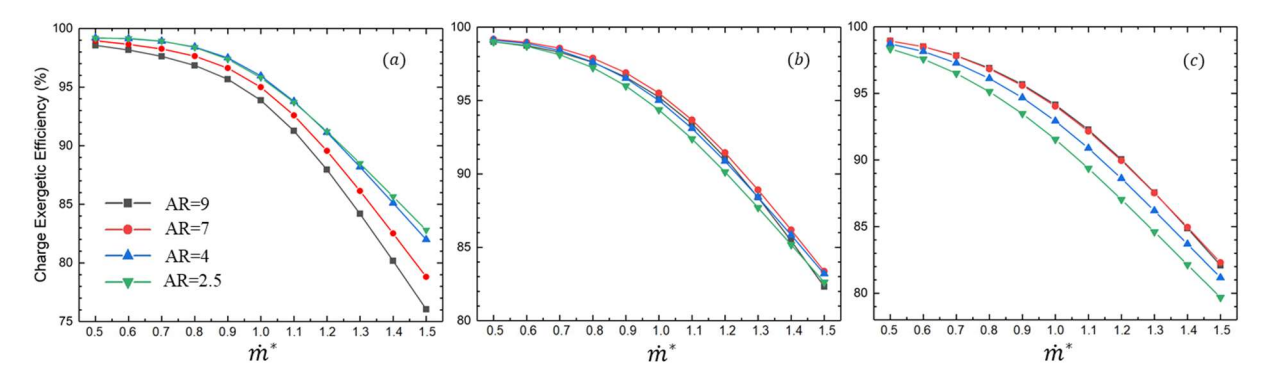


Figure 33 - Charge exergetic efficiency with varying \dot{m}^* for (a) d_o = 0.06 m, (b) d_o = 0.114m, (c) d_o = 0.168 m

It is observed from Figure 33 that, the dependency of charge exergetic efficiency on mass flow rate is similar to that of charge utilization. The system's ability in efficiently absorbing useful work decreases with increase in the mass flow rate or system temperature. However, its dependency on shell aspect ratio and tube diameter is different from that of charge utilization. Shown in Figure 33 (a), system with $d_o = 0.06$ m and AR = 9 has the lowest charge exergetic efficiency within the studied range of mass flow rate, whereas this system configuration posses the highest charge utilization through the entire range of mass flow rate (Figure 30 (a)). The lowered exergetic efficiency is caused by exergy destruction from pump work. Although, a larger AR provides better heat transfer performance that is beneficial to exergy absorption, it also requires higher pump

work due to increased flow velocity and pressure drop. Therefore, with tube diameter decreasing and shell AR increasing, the amount of exergy destruction overcomes the benefit of better heat transfer performance, leading to an inverse relationship with charge exergetic efficiency. The effect of pump work diminishes when tube size increases. For instance, the charge exergetic efficiency of systems with $d_0 = 0.114$ m and AR = 9 nearly merges with that of the system whose AR = 4, while system with $d_0 = 0.168$ m, AR = 9 provides similar results as that by AR = 7.

The discharge exergetic efficiency is defined by the ratio of net available exergy in the system to the initial exergy stored in the system [54], shown in Eq. (7). The net available exergy is the summation of recovered exergy and remaining exergy with exergy destruction excluded.

$$\phi_{D} = \frac{Exergy \, remaining + Ex}{Exergy \, stored} \frac{recovered - Exe}{Exergy \, stored}$$

$$= \frac{m_{s}C_{p,s}\left((T_{s} - T_{D}) - T_{o}ln\left(\frac{T_{s}}{T_{D}}\right)\right) + m_{t}C_{p,t}\left((T_{t} - T_{D}) - T_{o}ln\left(\frac{T_{t}}{T_{D}}\right)\right)}{m_{s}C_{p,s}\left((T_{i,s} - T_{D}) - T_{o}ln\left(\frac{T_{i,s}}{T_{D}}\right)\right) + m_{t}C_{p,t}\left((T_{i,t} - T_{D}) - T_{o}ln\left(\frac{T_{i,t}}{T_{D}}\right)\right)}$$

$$+ \frac{\int_{0}^{t_{D}} m_{f}C_{p,f}\left((T_{out,D} - T_{D}) - T_{o}ln\left(\frac{T_{out,D}}{T_{D}}\right)\right) dt - \frac{m_{f}W}{\eta}t_{D}}{m_{s}C_{p,s}\left((T_{i,s} - T_{D}) - T_{o}ln\left(\frac{T_{i,s}}{T_{D}}\right)\right) + m_{t}C_{p,t}\left((T_{i,t} - T_{D}) - T_{o}ln\left(\frac{T_{i,t}}{T_{D}}\right)\right)}$$

$$(7)$$

where $T_{i,s}$ and $T_{i,t}$ are initial sulfur and tube temperature at the beginning of discharging.

Figure 34 presents time dependent discharge exergetic efficiency, symbolled as ϕ_D , for six system configurations, covering upper and lower limits of shell AR and all three tube sizes. As discharging proceeds, an increasing amount of exergy has been recovered from the system, while the amount of exergy remained in the system decreases. When the stored exergy is nearly drained, further decrease in the remaining exergy and further increase in the exergy recovery approach cessation, leading to a plateau in the change of ϕ_D with time. For system with small shell AR (AR=2.5), ϕ_D plateaus at values in a descending order with mass flow rate. For instance, the system with shell AR=2.5 and do = 0.06 m, ϕ_D decreases from nearly 100% and plateaus at around 60% for \dot{m}^* =1.5 and around 45% for \dot{m}^* =0.5. It is because discharging with higher mass flow rate provides high-temperature exhaust at a faster rate, yielding larger amount of exergy recovery. Long time into discharging, exergy remaining approaches zero, the amount of exergy recovery dominates the value of ϕ_D . Therefore, by providing higher amount of exergy recovery, discharging with higher mass flow rate yields higher ϕ_D . In contrast, the above described dependency of ϕ_D on mass flow rate is not true for large shell AR (AR=9) due to prominent effect of exergy destruction from pump work. As discussed in charging performance section, large shell AR, small tube size and high mass flow rate lead to high pump work. Although high mass flow rate still provides high exergy recovery, exergy destruction is prominent to worsen the exergetic efficiency. As shown by Figure 34, for system with shell AR=9 and do=0.06 m, with $\dot{m}^*=1.5$, ϕ_D starts from about only 70%, drops quickly to less than 40% in 3 hours and reaches the plateau, whereas for the same system with $\dot{m}^*=0.5$, ϕ_D drops from near 100%, and slowly approaches 40% in 12 hours.

In summary, this section examined performance of SulfurTES systems in terms of energetic and exergetic efficiencies. Both efficiencies are related to system's thermal performance where larger shell aspect ratio with smaller sized tubes provides better HTF side heat transfer that generally is beneficial to the system performance. However, better heat transfer requires higher pump work with higher exergy destruction. Therefore, the following section suggests a design strategy that helps provide a balanced system design, considering all aspects of system performance.

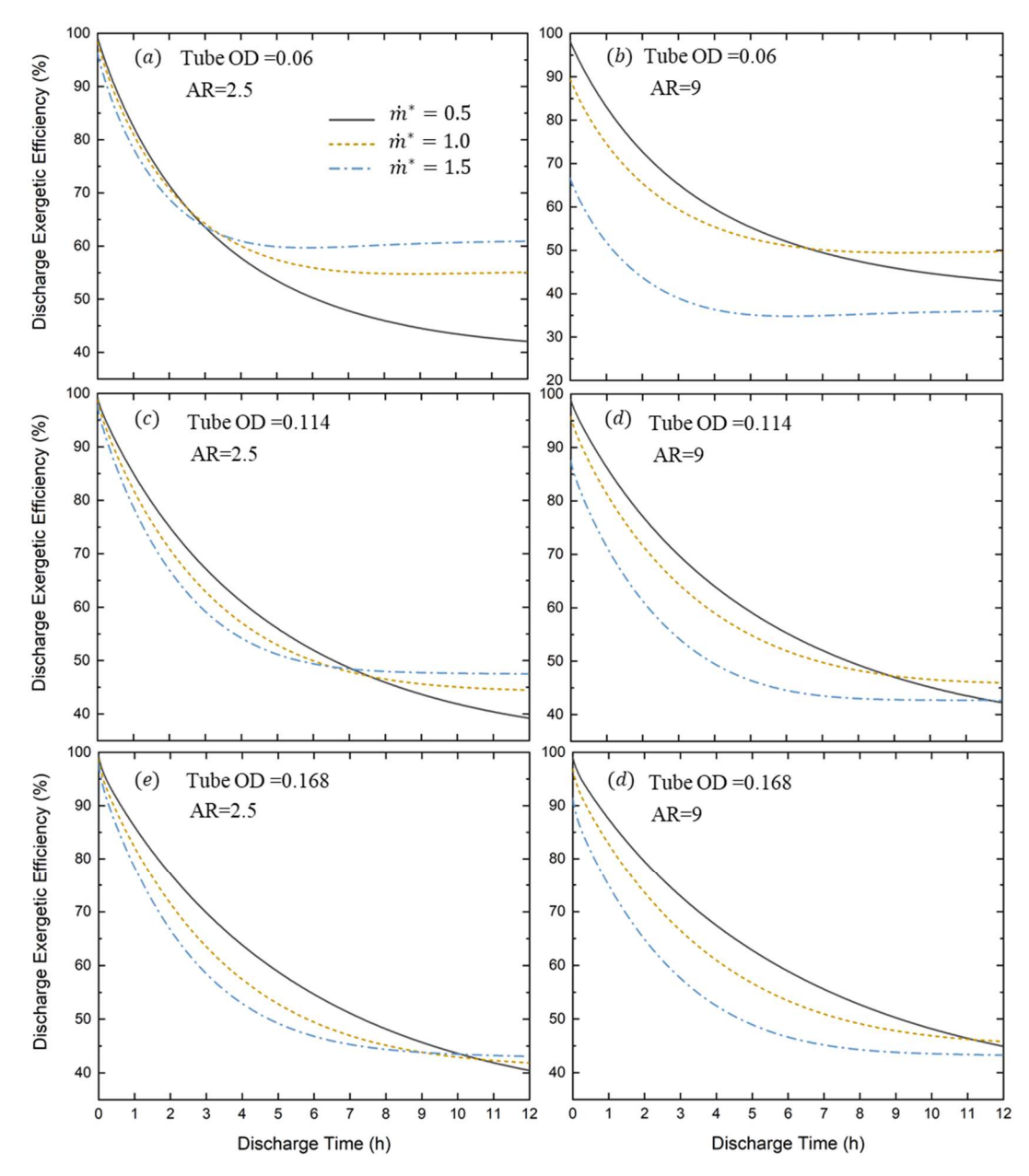


Figure 34 - Discharge exergetic efficiency for different system configurations with (a) d_o = 0.06 m and AR = 2.5 (b) d_o = 0.06 m and AR = 9 (c) d_o = 0.114 m and AR = 2.5 (d) d_o = 0.114 m and AR = 9 (e) d_o = 0.168 m and AR = 2.5 (f) d_o = 0.168 m and AR = 9 with varying mass flow rate

4.2. System design strategy

The above performance characterization of SulfurTES system shows trade-offs between different performance parameters, where an optimum design or operation that optimizes all performance parameters may never exist. Therefore, the following section presents a design procedure that produces a balanced design and operation, so that each performance parameter is above specific requirement.

The proposed design procedure assumes known actual mass flow rate, operating temperature range and desired tube size as input parameters with a design space, unique to user defined performance requirements. The determination of such design space is documented here as well. The design space is composed by upper and lower limits on \dot{m}^* over a range of shell AR to indicate appropriate range of system design that satisfies the user desired performance.

Example system designs are presented in appendix B to demonstrate the use of design procedure discussed here. The first design example in appendix B illustrates the process of system design with specific working condition, and the second one presents the process of working condition selection for an existing system to achieve satisfactory performance.

System design procedure

Following the design procedure, the storage capacity is firstly determined within the first iteration loop. Based on the storage capacity, the shell geometry is then provided following the second iteration loop, outputting shell inner diameter, corresponding baffle spacing, number of tubes and shell length. The flow chart presents the above-described design procedure in detail.

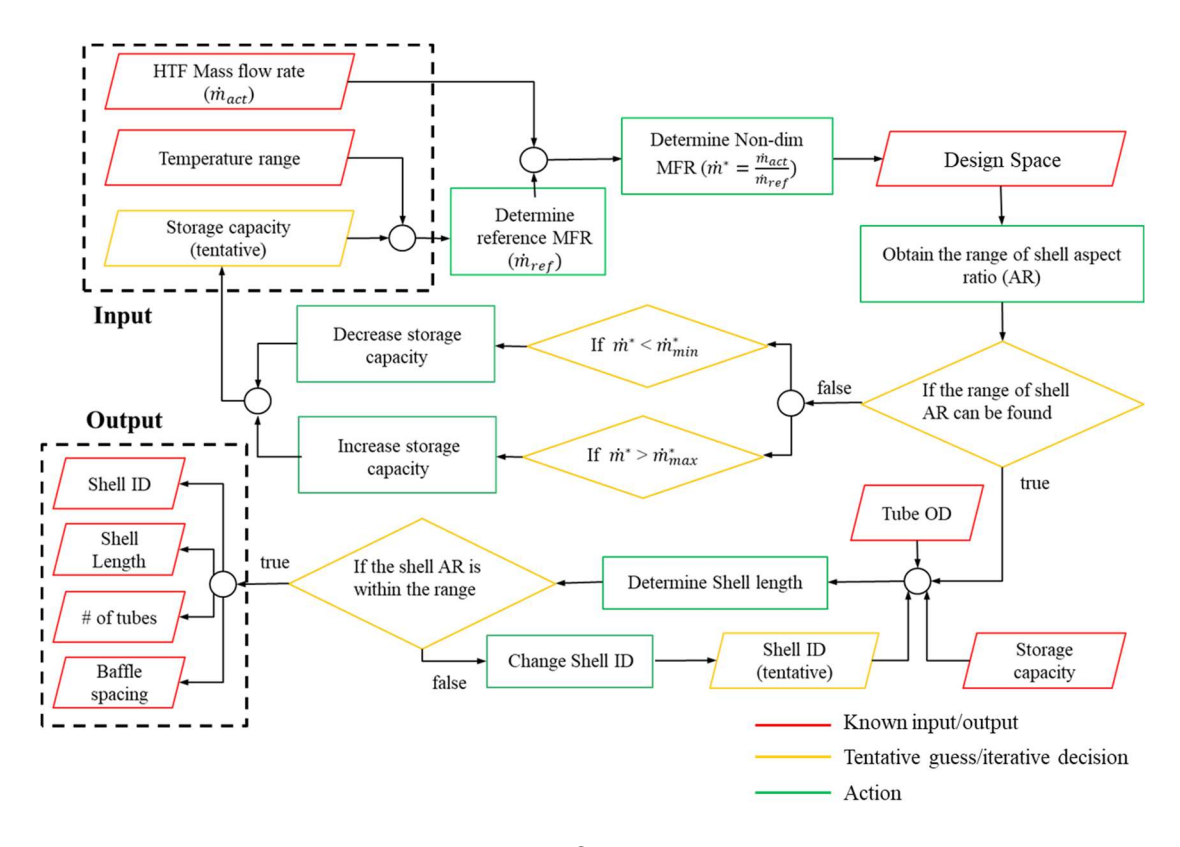


Figure 35 - Flow chart of system design procedure

Red colored input/output parameters denote to those that are known from users or the decided outcome from the process, whereas yellow colored ones refer to tentative guesses, requiring iterations. Actions are in green color. The design process commences by determining the storage capacity with an initial guess. Based on the tentative storage capacity, compute the non-dimensional mass flow rate. If the above obtained \dot{m}^* falls within the design space, the range of shell AR can be determined. If not, the iteration shall proceed till a reasonable storage capacity is found to have \dot{m}^* fallen within the design space, providing a range of shell AR appropriate to this specific \dot{m}^* .

The following second iteration loop aims to determine the complete shell geometry based on the storage capacity and range of shell AR. The loop starts by providing a guess of shell inner diameter, $D_{sh,i}$. With known storage capacity and tube size, calculate the shell length and corresponding shell AR. If the shell AR falls in between the AR range obtained from last step, the design process is concluded, outputting all necessary geometric parameters. If not, change the value of $D_{sh,i}$, and iterate the second loop till the shell AR falls into that range.

Design space determination

Seen in the previous section, the design space is an important input to the design procedure, as it demonstrates the appropriate geometric and operational range that satisfy users' requirements. This section presents the procedure of finding upper and lower bounds of operating mass flow rate over a range of shell AR to satisfy the system

performance requirements. Since the system level performance is characterized by a set of performance parameters, a successfully designed system should satisfy requirement on each performance parameter. Table 6 shows a set of example requirements of performance parameters. It is a representative example, serving demonstrative purpose.

Table 6: Example set of performance requirements

$U_{\it Capacity}$	U_c	$\phi_{\it C}$	$U_{\scriptscriptstyle roundtrip}$	$\phi_{\scriptscriptstyle D}$
>= 75%	>= 80%	>= 85 %	>= 68%	>= 50% in 8 h

As discussed in section 4.1, except ϕ_D , the rest four of the performance parameters in Table 6 change monotonically with changing mass flow rate, where $U_{capacity}$ increasing and U_C , ϕ_C and $U_{roundtrip}$ decreasing with increasing mass flow rate. Therefore, requirement on $U_{capacity}$ yields a lower bound on mass flow rate, \dot{m}_{min}^* .

As shown in Figure 36, \dot{m}_{min}^* should be around 0.85 for shell AR = 9.7 and 4 and 0.9 for shell AR = 2.5 to have $U_{capacity}$ being higher than 75%.

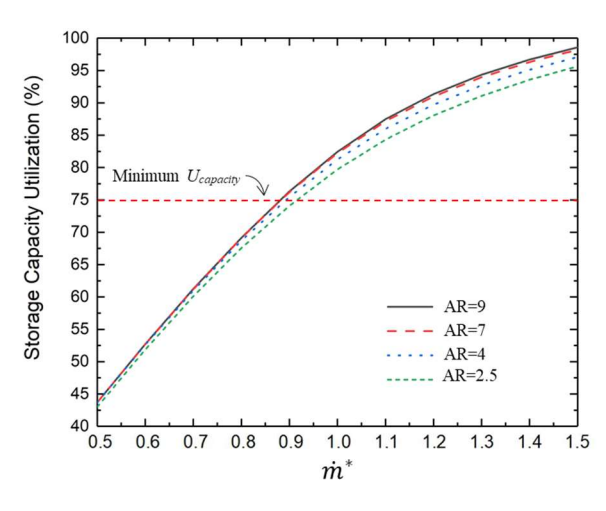


Figure 36 - Storage capacity utilization for systems with d_0 = 0.06 under varying mass flow rate

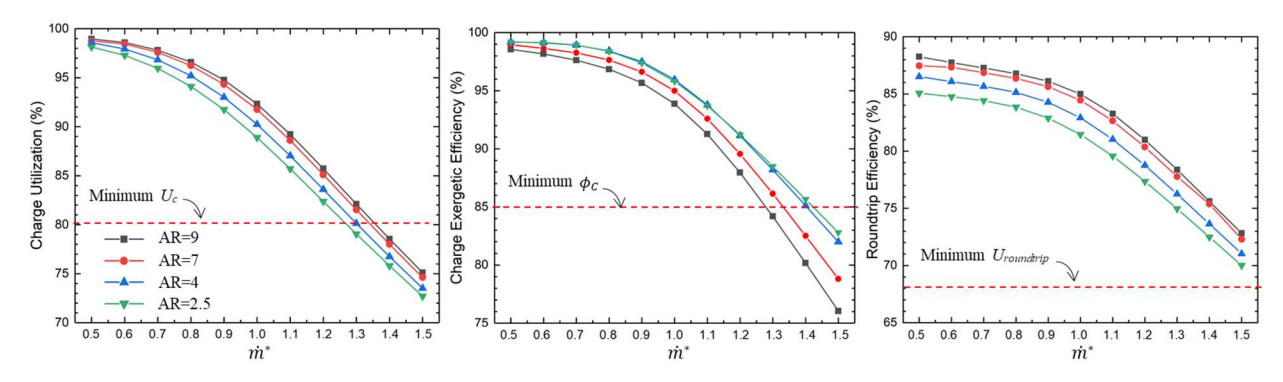


Figure 37 - (a) charge utilization, (b) charge exergetic efficiency, (c) roundtrip efficiency for systems with $d_o = 0.06$ m under varying mass flow rate

 \dot{m}_{max}^* is found comparing requirements of U_C , ϕ_C and $U_{roundtrip}$. Figure 37 shows that, as \dot{m}^* increases, U_C reaches its requirement of 85% firstly while the other two performance parameters are still above required values. Therefore, based on the restriction on U_C , the upper bound, \dot{m}_{max}^* , is found to be 1.25, 1.35, 1.3, and 1.3 for shell AR = 2.5, 4, 7, and 9, respectively.

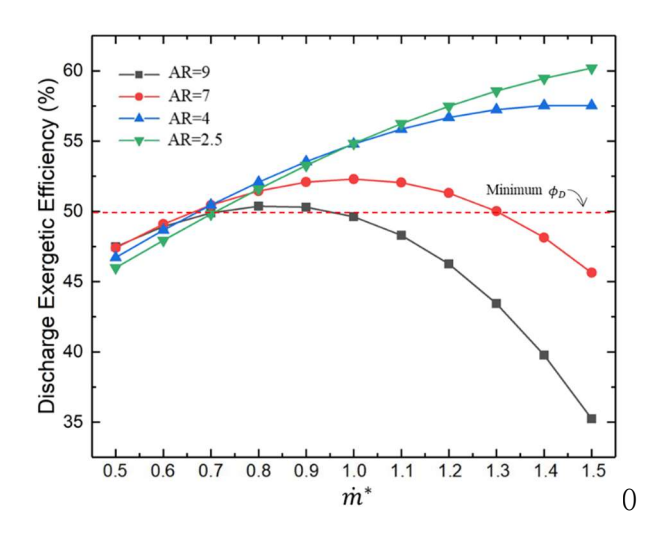


Figure 38 - Discharge exergetic efficiency of systems with d_o = 0.06 m at 8 hours into discharging under varying mass flow rate

Figure 38 shows the discharge exergetic efficiency of systems with different shell AR at eight hours of discharging for a range of mass flow rates. As shown in Figure 38, ϕ_D does not vary monotonically with \dot{m}^* when shell AR is large (AR=7,9) due to significant exergy destruction by pump work. Therefore, a range of \dot{m}^* exists (between $\dot{m}_{\phi_D,min}^*$ and $\dot{m}_{\phi_D,max}^*$) that satisfies the requirement of ϕ_D . For systems with smaller shell AR (AR=2.5,4), $\dot{m}_{\phi_D,max}^*$ is not available in the current range of mass flow rate, therefore, only an $\dot{m}_{\phi_D,min}^*$ is needed to meet ϕ_D requirement. By observing ϕ_D variation with mass flow rate, \dot{m}^* is determined to be between 0.7 and 1 for shell AR=9, or between 0.7 and 1.3 for shell AR=7. But for systems with shell AR=2.5 and 4, having a \dot{m}^* larger than 0.7 satisfies the above-mentioned requirement within the current range of mass flow rate.

Comparing \dot{m}_{min}^* and \dot{m}_{max}^* , obtained based on requirements for the first four performance parameters, to $\dot{m}_{\phi_D,min}^*$ and $\dot{m}_{\phi_D,max}^*$, determined by requirement of ϕ_D , the range of \dot{m}^* that satisfies all five parameters can be found. The smaller among \dot{m}_{max}^* and $\dot{m}_{\phi_D,max}^*$, is set to be the upper limit on \dot{m}^* , and the larger one among $\dot{m}_{\phi_D,min}^*$ and \dot{m}_{min}^* is chosen as the lower limit on \dot{m}^* .

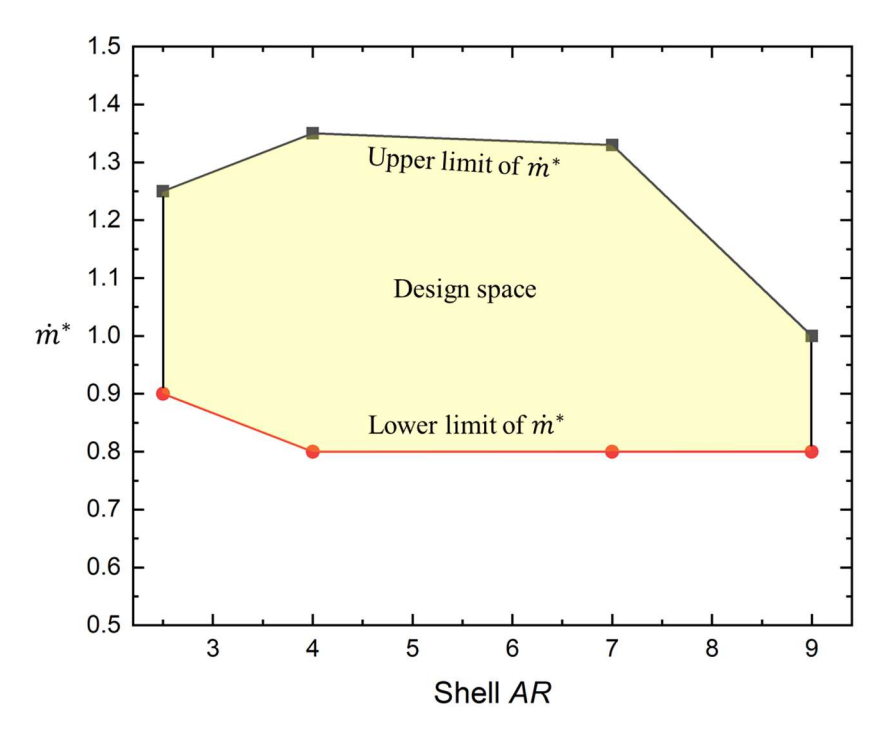


Figure 39 - Determined design space unique to performance requirements

Based on above described comparison, lower and upper bounds of \dot{m}^* for each corresponding shell AR are determined and presented on Figure 39(a) with d_o = 0.06 m. The area between curves of upper and lower limit of \dot{m}^* composes the design space that meets the specified performance requirements listed in Table 6. It is observed that with

shell AR between 4 and 7, the design space is relatively wider where \dot{m}^* can be between 0.8 and 1.3 to safely meet performance requirements. The design space narrows down with shell AR smaller than 4, due to restriction on charge utilization, and with shell AR larger than 7, due to restriction on exergetic efficiency. Therefore, the recommended range of shell AR is between 4 and 7 to accommodate wide range of operating condition.

4.3. Conclusions

A transient two-dimensional numerical model is developed to characterize the performance of the SulfurTES system. This model is validated using the demonstration results of the laboratory-scale SulfurTES thermal battery, with around 5% error. This high-fidelity model is used to conduct a parametric study on key parameters, including tube size, shell aspect ratio, and mass flow rate of HTF. Overall, the results reveal a large design space for SulfurTES thermal batteries with attractive performance. By characterizing the system level performance with charge/discharge utilization, charge/discharge exergetic efficiency, roundtrip efficiency and storage capacity utilization, the following conclusion can be made:

1. Increase in mass flow rate is beneficial to capacity utilization where increased amount of energy is supplied to have the storage capacity fully utilized.

- 2. Increase in mass flow rate lowers the potential of energy transfer that leads to monotonically decreasing charge utilization and charge exergetic efficiency.
- 3. Increased mass flow rate yields higher rate of energy recovery during discharging, leading to an increase in discharge utilization.
- 4. The combined effect of charge and discharge utilization leads to small variation in roundtrip efficiency with $\dot{m}^* < \sim 1$. Further increase in mass flow rate yields lower charge utilization that in turn lowers the roundtrip efficiency.
- 5. High mass flow rate is in favor of discharge exergetic efficiency as large amount of exergy can be recovered.
- 6. Large shell *AR* and small tube size are beneficial to HTF heat transfer performance that leads to improved system level performance. But care should be taken with large mass flow rate as exergy destruction can be significant that lowers the exergetic efficiency.

Following the parametric study, a system design strategy is suggested with a process in finding the design space unique to user specified performance requirements, and an iterative design procedure that uses the determined design space to finalize storage capacity and shell geometry. It is observed that the shell *AR* should be between 4 and 7 to have relatively wider range of selection in operating mass flow rate.

The current study not only showed performance of SulfurTES system in various aspects for the first time, but also presented a systematic approach for investigating performance of TES system, correlating operating condition with storage capacity and selecting geometric design with regularity. It developed a framework for future study in performance enhancement with varied system configurations, and a sound basis for system cost analysis.

Chapter 5 Performance enhancement considerations and cost analysis

The last chapter presents the performance of SulfurTES system in single-tank thermal battery configuration operating under various flow rate of HTF (air) within temperature range of 50 °C - 600°C. We observed that systems with small tubes (d_o =0.06 m) generally have superior thermal performance due to larger interface area and higher shell side heat transfer coefficient. If the same process in determining design space for system with large tubes (d_o =0.168 m) is carried out for the same set of performance requirements listed in Table 6, the design space becomes much smaller, shown in Figure 40. Obviously, this small design space is undesirable because it accommodates very limited applications and will probably disappear if higher energetic efficiency is required.

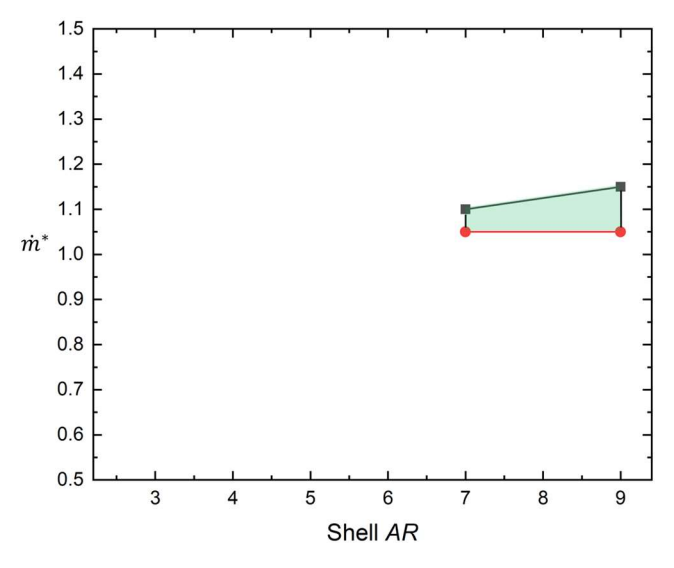


Figure 40 - Design space determined for system with large tubes (d_o =0.168 m)

However, system with large sized tubes are desirable for large-scale systems because of the low usage on containment material that leads to low system cost. Therefore, performance enhancement for systems with large tubes is essential to realize advantageous cost characteristics of SulfurTES systems. To achieve the overarching objective, we investigated system performance with varied system configurations, including the one with two shell passes on the HTF side that leads to increased heat transfer coefficient, and the cascaded configuration where system is constructed with multiple tanks containing different sized tubes. Due to the operational nature of singletank TES system, there will always be a colder region near charging outlet that does not require expensive high-temperature resistant containment material. Therefore, the single-tank system can be divided into multiple tanks with different tube materials based on their operational temperature ranges. The tank operates at lower temperature range can utilize smaller sized tubes made with cheaper material that increases the heat transfer area without increasing the system cost. Next, we studied heat transfer variation with different types of HTFs, including sCO2 and HITEC molten salt, with potentially high heat transfer coefficient because of their thermal properties. The performance enhancement of SulfurTES system is observed, and used to conduct a cost analysis. The analysis compares the cost of SulfurTES in thermal battery configuration and conceptual two-tank configuration (analogues to two-tank molten salt TES) to existing molten-salt TES system, assuming integration with CSP-Trough plant and Power tower in a wide range of plant capacities, to quantify the significant cost reduction in both capital TES cost and levelized cost of energy (LCOE).

The current study evaluates possible solutions in enhancing HTF side thermal performance that can be applied to not only SulfurTES, but also other single-tank TES systems with encapsulated storage medium, and provides an in-depth, realistic cost estimation to manifest the advantageous cost of SulfurTES systems.

5.1. System level performance with varying shell configuration

Two shell passes

Inspired by TEMA E shell design [45] in shell-and-tube heat exchangers, Single-tank SulfurTES systems with two shell passes are designed and studied. Shown in Figure 41 (b), a longitudinal baffle is added to split the shell into two compartments with an open end on one side, makeing the one-way flow path into a round trip to enhance the thermal stratification by increasing shell side flow velocity and heat transfer coefficient.

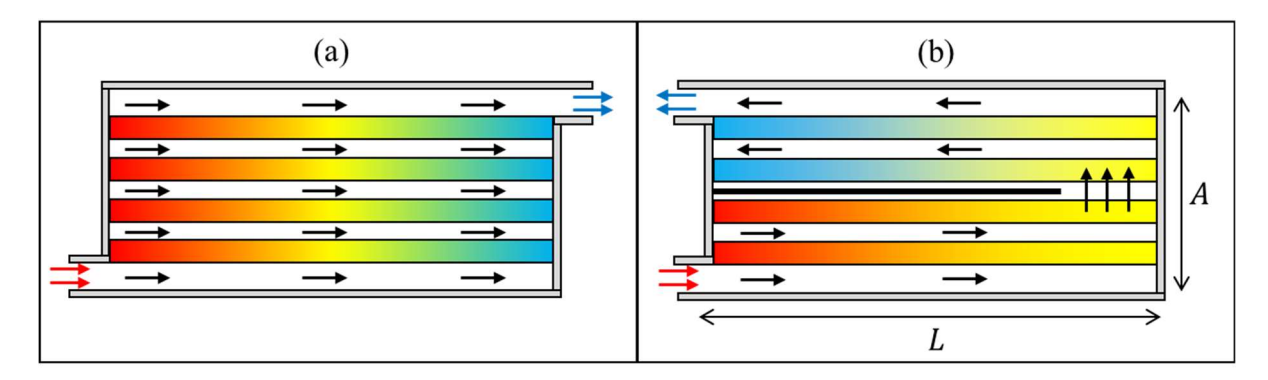


Figure 41 - Charging flow path of (a) single shell pass (b) two shell passes

The effective shell geometry with two shell passes is equivalent to the one with single

shell pass but half in cross-sectional area and double in length, shown in Figure 42. The equivalent shell AR is $2\sqrt{2}$ times the original AR, because $A_{2\;pass} = \frac{1}{2}A_{original} = D_{2\;pass} = \frac{\sqrt{2}}{2}D_{original}$ while $L_{2\;pass} = 2L_{original}$. Therefore, $AR_{2\;pass} = \frac{L_{2\;pass}}{D_{2\;pass}} = \frac{2L_{original}}{\frac{\sqrt{2}}{2}D_{original}} = 2\sqrt{2}AR_{original}$. The increased effective AR leads to higher flow velocity that enhances the shell side heat transfer performance. Additionally, the virtual change in shell AR does not change the system's real geometry, so the larger heat loss associated with larger shell AR (larger surface area) is avoided. One disadvantage of this design is the extra pressure-drop caused by reduced flow area and increased flow path length. The additional pressure-drop by flow turning is neglected in shell-and-tube heat exchanger design [59],

and thus neglected in this study also.

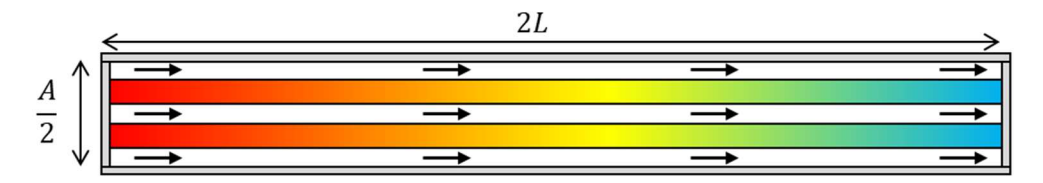


Figure 42 - Equivalent shell geometry change by having two shell passes

The effect of shell pass was investigated by comparing the performance of same systems with one shell pass (original system) and two shell passes (2-pass system). Their specifications can be found in Table 3. The operating temperature range was set to 50 – 600°C and the non-dimensional mass flow rate ranged from 0.5 to 1, as it is enough to present difference in system level performance from underutilized to highly utilized condition without prominent energy waste.

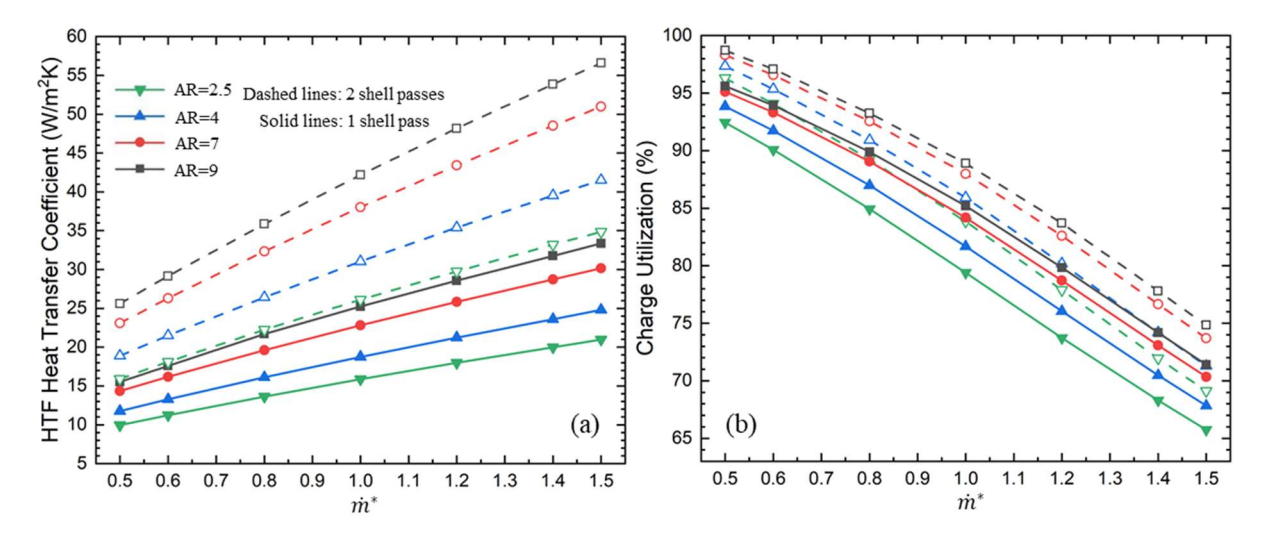


Figure 43 - Comparison of (a) heat transfer coefficient (b) charge utilization between systems with single and two shell passes

Figure 43 (a) shows the variation of shell side heat transfer coefficient with varying mass flow rate. As expected, the heat transfer coefficient increases with increasing mass flow rate and shell AR where higher flow velocity is provided. The additional shell pass increases the heat transfer coefficient to around 1.5 times higher. This is explained by a simple analytical calculation. Since the flow velocity is twice in 2-pass system compared to original system, $Re_{2-pa}=2Re_{1-pass}$. Because $Nu \propto Re^{0.6}Pr^{0.36}$, $Nu_{2-pass}=2^{0.6}Nu_{1-pas}=1.5Nu_{1-p}$, which consequently provides an around 50% increase in the heat transfer coefficient. An around 5% increases in the charge utilization is boosted by the increase in heat transfer coefficient, shown in Figure 43 (b).

Cascaded system

Another method in enhancing shell side thermal performance is to increase the interface area for heat transfer between HTF and tube/sulfur without significantly increase the system cost. As observed from the operation of one-tank system, there is a portion of system near the charge outlet stays at lower temperature during the entire process. It is therefore proposed to replace the one-tank thermal battery with two cascaded tanks. One is made with 0.168 m SS316 tubes as the high temperature tank (hot tank), and the other tank is made with 0.06 m SS 304 tubes as the low temperature tank (cold tank), shown in Figure 44. During operation, the charging flow enters and passes

through the hot tank before entering the cold tank, ensuring low enough flow temperature that is safe for the cold tank. The reduced tube size in cold tank increases the interface area, but the use of cheaper SS 304 prevents the system cost from drastically increasing.

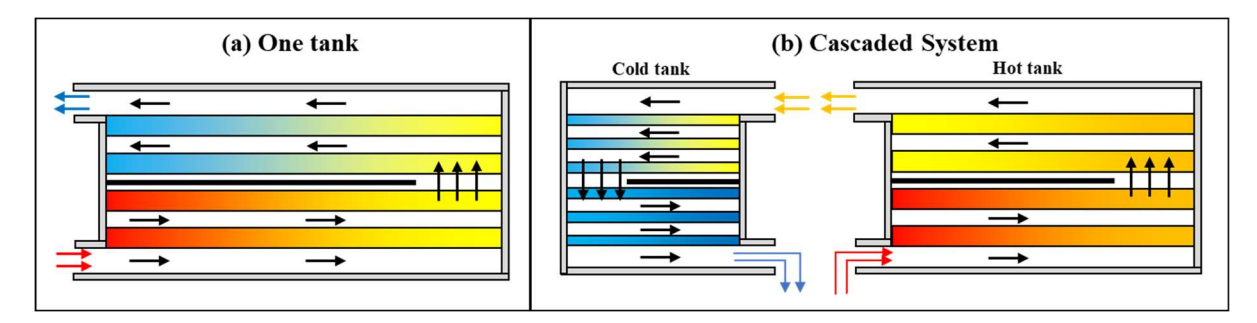


Figure 44 - Charging flow path of (a) two-shell pass one tank system (b) two-shell pass cascaded system

The thickness and highest operating temperature of SS 304 tube are determined comparing hoop stress (Eq. 1) by sulfur vapor pressure and temperature dependent yield stress of SS 304 of 200 MPa.

$$\sigma_{hoo} = \frac{P_s r_o}{r_o - r_i} \tag{1}$$

where P_s refers to the temperature dependent sulfur vapor pressure and r denotes to the radius of tube. The pressure-temperature relationship of sulfur is found based on Figure 13.

Table 7 – Comparison of Hoop and yield stress by sulfur vapor pressure at $600\,^{\circ}\mathrm{C}$

NPS Pipe schedule	Poop stress (MPa)	Yield Stress at 600 °C [60] (MPa)
10	15	
40	11	150
80	8	

Comparing the yield stress of SS 304 at 600 °C to hoop stress of tubes with thickness ranging from sch.10 to 80, it is observed that a large safety margin (factor of safety = 10) exists for thinnest tube (Sch. 10) at 600 °C. According to a further in-house compatibility study, SS 304 is compatible with sulfur below 400 °C, where corrosion is minimum. It is therefore decided to partition the system so that the cold tank stays below 400 °C. Based on the temperature distribution within one-tank thermal battery at the end of charging, the region below 400 °C is around 30% of the system. Therefore, the hot tank in the cascaded system is designed to consist 70% of storage capacity in the current study while the rest 30% comes from the cold tank.

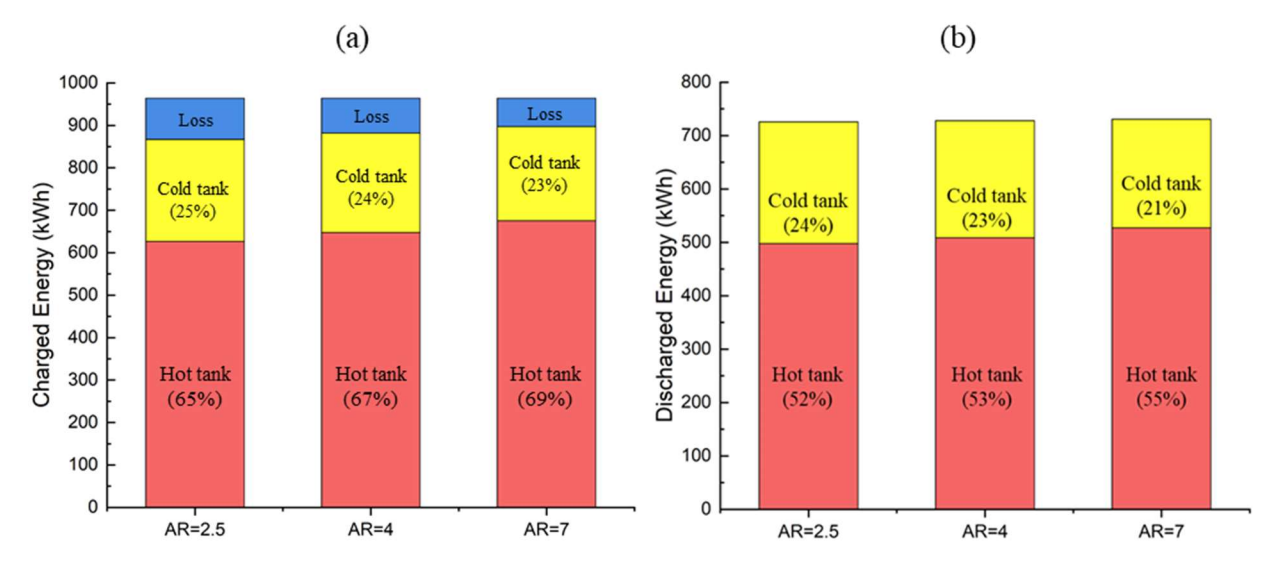


Figure 45 - Energy content in hot/cold tanks with energy loss of cascaded system during (a) charging (b) discharging at $\dot{m}^* = 1$ for systems with shell AR from 2.5 to 7

It is observed from Figure 45 (a) that the energy storage within hot tank increases with shell AR increases, due to higher heat transfer coefficient, which consequently reduces the energy storage in cold tank. But the total amount of energy stored also increases with increasing shell AR. Similar energy distribution is seen from amount of energy discharged. But the total discharged energy only slightly increases for larger shell AR, because the energy within the system is nearly drained, where temperature difference between HTF and the system is small enough to diminish the effect of shell geometry on thermal performance.

Table 8 shows the comparison of interface area of a 1-MWh SulfurTES thermal battery in one-tank and cascaded configurations. The use of smaller tube in cold tank provides

20.8 m² more surface area, equivalent to a 24% increase in the total surface area for heat transfer.

Table 8: Tube surface area comparison between one-tank and cascaded tanks

One tank	Cascaded tanks (m ²)		
Area (m ²)	Hot tank	Cold tank	
00.3	61.8	46.8	
88.2	Total: 108.6 (24% more)		

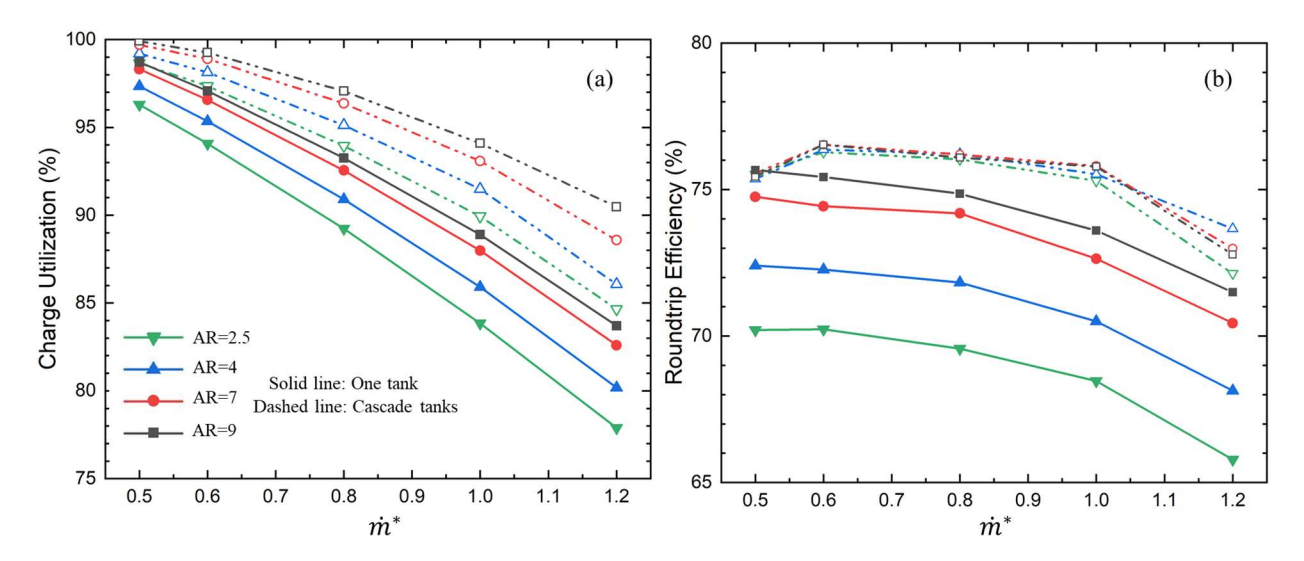


Figure 46 - (a) Charge utilization and (b) roundtrip efficiency comparison between onetank system and cascaded system

The enlarged interface area of cascaded system enhances the charge utilization around 6% compared to one-tank system, as shown in Figure 46 (a). The roundtrip efficiency, however, remains stable as mass flow rate varies, and is less sensitive to shell AR comparing with charge utilization. This observation indicates that although more energy is charged into the system with larger AR, difference in energy content recovered

from discharging is too small to reflect advantageous charging performance, as seen in Figure 45 (b). This observation may indicate a possible ceiling of the cycle performance associated with the specific system configuration in the current study, where additional increase in shell side heat transfer coefficient does not provide prominent enhancement to the thermal performance.

This section has demonstrated enhancement in energetic efficiencies (charge utilization and roundtrip efficiency) led by cascaded system with two shell passes. However, it is important to realize the downside of such alternation in system configuration, which is the elevated compressor work associated with increase in HTF flow velocity.

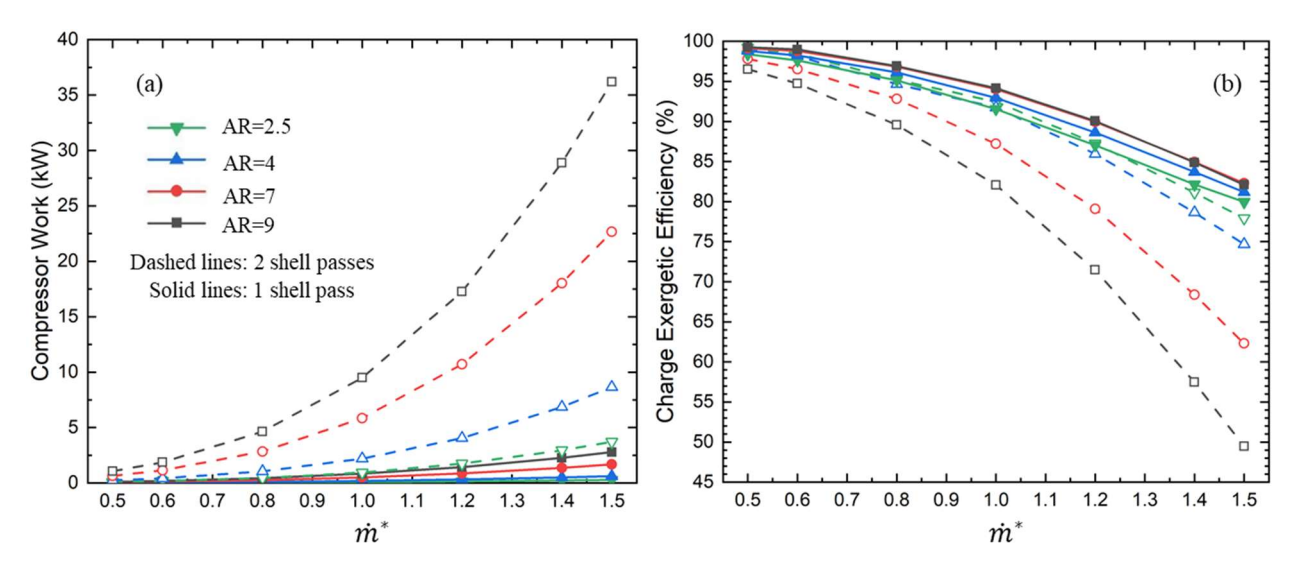


Figure 47 - Comparison of (a) compressor work (b) charge exergetic efficiency between systems with single and two shell passes

The compressor work required to flow the HTF across the system with single and two shell passes are shown in Figure 47 (a). The compressor work is determined as the specific work of isentropic compression, expressed as [61]:

$$W_{1-2} = \Delta h = \int_{1}^{2} v dP$$

$$= \int_{1}^{2} v_{1} \left(\frac{P_{1}}{P}\right)^{\frac{1}{\gamma}} dP = \frac{v_{1} P_{1} \gamma}{\gamma - 1} \left[\left(\frac{P_{1} + \Delta P}{P_{1}}\right)^{\frac{\gamma - 1}{\gamma}} - 1 \right]$$
(2)

where P_1 is the pressure at the system inlet, ΔP denote to the pressure drop across the system. For ideal gas (air), $\gamma = const = \frac{c_p}{c_v} = 1.4$. Based on the expression of pressure-drop across an ideal tube bank, $\Delta P \propto N\rho V^2$ where N is the number of tube rows crossed and V is the flow velocity. With one additional shell pass, both flow velocity and the number of tube rows crossed doubled. Consequently, the pressure-drop becomes 8 times higher, consuming around 10 times more compressor work for the operation. The effect of increased compressor work brings significant exergy destruction that overcomes the benefit brought by enhanced heat transfer performance where charge exergetic efficiency is positively related to increasing shell AR with original systems while the opposite becomes true with two-pass systems, demonstrated by Figure 47 (b).

Design space variation by enhanced performance

With above-discussed variation in system configuration, cascaded tanks with two shell passes, the design space is regenerated according to enhanced performance for requirements listed in Table 6, and compared with original design space, shown in Figure 48.

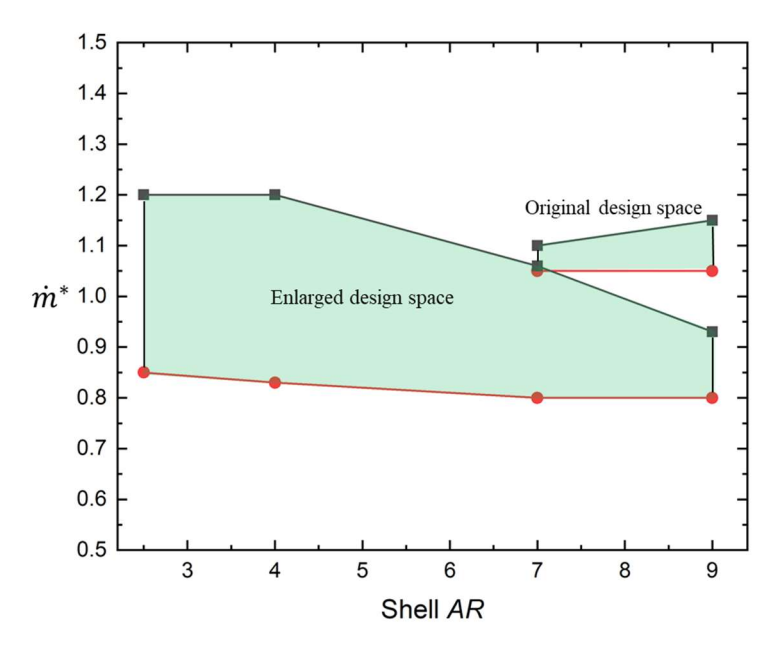


Figure 48 – Comparison of updated design space with the original one based on enhanced performance for systems with large tubes (d_o =0.168 m)

It is clearly seen that the design space is greatly enlarged in range of suitable shell AR and mass flow rate. Due to temperature limit of cold tank, the upper limit of \dot{m}^* is restricted at 1.2 for shell AR=2.5 and 4. It slowly decreases as shell AR increases further, due to drastically decreasing exergetic efficiency. Furthermore, comparing the enhanced

performance with performance requirements used here, especially in charge utilization and roundtrip efficiency, a large margin exists. Therefore, a new set of performance requirements, listed in Table 9, with higher charge utilization and roundtrip efficiency is proposed here to further demonstrate promising potentials of SulfurTES system with enhanced performance.

Table 9: Updated performance requirements

$U_{\it Capacity}$	U_c	$\phi_{\it C}$	$U_{roundtrip}$	ϕ_D
>= 75%	>= 90%	>= 85 %	>= 75%	>= 50% in 8 h

The design space suitable for the updated performance requirements is shown below.

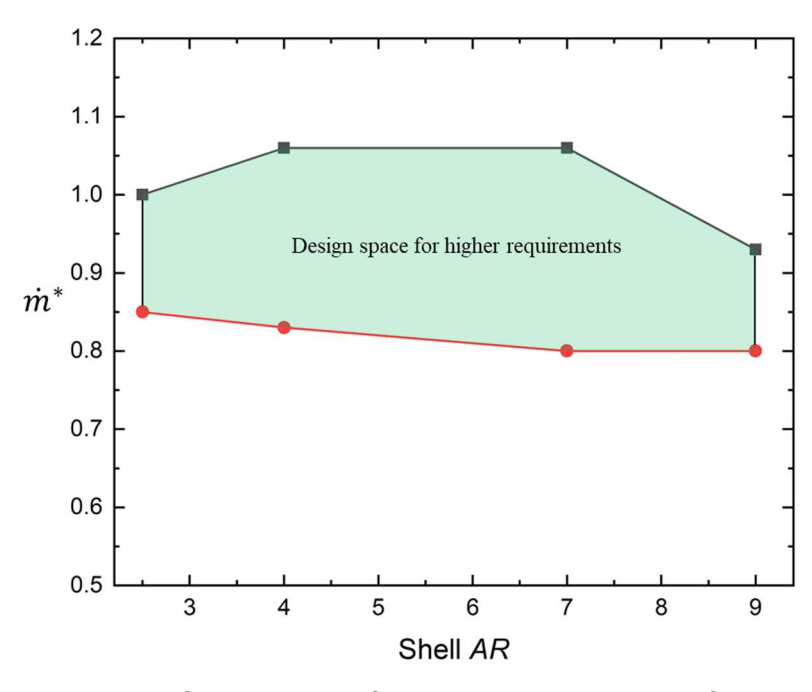


Figure 49 - Design space of updated performance requirements for systems with large tubes (d_o =0.168 m)

Due to highly elevated requirement on charge utilization and roundtrip efficiency, range of mass flow rate narrows down as shell AR decreases from 4 to 2.5, and the largest suitable \dot{m}^* decreases to around 1.05 as opposed to 1.2 in previous design space. But this design space still spans from shell AR from 2.5 to 9 with meaningful range in mass flow rate for selection (from around 0.8 to 1.05 at shell AR = 7). Therefore, the study in performance enhancement is successful where design space is enlarged for previous performance requirements, and reasonable design space can be found with higher demand in charge utilization and roundtrip efficiency.

5.2. System level performance with different HTFs

As discussed in previous studies, the system level performance of single-tank SulfurTES system depends heavily on shell side heat transfer performance, where heat transfer coefficient serves as a dominant factor and is determined by properties of heat transfer fluid. This section presents the performances of systems thermal cycled with sCO₂ and Solar salt within appropriate temperature ranges unique to the HTF (50 - 600°C for sCO₂ and 300 – 550 °C for Solar salt). Performance of systems with air were used as baseline cases for comparison. The study revealed special performance characteristics associated with different HTF properties (gases and liquid HTF), and their advantages/disadvantages.

Comparison between air and sCO₂

Power generation by Brayton cycle with sCO₂ as working fluid has been studied analytically with potential of providing high conversion efficiency, due to high turbine inlet temperature, compact plant size with low cost, due to high fluid density, and reducing CO₂ emission [63,64,65]. Wright et al. [62] designed and constructed a small-scale power plant with sCO₂ Brayton cycle. The main challenge of such cycle is to keep a stable operation of the sCO₂ compression as the fluid properties largely varied in a non-linear fashion. By using the turbo-alternator-compressor unit and the technologies used in its design, they successfully resolved the issue, and have being operating the cycle for over a year with stable power generation.

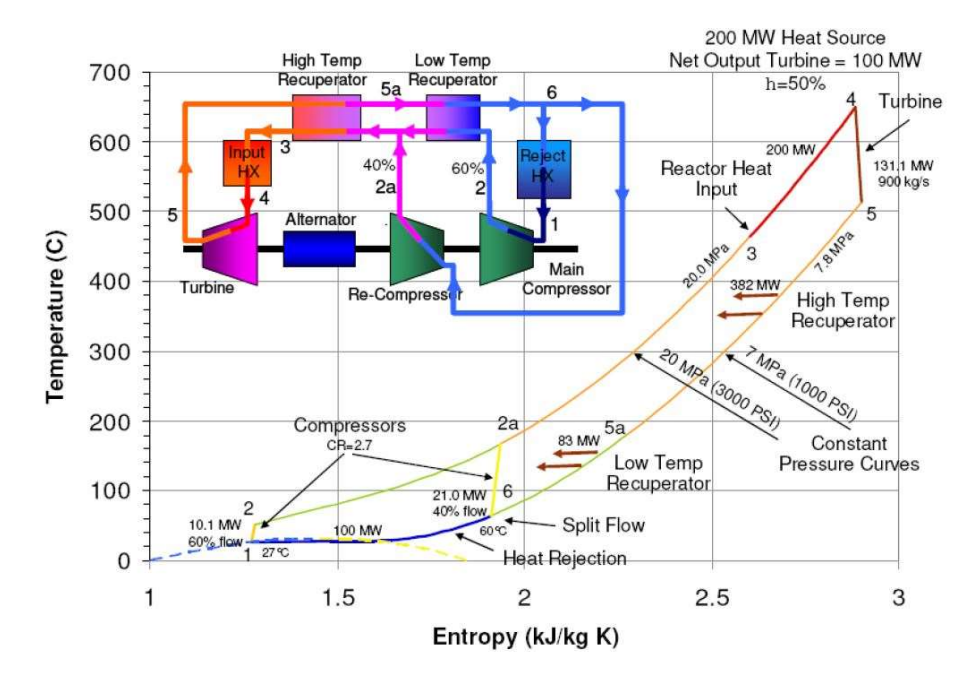


Figure 50 - Temperature-entropy diagram of sCO₂ Brayton cycle [63]

An sCO₂ recompression cycle is shown in Figure 50 [63]. The sCO₂ near critical point is compressed from 7.8 MPa to 20 MPa, heated to around 650 °C by the heating unit, composed by a low temperature recuperator, a high temperature recuperator and a final heat input heat exchanger, then supplied to the turbine, expanding back to 7.8 MPa, and exhausted out at around 500 °C. The turbine exhaust is supplied to recuperators to recycle the waste heat and to cool down to allowable operating temperature for compressors, at around 40 °C. Due to large specific heat mismatch between high-temperature, lowpressure exhaust sCO₂ and low-temperature sCO₂ that is near the critical point, the pinchpoint problem occurs in the recuperator, where heat exchanging effectiveness is extremely low [67]. To solve this issue, the above shown recompression cycle is designed with split flow at stage 6 where partial flow is pre-cooled further before entering the main compressor while the rest of the flow is directly re-compressed. The pre-cooled flow is compressed by the main compressor and enters the low temperature recuperator, where specific heat mismatch is smaller with further reduction by having smaller mass flow rate of cold flow. The flow, heated by the low-temperature recuperator, is merged with the rest of the flow from the re-compressor and supplied to the high-temperature recuperator. The heat exchanging effectiveness is acceptable here because temperature of cold flow is already high enough to be far away from critical point where specific heat mismatch is small enough. Based on previous studies, the optimum operating pressure of re-compression cycle is 20 MPa where highest energy efficiency is achieved [66].

In a conceptual SulfurTES implemented sCO₂ Brayton cycle power plant, SulfurTES system is assumed to replace the original heating unit where sCO₂ at 50 °C, 20 MPa is provided as HTF for discharging. According to NIST Chemistry Webbook Standard Reference Database [50], temperature dependent thermophysical properties are shown in Figure 51. Their temperature dependencies are obtained by curve fitting and are listed in Table 10.

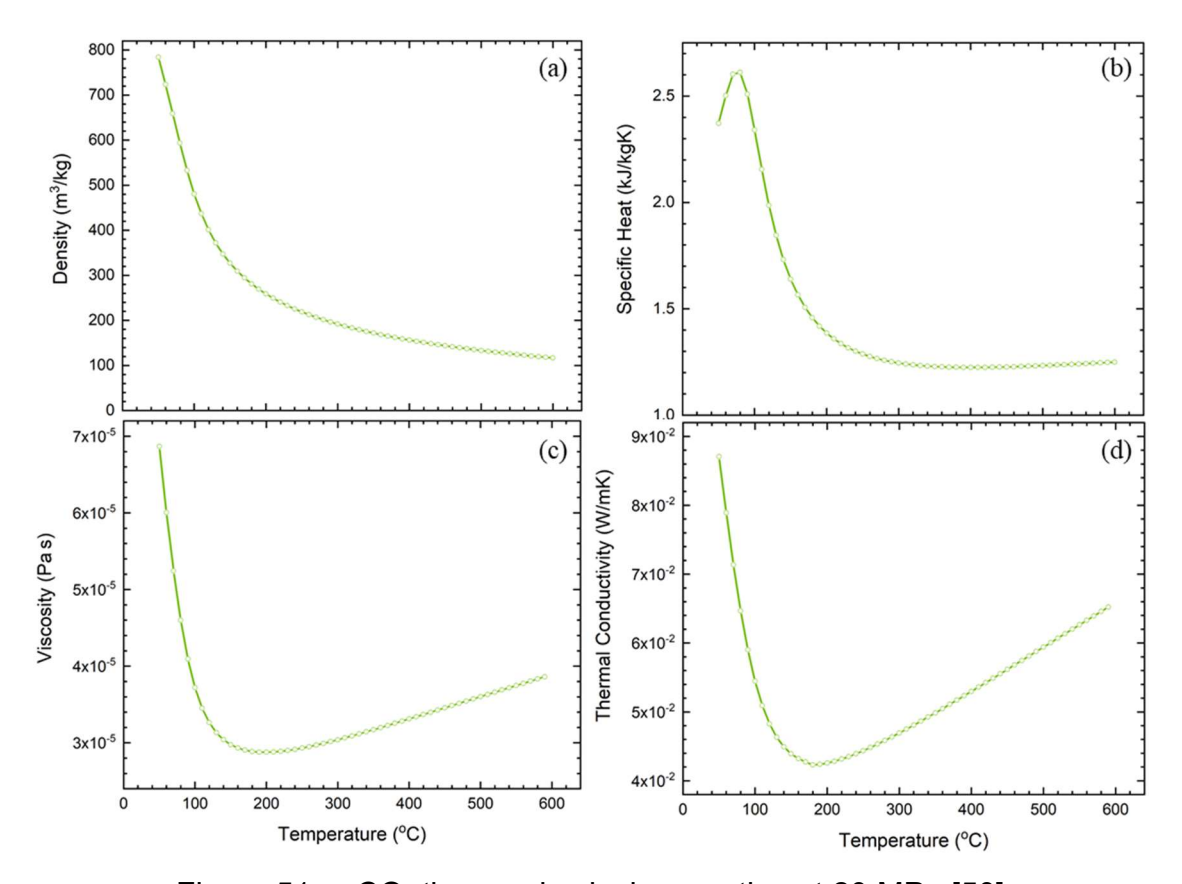


Figure 51 - sCO₂ thermophysical properties at 20 MPa [50]

Large variation in specific heat and density are two prominent features of sCO₂. In Figure 51 (a), the density monotonically decreases from 800 to about 100 m³/kg. The specific heat, shown in Figure 51 (b), peaks around 2.6 kJ/kgK at 100 °C, quickly drops to around 1.3 kJ/kgK at around 200 °C and stays relatively constant. This liquid-like density leads to compact plant size that lowers the cost. Both viscosity and conductivity are gas-like, seen from Figure 51 (c) and (d), similar to those of air.

Table 10: Thermal properties of HTF (sCO₂)

Properties	sCO ₂ (unit of T: °C)
Density, ρ [kg/m³]	$1.92 \times 10^{-13} T^6 - 5.07 \times 10^{-10} T^5 + 5.44 \times 10^{-7} T^4 - 3.05 \times 10^{-4} T^3 + 9.52 \times 10^{-2} T^2 - 16.2 T + 1.4 \times 10^3$
Viscosity, μ [Pa s]	$8.28\times10^{-20}T^{6} - 1.83\times10^{-16}T^{5} + 1.63\times10^{-13}T^{4} - 7.46\times10^{-11}T^{3} + 1.86\times10^{-8}T^{2} - 2.42\times10^{-6}T + 1.49\times10^{-4}$
Specific heat (T < 150 °C), C_p [J/kgK]	$2.51\times10^{-9}T^4 + 2.62\times10^{-6}T^3 - 1.08\times10^{-3}T^2 + 1.11\times10^{-1}T - 0.85$
Specific heat ($T > 150 ^{\circ}\text{C}$), $C_p[J/\text{kgK}]$	$6.42\times 10^{-11}T^4 - 1.13\times 10^{-7}T^3 + 7.38\times 10^{-5}T^2 - 2.12\times 10^{-2}T - 3.48$
Thermal Conductivity, k [W/mK]	$4.72\times10^{-17}T^{6} - 1.12\times10^{-13}T^{5} + 1.08\times10^{-10}T^{4} - 5.44\times10^{-8}T^{3} + 1.51\times10^{-5}T^{2} - 2.16\times10^{-3}T + 0.164$

In the current study, SulfurTES systems used here are one-tank 2-pass systems from last section. Performance of systems are observed and compared with both air and sCO₂. To ensure a fair comparison, the rate of energy supplied or extracted are kept constant where $(\dot{m}C_p)_{air}(T_{hot}-T_{cold})=(\dot{m}C_p)_{sC_{-2}}(T_{hot}-T_{cold})$

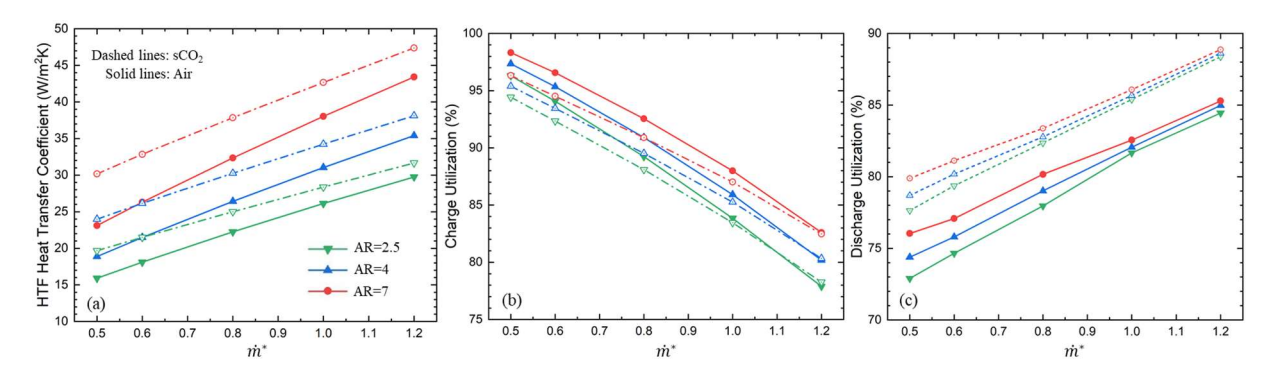


Figure 52 - Comparison of (a) shell side heat transfer coefficient during charging (b) charge utilization (c) discharge utilization with sCO₂ and air as HTFs

Shown in Figure 52 (a), for each system, charge with sCO₂ provides an around 25-10% higher heat transfer coefficient than charge with air as mass flow rate varies from \dot{m}^* = 0.5 to 1. The difference in heat transfer coefficient is mainly contributed by difference in fluid properties. Based on temperature-averaged sCO₂ properties between 50 to 600 °C, a simple analytical calculation shows that: because $Re = \frac{4\dot{m}}{\pi D\mu}$, $\frac{\dot{m}_{SCO_2}}{\dot{m}_{air}} = \frac{c_{Pair}}{c_{PsCO_2}} = 0.88$ and $\frac{\mu_{SCO_2}}{\mu_{air}} = 1.17 = \frac{Re_{SCO_2}}{Re_{air}} = 0.78$. Because $\frac{k_{SCO_2}}{k_{air}} = 1.1$ where $\frac{Pr_{SCO_2}}{Pr_{air}} = 1.62$. Therefore, $\frac{Nu_{SCO_2}}{Nu_{air}} \propto (0.78)^{0.6} \times 1.62^{0.36} = 1.025$ and $\frac{h_{SCO_2}}{h_{air}} = (Nu*k)_{SCO_2}/(Nu*k)_{air} \approx 1.13$.

Charing with small mass flow rate, the average HTF temperature stays low, leading to a higher percentage increase in the heat transfer coefficient, and vis versa for charging with larger mass flow rate.

However, the increase in heat transfer coefficient doesn't prominently boost up the charge utilization, shown in Figure 52 (b). On the contrary, the charge utilization is

around 1.5% lower using sCO₂ than using air. The reason of such behavior is analogous to the pinch-point problem in recuperator where specific heat mismatch lowers the heat exchanging effectiveness. If we focus on a small section near the charge outlet where temperature is less than 200 °C, shown in Figure 53,

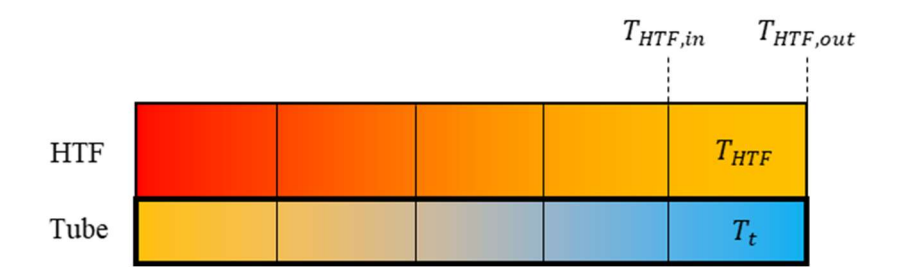


Figure 53 - Schematic of energy transfer between HTF and tube

In a very short period of time, the energy transfer can be seen as steady state where energy conservation of HTF in this small section is expressed as:

$$\dot{m}C_p(T_{HTF,in} - T_{HTF,out}) = hA(T_{HTF} - T_t) \tag{3}$$

With sCO₂ as HTF, at temperature less than 200 °C, C_p quickly increases while ($T_{HTF} - T_t$) stays relatively constant in a short time period, causing a quick drop in $(T_{HTF,in} - T_{HTF,out})$. As time progresses, T_t eventually goes up, faster than that of air, leading to a faster increase in T_t at cold section, reducing the value of right-hand side of the equation that lowers the left-hand side of the equation too. Consequently, the charge utilization becomes smaller due to reduced rate of energy absorption. The difference in charge utilization diminishes as mass flow rate increases, because in this case, T_{HTF}

increases beyond 200 °C faster and staying in temperature zone where C_{p,sCO_2} is relatively constant, closing out the problem. Despite complex physical phenomena discussed above, sCO₂ does not show significant difference in charge utilization over air.

An around 3% enhancement in discharge utilization is obtained using sCO₂ as HTF over air, seen in Figure 52 (c). Because the HTF enters at 50 °C where specific heat is near the peak value. The value of specific heat steeply drops and stays relatively constant as HTF flows along the system with increase in temperature. Therefore, the specific heat problem seen during charging is not applicable in discharging, and the higher heat transfer coefficient with sCO₂ leads to the higher discharge utilization.

The main advantage of using sCO₂ as HTF over air is the negligible exergy destruction by compressor work. The calculation of compressor work is shown by Eq.(2), where $\gamma = -\frac{v}{P}\frac{c_p}{c_v}\left(\frac{\partial P}{\partial v}\right)_T$ instead of a constant for ideal gas. The graphical representation of correlations between specific work and compression ratio is available in the literature where specific work is plotted again compression ratio, r, with different γ [61]:

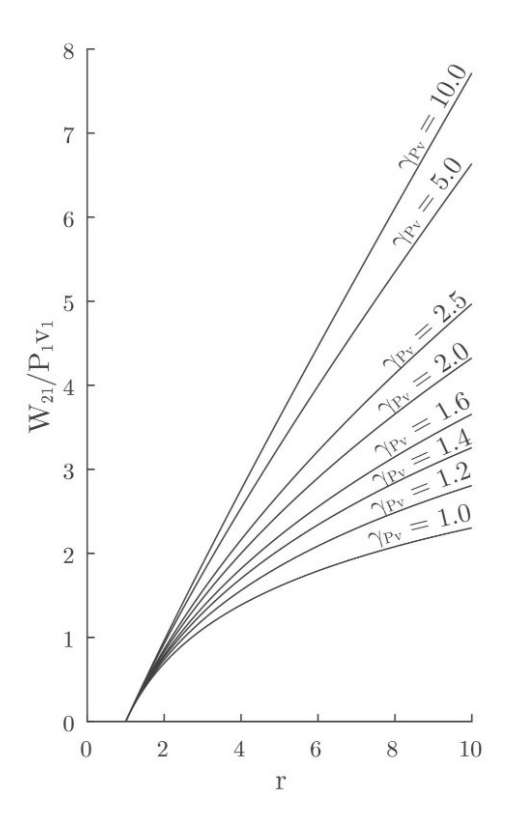


Figure 54 – Specific work of isentropic compression of real gas with corresponding compression ratio [61]

Based on Eq. (8) in section 0, the maximum pressure-drop with air is around 10 kPa. Replacing air with sCO₂, the temperature-averaged density increases to around 450 times higher, where velocity decreases to 1/450 of the original velocity. Since $\Delta P \propto N\rho V^2$, $\Delta P_{SC_2} = \frac{1}{450} \Delta P_{air} \approx 25 \ Pa$. Due to high initial pressure of 20 MPa, the compression ratio is very close to unity. From Figure 54, when compression ratio is approaching 1, the specific work is close to zero. Therefore, with negligible pressure drop, due to low

velocity from high density, and high initial pressure, the exergy destruction by compressor work is neglected using sCO₂ as HTF.

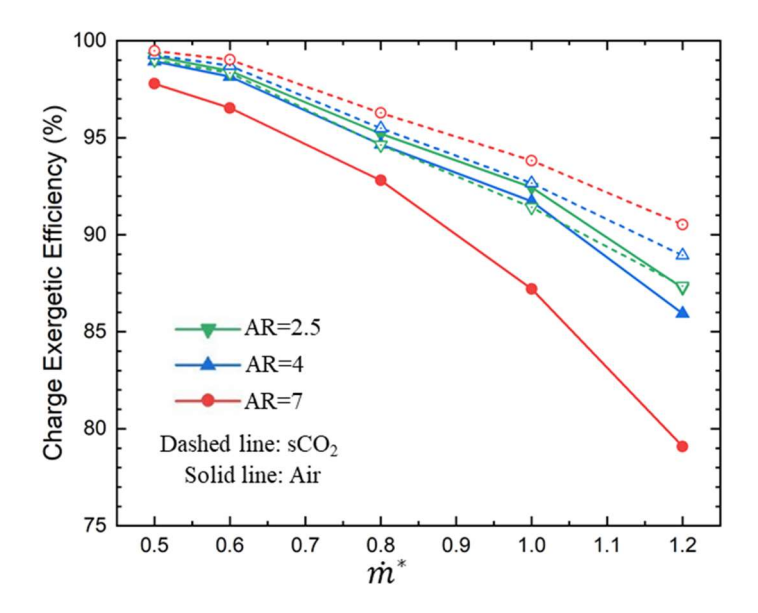


Figure 55 - Comparison of charge exergetic efficiency between air and sCO₂

As observed from Figure 55, without the influence of large exergy destruction, the charge exergetic efficiency with sCO_2 show dependencies on shell geometry and mass flow rate similar to that of charge utilization, whereas completely opposite tendency is seen with air, as mass flow rate and shell AR increase.

Comparison between air and HITEC heat transfer salt

So far, only gases HTFs have been investigated. The performance of liquid HTF, with much higher density and thermal conductivity, is an interesting topic discussed in this section. Molten nitrite salt is widely used as both HTF and storage medium in many high

temperature applications [68,69,70]. Different salts with different chemical compounds are applied for different temperature range within their freezing points and maximum chemically stable temperature. Some examples can be found in section 2.1. in the current study, HITEC heat transfer salt [71] (abbreviate as HITEC salt) is used as HTF. The allowable operating temperature range is 238-593 °C [72]. For practical concerns, the operating temperature range is set to be 290-550 °C to avoid freezing and chemical decomposition [70], and thus used in this study. The thermal properties of HITEC salt is obtained from [71] and listed in.

Table 11: Thermal properties of HTF (HITEC salt [71])

Properties	HITEC salt (unit of T: °C)		
Density, ρ [kg/m ³]	$1938.0 - (0.732 \times (T-200))$		
Viscosity, μ [Pa s]	EXP(-4.343 - (2.0143 * (ln(T) - 5.011)))		
Specific heat, $C_p[J/kgK]$	1561.7		
Thermal Conductivity, k [W/mK]	0.74		

Because of the large energy density of HITEC salt, it can be used as both HTF and storage medium. Thus, the following study shifted the range of mass flow rate to \dot{m}^* =0.8 – 1.4 to observe the system level performance under over charged scenario.

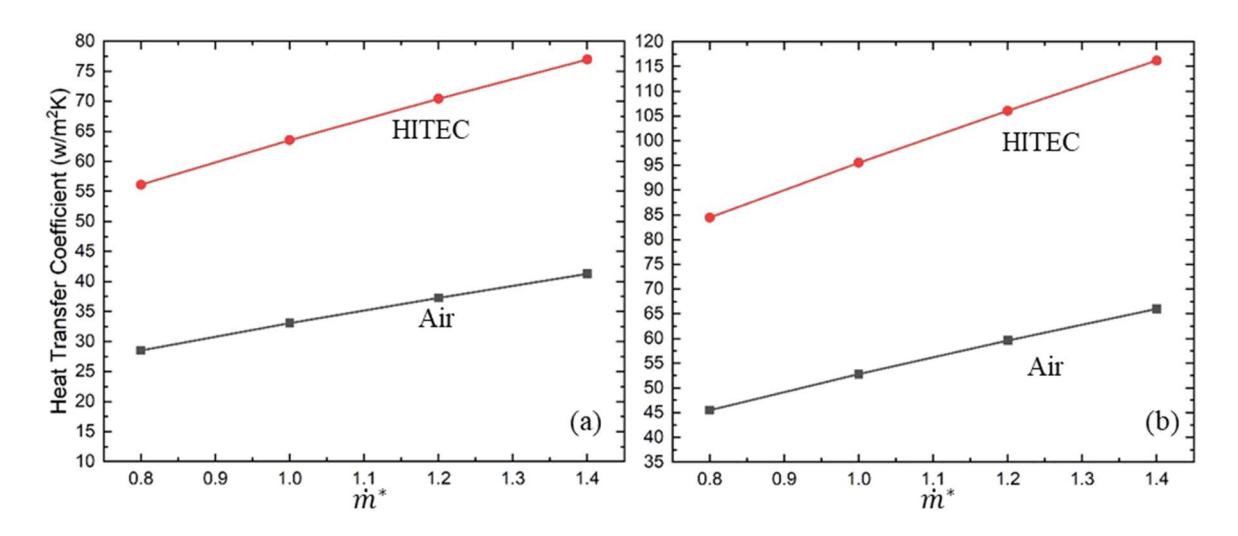


Figure 56 - Comparison of shell side heat transfer coefficient during charging between air and HITEC salt for systems with (a) AR=2.5 (b) AR=7

Figure 56 provides the comparison of shell side heat transfer coefficients using HITEC salt and air as HTFs for system with AR=2.5 and 7. As expected, system with larger AR has higher heat transfer coefficient due to higher flow velocity in slenderer system. Heat transfer coefficient of HITEC salt is about 2 times of that of air, based on difference in thermophysical properties. An analytical calculation, similar to the one presented in previous section for sCO₂ below Figure 52, is done to verify the validity of such observation. Although the much larger viscosity and a higher specific heat of HITEC salt $\frac{\mu_{salt}}{\mu_{air}} = 42.3, \frac{m_{salt}}{m_{air}} = \frac{c_{p_{air}}}{c_{p_{salt}}} = 0.7$) yield a small Nusselt number compared with air $\frac{Nu_{salt}}{Nu_{air}} = 0.157$), the much larger thermal conductivity $\frac{k_{salt}}{k_{air}} = 12.93$) still leads to higher heat

transfer coefficient: $\frac{h_{salt}}{h_{air}} = (Nu * k)_{salt}/(Nu * k)_{air} \approx 2.02$, which is consistent with result shown in Figure 56.

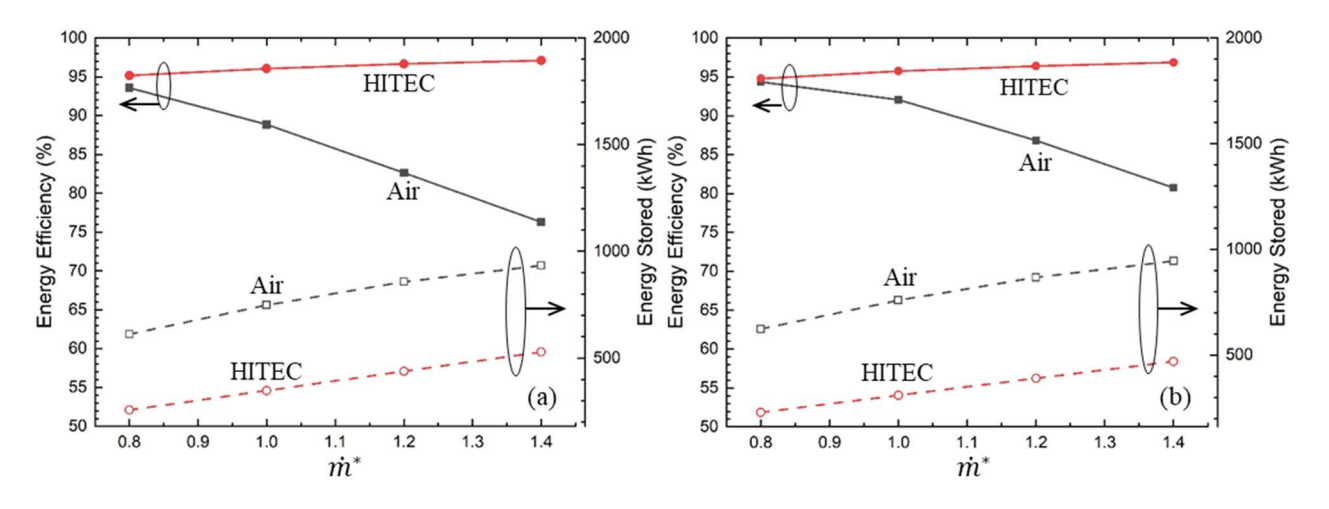


Figure 57 - Comparison of charge utilization and amount of energy stored between air and HITEC salt for systems with (a) AR=2.5 (b) AR=7

The charge utilization with corresponding amount of energy storage using air and HITEC salt as HTFs are demonstrated in Figure 57. It is observed that with HITEC salt, the charge utilization stays relatively constant near 100% for all charge mass flow rates and system configurations, indicating that the energy waste is almost zero except less than 5% of heat loss. However, the amount of energy stored within the sulfur and tube is only around half of that using air as HTF, despite its decreasing charge utilization that is deviating far away from 100% as mass flow rate increases. By examining the axial temperature distribution at the end of charging with both types of HTFs, shown in Figure

58, we observe a clear thermocline within HITEC salt that provides great thermal segregation, yielding a near 100% charge utilization.

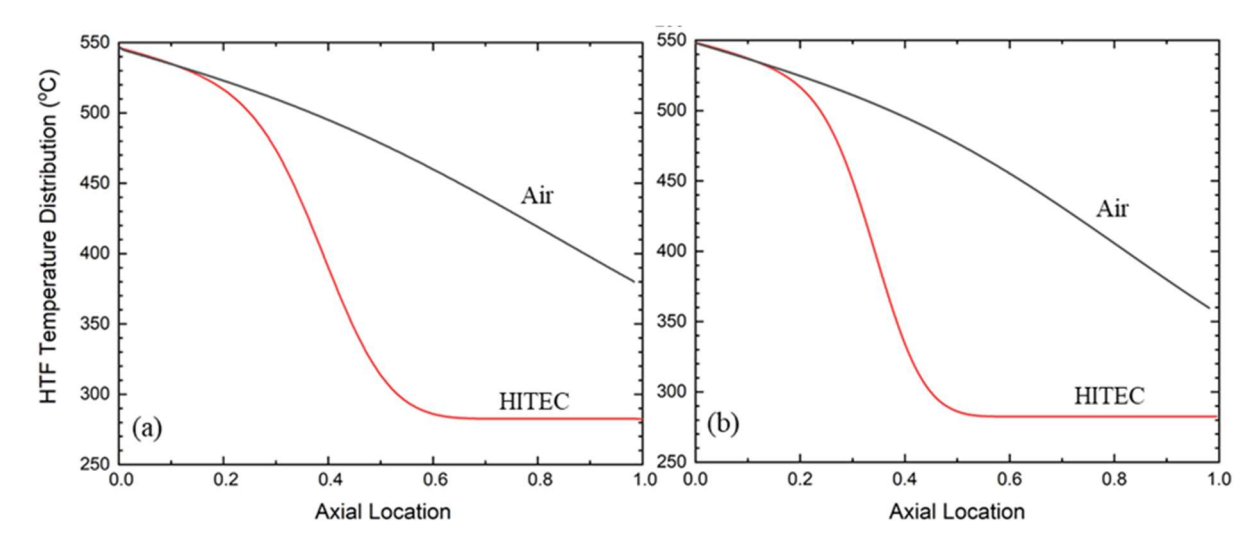


Figure 58 – Comparison of axial temperature distribution within HTFs at the end of charging for systems with (a) AR=2.5 (b) AR=7 between air and HITEC salt

However, due to HITEC salt's significantly higher energy density compared to air $(\frac{c_{p_{salt}}}{c_{p_{air}}} = 1.65, \frac{\rho_{salt}}{\rho_{air}} = 3035)$, the energy withheld within the HTF is also significant, and is calculated as:

$$E_{HTF} = \int_0^L \rho A C_p(T(x) - T_{cold}) dx \tag{3}$$

Figure 59 shows the energy distribution at the end of charging for both system configurations with $\dot{m}^*=1$. With a total of 950 kWh energy input by HITEC salt, the system absorbs around 350 kWh of energy, around 490 kWh of energy stays within the HITEC salt, and the rest of the energy is either lost to the ambient or stored within shell

and insulation. On the other hand, when charged with air, the energy storage within HTF is around 0.3 kWh, too small to be visible from Figure 59.

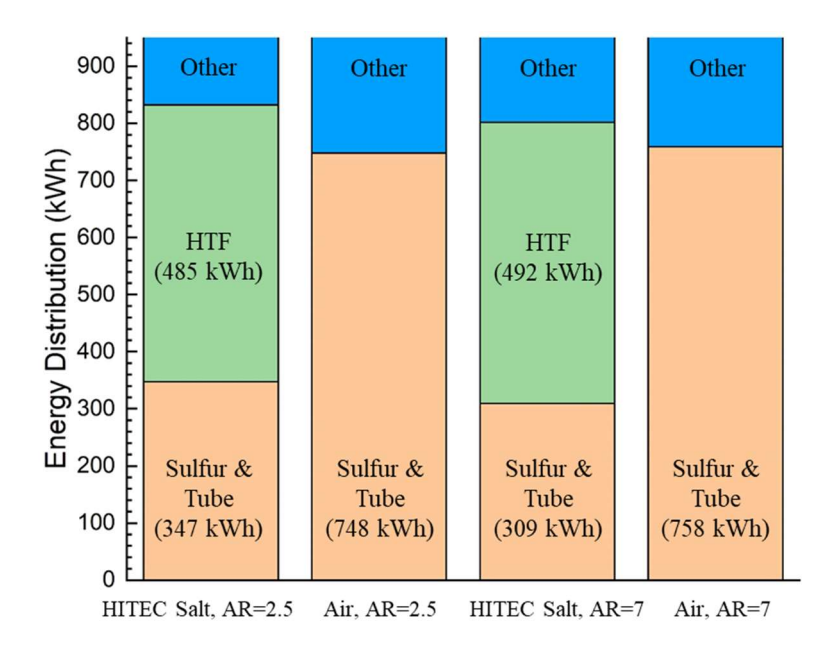


Figure 59 – Comparison of energy distribution within system at the end of charging with $\dot{m}^* = 1$ between air and HITEC salt

The energy storage within sulfur and tube for system with AR=2.5 is 38 kWh more than that of system whose AR=7. This is because the total amount of shell and insulation materials is slightly higher in slenderer system with a higher heat loss due to larger surface area, thus, leads to the difference.

It is observed from this study that the superior heat transfer performance of liquid HTF maintains thermal segregation well that keeps the energy efficiency close to perfect.

The additional storage capacity of HTF could also lead to potential cost reduction with

more compact system. However, the price of liquid HTF itself can be high enough to overcome the cost advantage brought by compact system. The conclusion of whether operating with liquid HTF is a suitable option for SulfurTES systems will be drawn based on the cost comparison with free gases HTF in the next section.

5.3. Cost analysis

The overarching goal of TES technology development is to advise a method that stores thermal energy efficiently with low cost. As shown in Figure 8, numerous research efforts exploited various ways in thermal energy storage, attempting to achieve the cost target. One of the major innovations of SulfurTES system is its low-cost characteristics associated with elemental sulfur. This chapter provides insight into the cost of SulfurTES system based on performance variation observed from previous sections. Both capital cost for installation and levelized cost of energy (LCOE) are estimated and compared with state-of-the-art molten-salt TES system to demonstrate the cost advantage of SulfurTES system.

Capital cost estimation of SulfurTES system

The capital cost denotes to the total amount of expenditure for TES installation. It includes costs of essential components for system construction normalized by the storage capacity. The labor cost for construction and maintenance is not considered in this study.

Two-pass SulfurTES thermal battery in cascaded configuration (abbreviated as single-tank SulfurTES) is studied here. Due to inherent drawback of single-tank SulfurTES in energetic efficiency that is increasingly pernicious to cost as system scale increases, the conceptual two-tank SulfurTES is proposed and evaluated here with potentially further reduction in cost. Two-tank SulfurTES is analogous to molten-salt TES where sulfur is pumped flowing around two tanks for energy transfer. The following cost analysis assumes TES implementation to CSP-trough and CSP-power tower where operating conditions are obtained accordingly. The cost comparison of single-tank/two-tank SulfurTES and molten-salt TES over a wide range of plant capacity is discussed in this section.

To realistically estimate the capital cost, the thermal to electrical energy conversion efficiency is considered to accurately estimate the storage capacity of TES system. The conversion efficiency of power block was measured by ref. [73], where gross electricity output is plotted against turbine inlet temperature with corresponding amount of input thermal energy:

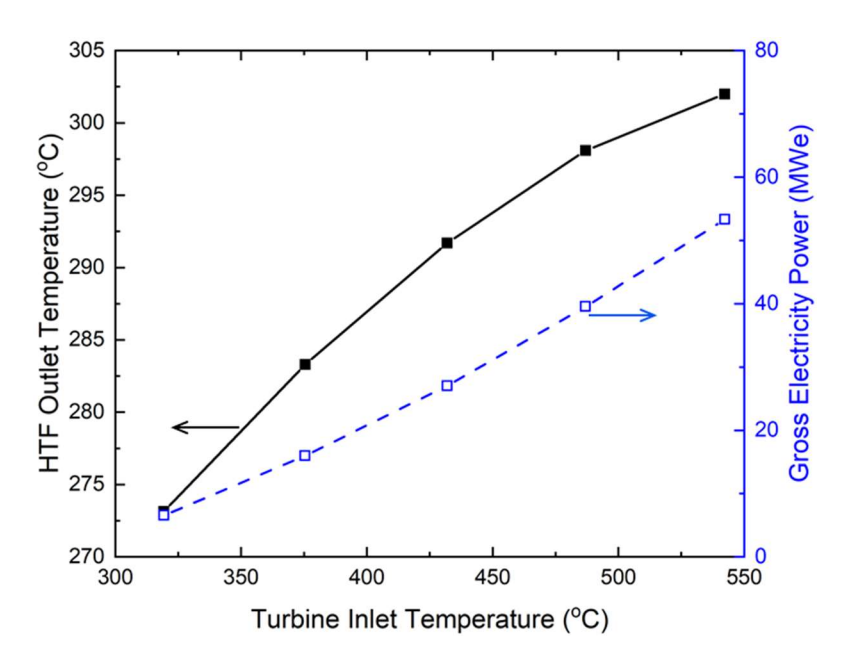


Figure 60 – Gross electricity output from power block with corresponding turbine inlet temperature and amount of input thermal energy [73]

Based on the amount of thermal energy input and electricity generation, the real turbine efficiency is calculated, and compared with Carnot efficiency to obtain the non-ideality of the turbine, shown in Table 12. Since the turbine exhaust temperature is not available in this literature, 102 °C is assumed to be the lowest possible temperature of turbine exhaust [74], and used as temperature of cold reservoir in calculating Carnot efficiency. It is observed that the average ratio between real conversion efficiency and Carnot efficiency is about 75% for turbine inlet temperature from 320 to 550 °C. Therefore, in the current study, the real turbine efficiency is assumed to be 75% of Carnot efficiency.

Table 12: Turbine thermal to electric energy conversion efficiency

Turbine Inlet Temperature (°C)	Salt Outlet Temperature (°C)	Thermal Power Input (MW)	Electricity Output (MW)	Carnot Efficiency (%)	Real Efficiency (%)	Real/Carnot (%)
319.3	273.1	24.9	6.5	37	26	71
375.5	283.3	49.8	16.0	42	32	75
431.9	291.7	75.7	27.0	47	36	76
487.0	298.1	102.0	39.5	51	39	76
542.3	302.0	129.8	53.3	54	41	76

The operating temperature ranges and corresponding conversion efficiencies of studied systems are shown in Table 13. Constant output temperature is assumed with two-tank SulfurTES while single-tank SulfurTES provides sliding output temperature. The conversion efficiency is the average value of efficiencies associated with upper and lower limit of the sliding temperature range. To ensure sufficient energy usage of single-tank SulfurTES while maintaining practicality in turbine operation, the discharge cutoff temperature is set to be 250 °C. To avoid sulfur freezing in two-tank configuration, sulfur temperature is maintained above 200 °C, while in single-tank, TD is assumed to be 150 °C for higher energy density.

Table 13: Operating temperature ranges and conversion efficiencies of SulfurTES systems in single/two-tank configurations for CSP-trough and CSP-power tower

System Con	ifiguration	Turbine Inlet Temperature (°C)	TES Discharge Temperature (°C)	Conversion Efficiency (%)
Trough Plant	Single tank	550-250	150	31
	Two tank	550	200	41
Power Tower	Single tank	650-250	150	33
	Two tank	650	200	45

Cost of Single-tank SulfurTES

To accurately estimate the system cost, it is imperative to determine the appropriate storage capacity that is enough to provide necessary amount of energy required for a 12-hour power block operation without unnecessary overdesign. The thermal energy required for a 12-hour power block operation is calculated as

Thermal energy required
$$(Q_{required}) = \frac{Plant\ Capacity}{\eta_e} \times 12$$
 (5)

where η_e is the thermoelectric conversion efficiency found in

based on turbine inlet temperature. The storage capacity can then be determined as:

$$storage\ capacity(\ Q_{capacity}) = \frac{Q_{required}}{U_{roundtrip} \times \dot{m}^*}$$
 (6)

The incorporation of \dot{m}^* in the Eq.(6) denotes to the assumed ratio of the amount of energy provided to the storage capacity. The amount of energy provided is calculated as $Q_{provide} = \left(\frac{Q_{required}}{U_{roundtrip}}\right)$, and $U_{roundtrip}$ is dependent on system configuration and operating mass flow rate (\dot{m}^*). Therefore, the TES storage capacity is determined by the assumed \dot{m}^* , where storage capacity $Q_{capacity} = \frac{Q_{provide}}{\dot{m}^*}$. Clearly, the larger the \dot{m}^* is, the smaller storage capacity is with lower cost. However, in the current study, \dot{m}^* is restricted to be less or equal to 1 to avoid requiring excessive amount of energy supply from solar field that is higher than the storage capacity. Based on the roundtrip efficiency shown in

Figure 46 (b), it is observed that roundtrip efficiency stays relatively constant as \dot{m}^* varies from 0.5 to 1. Therefore, $\dot{m}^*=1$ is used in the current study to minimize the cost, as additional overdesign in the storage capacity does not provide prominent increase in $U_{roundtrip}$. Hot tank is designed to provide 70% and 50% storage capacity for systems integrated with CSP-Power tower and Trough plant, respectively, due to difference in operating temperature range. 0.168 m SS316 tubes are used for hot tank while 0.06m SS304 tubes are for cold tank. All systems have shell AR=2.5 to avoid excessive consumption in compressor work. Based on performance of Single-tank SulfurTES system with above-mentioned design, operating under $\dot{m}^*=1$, the storage capacity is finally determined. Table 14 shows storage capacities determined for plant capacity of 1MWe, 10 MWe and 100 MWe as examples. The larger operating temperature range of power tower provides higher $U_{roundtrip}$ and thus requiring smaller storage capacity.

Table 14: Storage capacities determined for selected plant capacities

Plant Capacity (MWe)	Thermal Energy Required (MWh)		\dot{m}^*	Storage Capacity (MWh)		Charge Utilization (%)		Discharge Utilization (%)		Roundtrip Efficiency (%)	
	Tower	Trough		Tower	Trough	Tower	Trough	Tower	Trough	Tower	Trough
1	36.4	38.7		49.1	55.0						
10	364	387	1	491	550	91	89	81	78	74	70
100	3640	3870		4910	5500						

The capital cost of single-tank SulfurTES is estimated based on the storage medium (sulfur) cost, tube cost (SS316 and SS304 tubes), shell cost, foundation cost, insulation cost

and fabrication cost, normalized by the amount of thermal energy required for a 12-hour power block operation, expressed as:

$$C_{single\ tank} = \frac{m_t C_t + L_f C_f + m_s C_s + A_{sh} C_{sh} + A_{ins} C_{ins}}{Q_{required}} + C_{foundation}$$
(4)

where L_f is the total length of tube fabrication required. The shell is made of cast iron, sitting on a foundation made by a pile of sand with a concrete reinforce ring wall [75] and wrapped around by calcium silica insulation. Detailed prices for all components are listed in Table 15.

Table 15: Component price of single-tank SulfurTES

	Materials (\$/k	g)	Shell	Fabrication	Insulation	Foundation (\$/kWh) [70]	
Sulfur [4]	SS316 [76]	SS304 [78]		Fabrication cost (\$/ft) [80]	$(\$/m^2)$ [70]		
0.04	4.34	1.5-2	13.2-21.9	1.99	235	1.1	

Capital costs of Single-tank SulfurTES systems integrated with CSP-Power tower and Trough plant whose plant capacity ranges from 0.5 MWe to 100 MWe are presented in Figure 61. The upper and lower system cost limits are derived based on upper and lower cost limits of aluminum alloy and shell costs. Because higher percentage of storage capacity is contributed by cold tank in systems for trough plant, the uncertainty in aluminum price imposes greater effect on system cost, producing a larger gap between upper and lower cost limits.

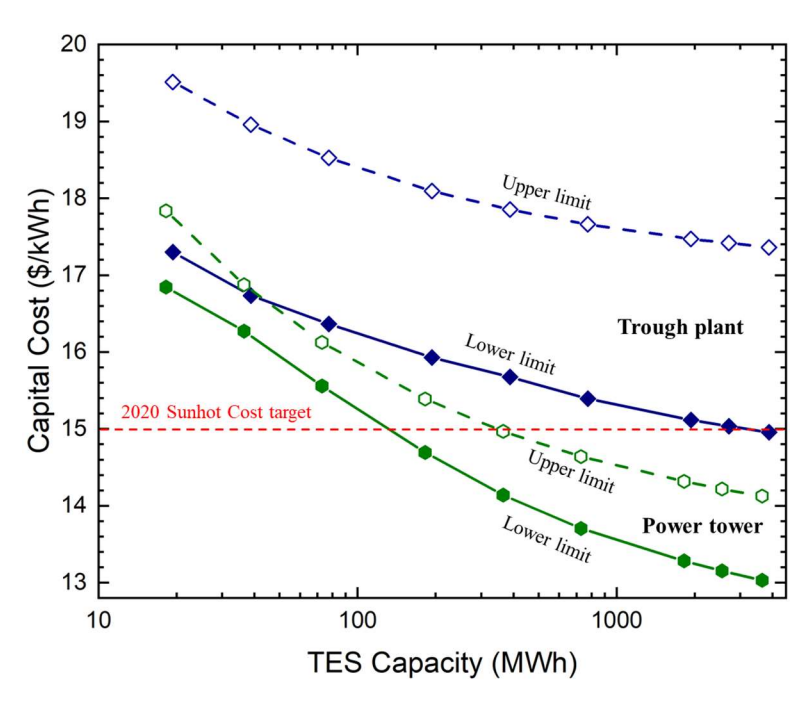


Figure 61 – Capital costs of Single-tank SulfurTES systems integrated with CSP-Power tower and Trough plant

The system cost decreases as storage capacity increases, and ideally, the 2020 Sunshot TES cost target of \$15/kWh for power tower is achieved with storage capacity larger than 180 MWh (5 MWe plant capacity), or 360 MWh storage capacity (10 MWe plant capacity) with greater margin.

As discussed in section 5.2, with HITEC salt as HTF, the large energy density of HTF can be utilized as part of storage capacity, and potentially lowers the system cost. In this case, the \dot{m}^* is set to be 1.4 to observe cost performance of under-designed system.

Table 16: Storage capacity comparison using HITEC salt and air as HTF for trough plant

Plant Capacity (MWe)	Thermal Energy Required (MWh)		\dot{m}^*		Storage Capacity (MWh)		Charge Utilization (%)		Discharge Utilization (%)		Roundtrip Efficiency (%)	
	Salt	Air	Salt	Air	Salt	Air	Salt	Air	Salt	Air	Salt	Air
1	33.7	38.7			32.1	55.0						
10	337	387	1.4	1	321.0	550	96	89	75	78	105	70
100	3370	3870			3210	5500						

Table 16 shows the storage capacities for various plant capacities using HITEC salt as HTF. The required thermal energy is less for systems with salt than that with air. It is because that the operating temperature range of HITEC salt is limited to 290-550 °C, where discharge cutoff temperature is set to be 350 °C, yielding a higher thermoelectric conversion efficiency of 0.36 instead of 0.31. Incorporating energy storage within the HTF, a 105% roundtrip efficiency is achieved, reducing the storage capacity to 95% of thermal energy required. Both factors bring great potential of achieving a lower cost. The capital cost of such system is estimated including the cost of HTF (\$2118.39/m³ [5]). The total amount of HTF required is assumed to be 1.5 times of the amount needed to fill the system.

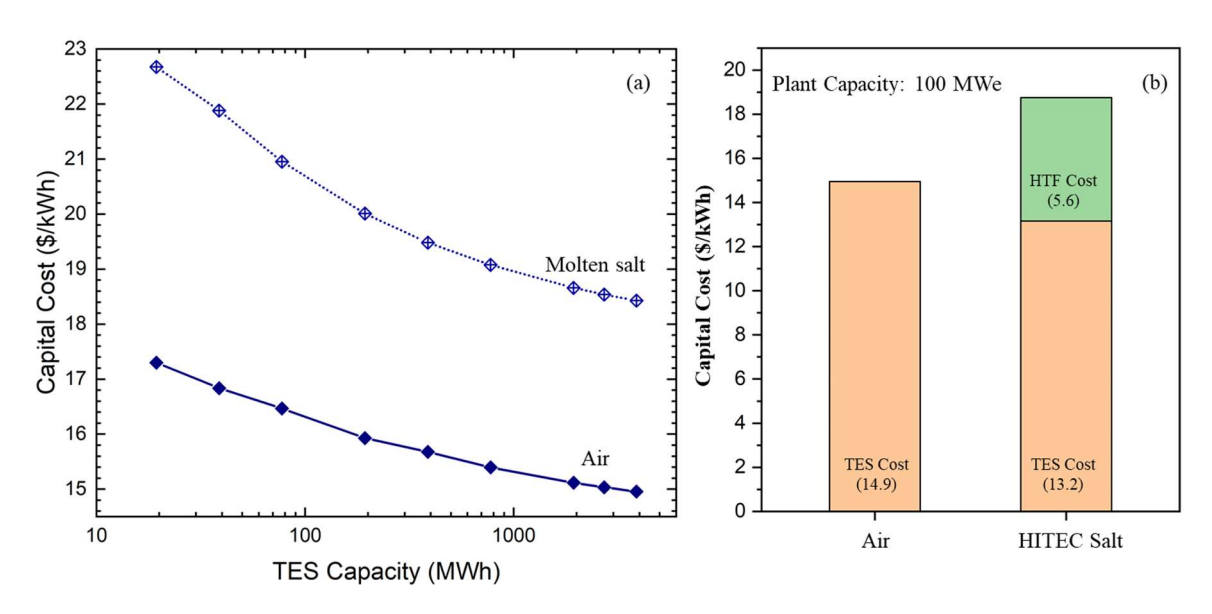


Figure 62 - (a) Capital cost comparison between systems using air and HITEC salt as

HTFs (b) Cost distribution within system and HTF

Figure 62 (a) presents the capital cost variation with plant capacity for systems using air and HITEC salt as HTFs. Opposite to what has been expected, the capital cost of systems using salt as HTF is around \$3.5/kWh higher than those using air. The cost distribution in Figure 62 (b) indicates that, although the storage capacity with salt is around 58% of that with air, the cost only drops to around 88%. This is caused by the small operating temperature range associated with the salt (290-550 °C for salt compared to 150-550 °C for air) that prevents the cost reduction. Besides, the cost of HTF contributes to a considerable portion of the total cost, exceeding the system cost with free HTF. Therefore, for Single-tank SulfurTES system, operating with HITEC salt may not be ideal due to limitations on its operating temperature range and its prohibitive cost.

Cost of Two-tank SulfurTES

An inherent drawback of Single-tank TES system is its impossibility of achieving near perfect roundtrip efficiency due to reduced temperature difference when approaching fully charged/discharged state. Especially during discharging, the left-over energy becomes increasingly harder to recover with deteriorating exergy. Two-tank SulfurTES system is thus proposed to close out this issue. Analogous to the state-of-the-art two-tank molten-salt TES system, Two-tank SulfurTES shares the same configuration but replacing molten-salt with sulfur, shown in Figure 63. The hot tank temperature is at 650/550 °C for power tower and trough plant respectively, and cold tanks are all at 200 °C to prevent freezing.

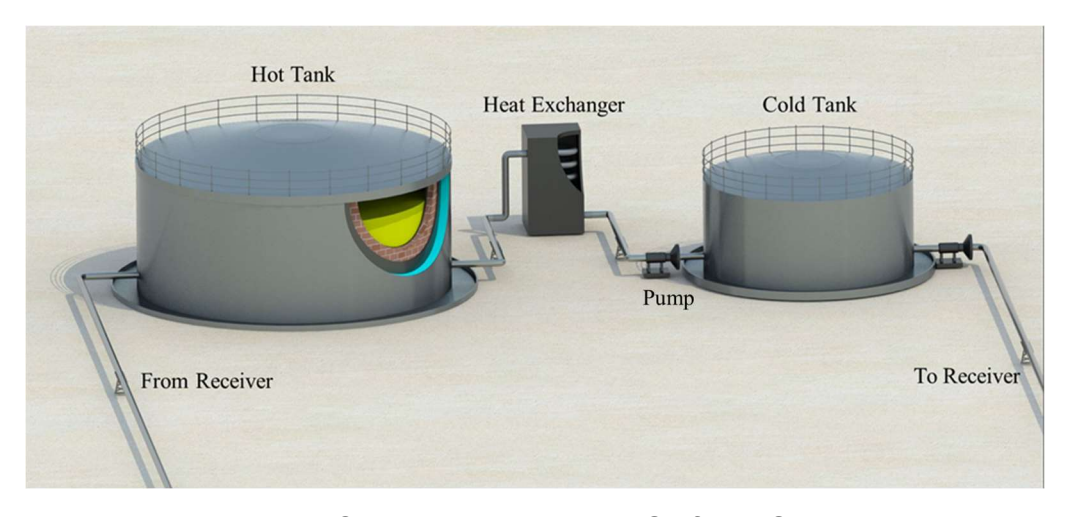


Figure 63 - Conceptual Two-tank SulfurTES system

The tank cost is the most critical component that governs the capital cost in two-tank configuration. The tank of Two-tank SulfurTES is made of SS316, and is designed to

withstand sulfur hydraulic pressure and vapor pressure at elevated temperatures. As shown in Figure 13, the vapor pressure is around 200 psig at 650 °C, 80 psig at 550 °C, and 50 psig at 200 °C. Therefore, the hoop stress is calculated based on Eq. (1), where the pressure term is the summation of vapor pressure and hydraulic pressure ($P = P_v + \rho_s g h_{tank}$). Since the yield stress of SS316 is 200 MPa, the tank thickness is selected so that the hoop stress is less than 150 MPa to add extra margin of safety. Based on the plant capacity, ranging from 0.5-1000 MWe, the size of Two-tank SulfurTES is determined, and is shown in Table 17 for selected plant capacities.

Table 17: Tank geometry of systems with selected plant capacities

Plant Capacity	Power	tower	Trough plant		
(MW)	Tank Diameter (m)	Tank Height (m)	Tank Diameter (m)	Tank Height (m)	
1	6.1	5.9	7.2	7.0	
10	13.2	12.6	15.4	15.3	
100	28.1	27.9	33.2	32.9	
1000	61.0	59.2	71.5	70.9	

The appropriate tank thickness is found and presented in Figure 64 for various plant capacities. Larger hot tank thickness is required for power tower plant, due to higher vapor pressure with higher temperature, while cold tank in trough plant is thicker, due to larger tank diameter imposing higher hoop stress.

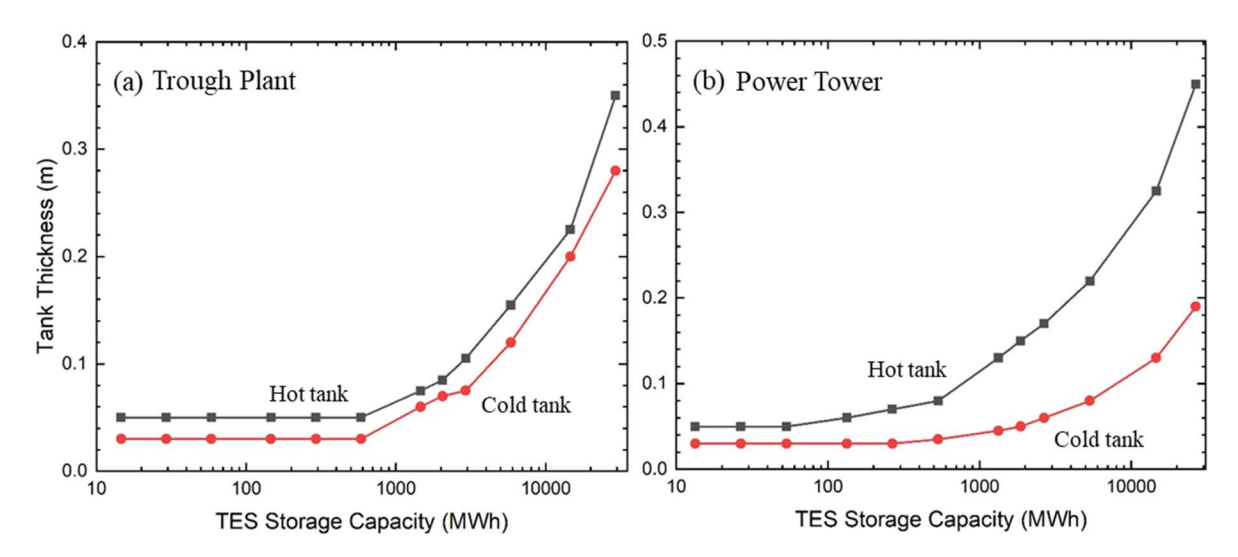


Figure 64 - Tank thickness of Two-tank SulfurTES systems with varying storage capacity

The capital cost of Two-tank SulfurTES is estimated as:

$$C_{two\ tank} = \frac{m_{tank}c_{tank} + m_sc_s + A_{ins}c_{ins}}{Q_{required}} + C_{foundation} + C_{piping} + C_{pumping}$$
 (5)

where detailed price of each component is listed in Table 18.

Table 18: Component price of Two-tank SulfurTES system

Materi	als (\$/kg)	Piping & Valving	Pumping	Insulation	Foundation (\$/kWh) [70]	
Sulfur [4]	SS316 [76]	(\$/kWh) [70]	(\$/kWh) [70]	$(\$/m^2)$ [70]		
0.04	4.34	0.2	0.94	235	1.1	

Based on above listed component price, the capital cost of Two-tank SulfurTES is determined and demonstrated in Figure 65. The capital cost decreases as storage capacity increases and reaches the minimum at 3 GWh and 500 MWh for trough plant and power

tower respectively. The increase in capital cost after the minimum point is caused by the drastically elevated tank thickness, seen in Figure 64, leading to a significant increase in system cost. It is thus proposed to replace the system, larger than the minimum price storage capacity, with multiple smaller systems, at minimum price storage capacity, to keep the cost steady, shown by the dashed line in Figure 65.

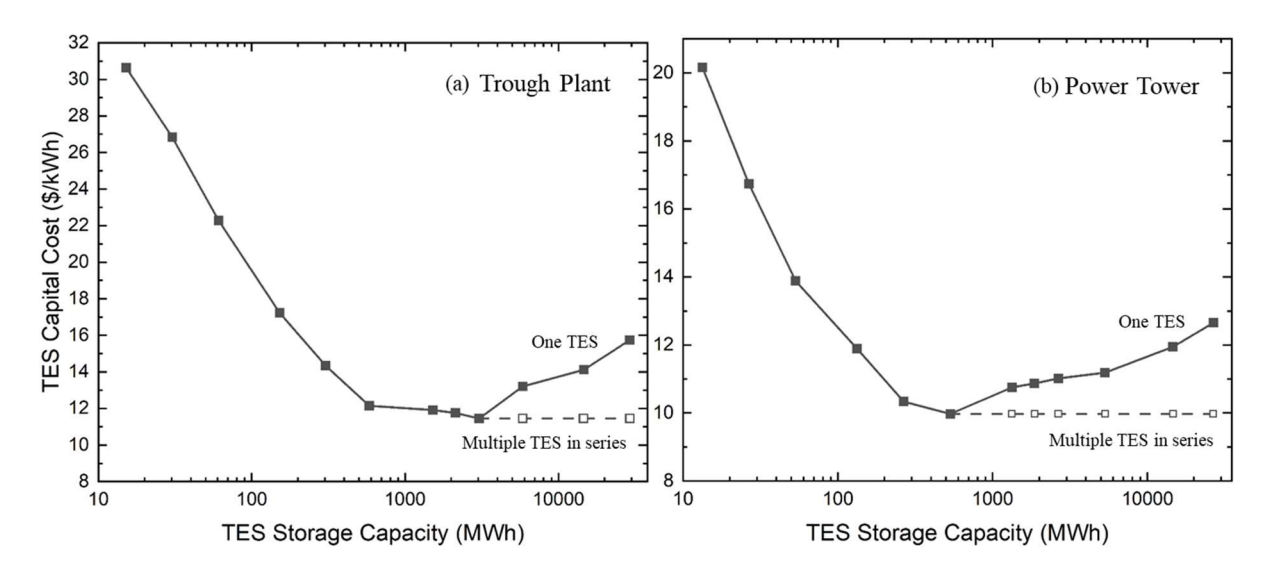


Figure 65 - Capital cost of Two-tank SulfurTES systems with varying storage capacity

capital costs of Single-tank/Two-tank SulfurTES systems along with molten-salt TES systems are compared for plant capacity ranging from 0.5 MWe to 100 MWe.

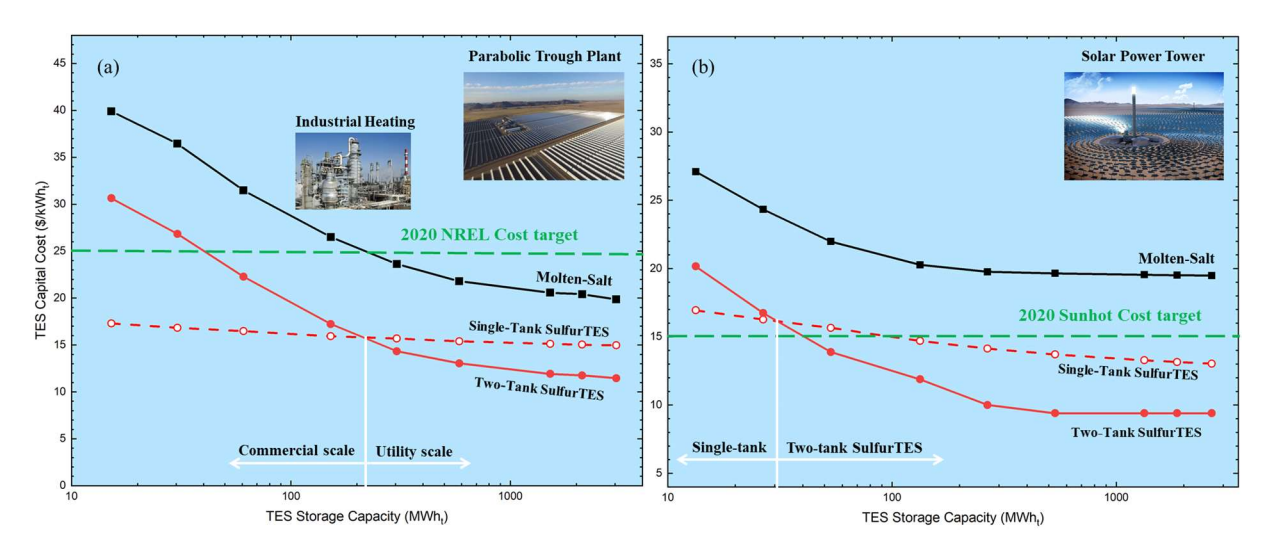


Figure 66 - Capital cost comparison between Single-tank/Two-tank SulfurTES and molten-salt TES systems with (a) parabolic trough plant (250 – 550 °C) (b) solar power tower (250 – 650 °C)

According to results shown in Figure 66, SulfurTES provides significant cost reduction compared to molten-salt TES in the entire range of plant capacity. Single-tank SulfurTES has lower cost in small scale applications, less than 200 MWh and 30 MWh for trough plant and power tower, respectively. Especially for storage capacity lower than 70 MWh with smaller temperature range (250-550 °C), Single-tank SulfurTES show great advantage in cost compared to Two-tank system due to its simple system configuration with less components. The storage cost of single-tank SulfurTES in trough plant within the entire range of storage capacity is way below the cost target by NREL at 2020 [83]. The Sunshot cost target is also easily met by Two-tank SulfurTES with storage capacity larger than 50 MWh and its capital cost keeps on dropping with increasing storage

capacity till reaches the minimum of \$9.4/kWh at 500 MWh (20 MWe plant capacity). It is thus decided to estimate the levelized cost of energy (LCOE) with Two-tank SulfurTES for plant capacity ranging from 20 MWe to 1 GWe.

Levelized cost of energy (LCOE) with Two-tank SulfurTES

The LCOE of CSP-Trough plant and Power tower is estimated with a 12-hour Twotank SulfurTES system using System Advisor Model (SAM) [81]. SAM uses meteorological data based on plant location to provide realistic estimation on energy input to solar field and electricity output from power block. The LCOE can then be determined as

$$LCOE = \frac{Total\ plant\ cost}{Annual\ energy\ generation\ \times Life\ time} \tag{6}$$

The total cost of solar field plus power block is firstly estimated based on the LCOE of plant without TES integration. The solar field of parabolic trough plant costs \$100/m² [82], based on assumed optical efficiency of 0.76. The solar field of power tower costs \$50/m² with \$10/m² site improvement cost [84]. And the price of power block is \$900/kW, according to ref. [84], with an operating and maintenance cost of \$66/kWh [85]. The total plant cost is then estimated as the summation of costs of solar field, power block and SulfurTES. Normalizing total plant cost by annual energy generation

with 12-hour TES and a 30-year lifetime, the LCOE is estimated and presented in Figure 67.

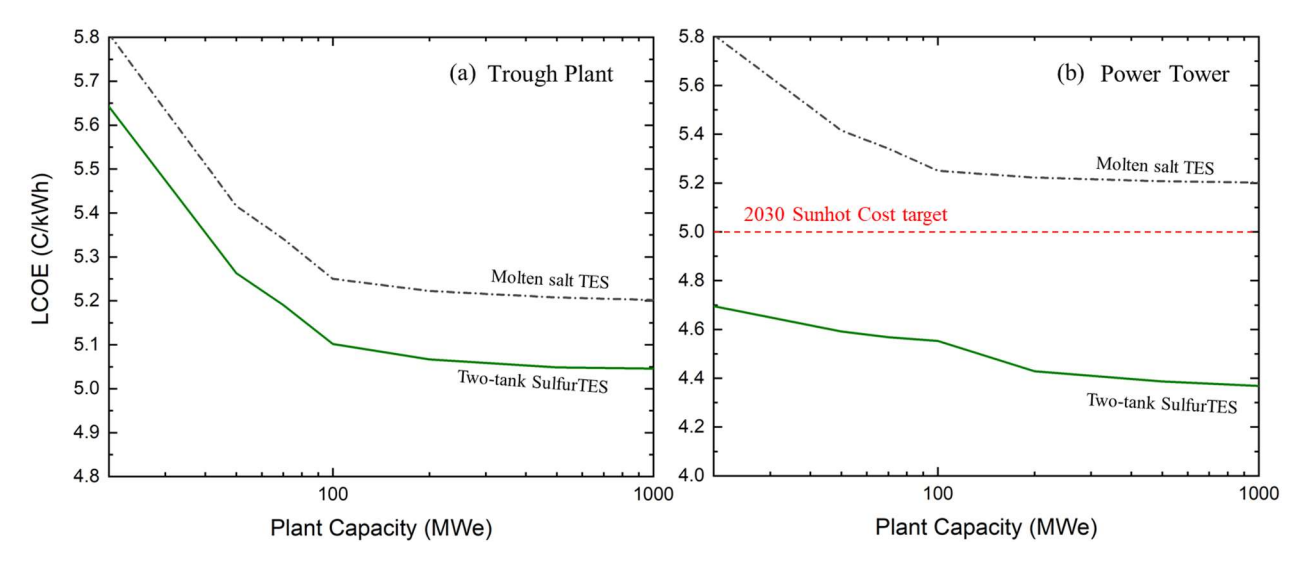


Figure 67 – Comparison of LCOE of (a) Trough plant (b) Power tower with 12-hour Two-tank SulfurTES and Molten-salt TES systems

Thanks to the halved capital cost of Two-tank SulfurTES compared to molten-salt TES, the LCOE in both plants with SulfurTES are much lower than that with molten-salt TES, especially in power plant where an around ¢0.8/kWh reduction is achieved. The 2030 Sunshot cost target of ¢5/kWh is also easily achieved by plant capacity beyond 20 MWe.

5.4. Conclusion

This chapter presents the performance variation and enhancement with varying system configuration and HTF.

- Systems with two shell passes are investigated, providing 50% increase in the shell side heat transfer coefficient that boosted the charge utilization to around 5% higher.
- Additionally, cascaded system with a hot and cold tank, where smaller sized SS304 tubes are used for the cold tank to increase the interface area for heat transfer, is proposed and studied. the increased surface area provides another around 5% increase in charge utilization, making roundtrip efficiency less dependent on shell *AR* and reaching a possible ceiling of about 75%.
- The enhancement in performance enlarged the design space for system with large tubes (d_o =0.168m), and can be further exploited to satisfy higher requirements by providing reasonably large design space for higher charge utilization and roundtrip efficiency.

The effect of HTF on performance of SulfurTES system is also observed here, where sCO₂ and HITEC salt are studied.

• sCO₂ as HTF provides around 10-25% increase in shell side heat transfer coefficient. Due to drastically increasing specific heat in low temperature range near critical point hampering heat transfer effectiveness, the charge utilization is around 1.5% lower than air. But discharge utilization is around 3% high, due

to higher heat transfer coefficient, and most importantly, the compressor work is negligible due to sCO₂'s liquid-like density that brings extremely low velocity with negligible pressure drop.

• The performance of SulfurTES system with HITEC salt as HTF is significantly different than using gases HTF. Due to its much higher conductivity, HITEC salt has about 2 times of shell side heat transfer coefficient of air. Its large energy density can also be used to expand the storage capacity, lowering the needed storage capacity from SulfurTES with potentially reduced system cost. However, the following cost analysis vetoes the use of HITEC salt as HTF, because of the prohibitive cost of salt itself and the limited temperature range that lowers the energy density of SulfurTES system, preventing the cost reduction.

Capital cost estimation of Single-tank SulfurTES in cascaded configuration is conducted assuming integration with CSP-trough plant and power tower with plant capacity ranging from 0.5-100 MWe.

• It is observed that the 2020 Sunshot TES cost target of \$15/kWh for power tower is achieved with storage capacity larger than 180 MWh (5 MWe plant capacity), or 360 MWh storage capacity (10 MWe plant capacity) with greater margin. The

- capital cost of conceptual two-tank SulfurTES is estimated and compared with Single-tank SulfurTES and two-tank molten-salt TES.
- SulfurTES show great cost advantage over molten-salt TES on the entire range of storage capacity. Single-tank SulfurTES has lower cost in smaller scale, less than 200 MWh and 30 MWh for trough plant and power tower, respectively, while Two-tank SulfurTES is more suitable for large scale applications, such as CSP plant.
- The LCOE of CSP-trough plant and power tower with plant capacity ranging from 20-1000 MWe is then estimated integrating with Two-tank SulfurTES. It is confirmed that 2030 Sunshot cost target of ¢5/kWh is easily achieved with SulfurTES system.

Chapter 6 Conclusions and future study

This dissertation shows that sulfur-based thermal energy storage "SulfurTES" provides high-performance and low-cost for industrial scale applications. Most notably, SulfurTES provides significant cost reductions in comparison to molten salts and clearly exceeds DOE targets for TES.

A 2D transient state model was developed and validated to investigate energetic and exergetic performance for Single-tank SulfurTES. Results showed that system's energetic efficiencies (charge/discharge utilization and roundtrip efficiency) were dependent on HTF's thermal performance, where systems with larger shell *AR* (higher shell side heat transfer coefficient) and smaller tube diameter (larger interface area) tend to have higher energetic efficiency. However, they also consumed more compressor work that could potentially lower the exergetic efficiency. This model and the accompanying results, establish important groundwork for further investigation on SulfurTES system level performance.

Systems in cascaded thermal battery configuration with two shell passes was proposed and evaluated. The design enhanced shell side thermal performance for systems with large-sized tubes that boosted energetic efficiencies, expanding the design

space with larger selection range in shell AR and mass flow rate to accommodate more applications.

The use of various HTFs was examined as well including sCO2 and HITEC salt. As expected, HTF properties affected shell side thermal performance. The most prominent advantage of sCO2 is its negligible compressor work, where sCO2's liquid-like density tremendously reduces the pressure drop. With similar thermal performance compared to air, sCO2 is confirmed to be a good HTF for SulfurTES integrated Brayton cycle. The large energy density of HITEC Salt provided additional storage capacity to the system, which could potentially lower the system cost. However, high-temperature salts have prohibitive cost and limited temperature range, which lowers the energy density of SulfurTES, leading to a higher system cost compared with free air.

Finally, the cost analysis assuming SulfurTES integration with CSP plant confirmed the great cost advantage of SulfurTES over state-of-the-art molten-salt TES, and showed promising potential of achieving Sunshot target in capital cost and LCOE with SulfurTES systems.

Future Work

To further advance the SulfurTES technology, necessary following steps are needed and proposed here. Firstly, due to large scale buoyancy driven natural convective current along the axis of vertical tubes, the temperature field along the tube will be different if

charged from the top or from the bottom. Therefore, the performance of systems with vertical tubes or cascaded systems with both horizontal and vertical tubes can be interesting to discover. Secondly, because sulfur is isochorically contained by tubes in all current Single-tank SulfurTES systems, the bath configuration, where HTF passes through sulfur surrounded tubes, has not been fully investigated yet. Without extensive use of tubes, except few as HTF pathway, SulfurTES in bath configuration provides great potential of additional cost reduction. Therefore, the system level performance of SulfurTES in bath configuration is also intriguing for discovery.

Appendix A: Conductive heat transfer coefficient of sulfur conduction

The conduction equation in cylindrical coordinate is:

$$\frac{1}{r}\frac{\partial}{\partial r}\left(r\frac{\partial T(r,t)}{\partial r}\right) = \frac{1}{\alpha}\frac{\partial T(r,t)}{\partial t} \tag{1A}$$

With initial condition $T = T_{s,i}$ and boundary condition $T(r = R) = T_t$ and $\frac{\partial T}{\partial r}(r = 0) = 0$, the analytical solution of 1A is

$$T(r,t) = T_t - \frac{2(T_t - T_{s,i})}{R} \sum_{n=1}^{\infty} \frac{J_o(\lambda_n r)}{\lambda_n J_1(\lambda_n R)} \exp\left(-\alpha \lambda_n^2 t\right)$$
 (2A)

Based on Eq. 2A, the area averaged sulfur temperature $T_s(t)$ can be calculated for different T_t , varying from 30 °C to 60 °C, shown in Fig.1A.

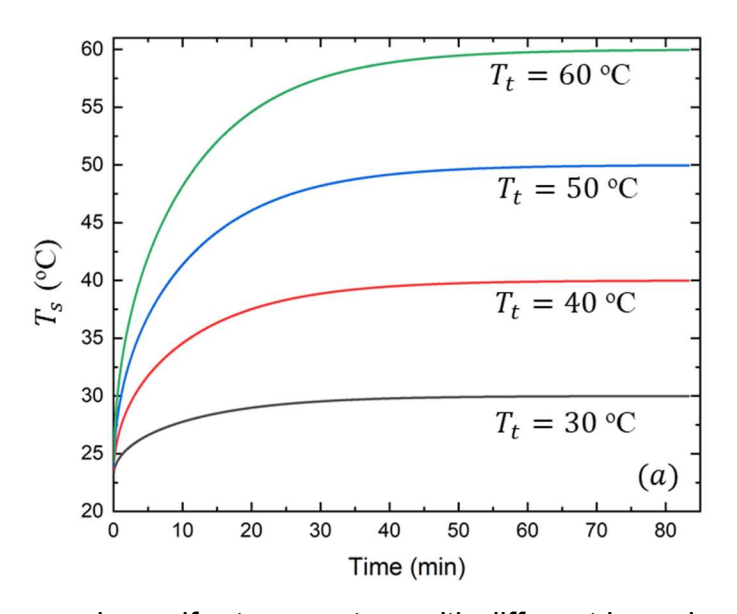


Figure 1A –time varying sulfur temperature with different boundary temperature

The heat rate $\dot{q} = -k \left(\frac{\partial T(r,t)}{\partial r} \right)|_{r=R}$ can be expressed as:

$$\dot{q} = \frac{2k(T_t - T_{s,i})}{R} \sum_{n=1}^{\infty} \frac{\lambda_n J_o(\lambda_n R)}{\lambda_n J_1(\lambda_n R)} \exp(-\alpha \lambda_n^2 t) = \frac{2k(T_t - T_{s,i})}{R} \sum_{n=1}^{\infty} \exp(-\alpha \lambda_n^2 t)$$
(3A)

The area-averaged sulfur temperature T_s is obtained as:

$$T_{S} = \frac{1}{\pi R^{2}} \int_{0}^{2\pi} \int_{0}^{R} T(r, t) r dr d\theta$$

$$= \frac{1}{\pi R^{2}} \int_{0}^{2\pi} \int_{0}^{R} (T_{t} - \frac{2(T_{t} - T_{s, i})}{R} \sum_{n=1}^{\infty} \frac{J_{o}(\lambda_{n} r)}{\lambda_{n} J_{1}(\lambda_{n} R)} \exp(-\alpha \lambda_{n}^{2} t)) r dr d\theta$$

$$= T_{t} - 2(T_{t} - T_{s, i}) \sum_{n=1}^{\infty} \frac{1}{\lambda_{n}^{2}} \exp(-\alpha \lambda_{n}^{2} t)$$
(4A)

Based on Eq. 3A and 4A, the expression for conductive heat transfer coefficient h_{cond} and Nusselt number becomes:

$$h_{cond} = \frac{Nuk}{2R} = \frac{-k\left(\frac{\partial T(r,t)}{\partial r}\right)}{T_t - T_s(t)} = \frac{\frac{2k\left(T_t - T_{s,i}\right)}{R}\sum_{n=1}^{\infty}\sum_{n=1}^{\infty}\exp\left(-\alpha\lambda_n^2t\right)}{\frac{1}{2\left(T_t - T_{s,i}\right)}\sum_{n=1}^{\infty}\frac{1}{\lambda_n^2}\exp\left(-\alpha\lambda_n^2t\right)} = \frac{k\sum_{n=1}^{\infty}\exp\left(-\alpha\lambda_n^2t\right)}{R\sum_{n=1}^{\infty}\frac{1}{\lambda_n^2}\exp\left(-\alpha\lambda_n^2t\right)}$$
(5A)

$$Nu = \frac{2(T_t - T_{s,i}) \sum_{n=1}^{\infty} \exp(-\alpha \lambda_n^2 t)}{(T_t - T_{s,i}) \sum_{n=1}^{\infty} \frac{1}{\lambda_n^2} \exp(-\alpha \lambda_n^2 t)} = \frac{2 \sum_{n=1}^{\infty} \exp(-\alpha \lambda_n^2 t)}{\sum_{n=1}^{\infty} \frac{1}{\lambda_n^2} \exp(-\alpha \lambda_n^2 t)}$$
(6A)

Eq. 6A demonstrates that the Nusselt number is only a function of time *t*, independent on boundary tube temperature. Shown in Fig.2A (a), the Nusselt number variation with time for all four cases merge into one curve.

Defining a non-dimensional temperature T^* with an expression shown in Eq.7A to combine the instantaneous sulfur temperature with tube temperature. The expression shows that, T^* is only a function of time. Therefore, T^* variation over time for above four cases fall on one curve, presented in Fig.2A (b).

$$T^*(t) = \frac{T_s(t) - T_{s,i}}{T_t - T_{s,i}} = \frac{(T_t - T_{s,i}) - 2(T_t - T_{s,i}) \sum_{n=1}^{\infty} \frac{1}{\lambda_n^2} \exp(-\alpha \lambda_n^2 t)}{(T_t - T_{s,i})} = 1 - 2 \sum_{n=1}^{\infty} \frac{1}{\lambda_n^2} \exp(-\alpha \lambda_n^2 t)$$
(7A)

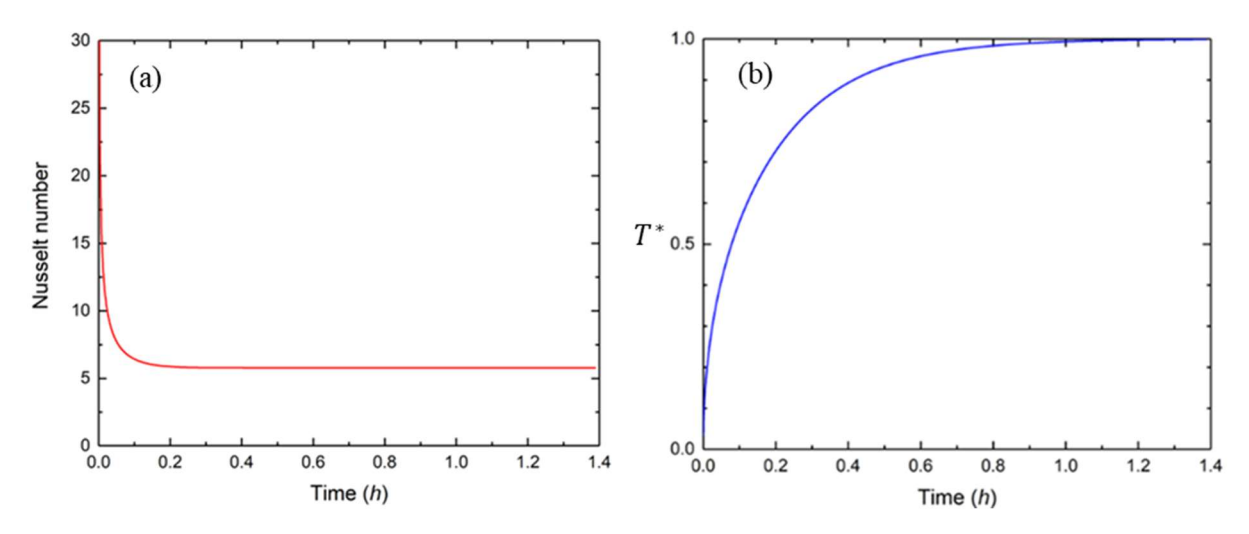


Figure 2A – (a) Nusselt number (b) T^* variation as a function of time

Correlating $T^*(t)$ and Nu(t) produces the relationship between instantaneous sulfur and tube temperatures with instantaneous Nusselt number, shown in Fig.3A.

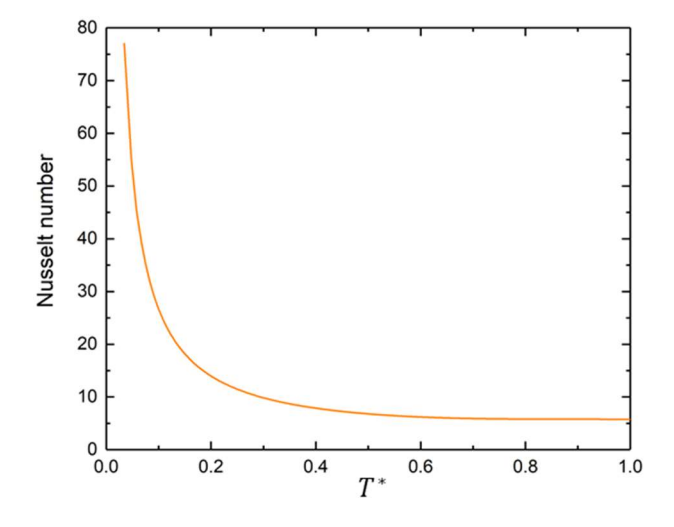


Figure 3A – Nusselt number as a function of T^*

The relationship between Nu and T*is obtained by curve fitting.

$$Nu = 3637.59T^{*6} - 12804.29T^{*5} + 18022.76T^{*4} - 12925.86T^{*3} + 4980.08T^{*2} - 992.17T^{*} + 90.54$$
(8A)

Appendix B: Example usage of system design procedure

Example 1

In the first example, known working condition comes from a representative CSP plant where the solar receiver can charge the system by air at 600 °C and a mass flow rate of 0.164 kg/s with a charge rate of 100 kW for 6 hours. The system will then be discharged by air at 50 °C for 12 hours. Based on this working condition and design space obtained in section 0, the system shall be designed in the following steps to meet performance requirements listed in section 0:

- 1. Set an initial guess of storage capacity of 1.2 MWh that leads to a $\dot{m}_{ref}=0.326$ kg/s
- 2. $\dot{m}^* = \frac{\dot{m}_{act}}{\dot{m}_{ref}} = \frac{0.164}{0.326} = 0.5 < 0.8$ (\dot{m}^* should be between 0.8 and 1.2 according to design space shown in section 0)
- 3. Decrease the storage capacity to another tentative value of 630 kWh with $\dot{m}_{ref} = 0.172$
- 4. $\dot{m}^* = \frac{\dot{m}_{act}}{\dot{m}_{ref}} = \frac{0.164}{0.172} = 0.95$, falling inside the design space. The storage capacity is set to be 630 kWh, concluding the first iteration loop.

- 5. The second iteration loop starts by setting an initial guess for shell inner diameter of 0.8 m with tube diameter of 0.06 m, then the number of tubes that this shell size can accommodate is 82.
- 6. Based on the storage capacity and number of tubes, the required shell length is 7.46 m with corresponding shell AR=9.3. Since \dot{m}^* = 0.95, the obtained shell AR of 9.3 is outside the design space, the shell diameter should be increased to lower the shell AR into safe range.
- 7. The shell inner diameter is increased to 1 m, which can contain 133 tubes, yielding a shell length of 4.6 m, with shell AR=4.6. Because \dot{m}^* = 0.95 with corresponding shell AR=4.6 falls into the design space, the above performance requirements should be met.

This example design provides one system design that satisfies the performance requirements, but it is not the only solution, other designs should also be valid if \dot{m}^* and corresponding shell AR fall into the design space shown in section 0.

Example 2

In the second example, existing system is provided where a 430-kWh system is built with 100 five-meter long tubes whose diameter is 0.06 m, then the appropriate operating condition can be chosen in the following step:

- 1. The shell inner diameter required to enclose $100\,0.06$ -m tubes is calculated as $0.84\,$ m.
- 2. The shell AR is then obtained as 5.9
- 3. From the design space, when shell AR=5.9, \dot{m}^* should be approximately in the range from 0.8 to 1.15.
- 4. Since the storage capacity is known as 430 kWh, where $\dot{m}_{ref}=0.118$ kg/s , the actual mass flow rate can then be determined to be in the range between 0.094= kg/s and 0.136 kg/s.

Appendix C: Preliminary experimental investigation on performance of lab-scale SulfurTES thermal battery

The preliminary experimental investigation on performance of lab-scale SulfurTES thermal battery is presented in this section. The experimental setup is shown in Fig. 1C.

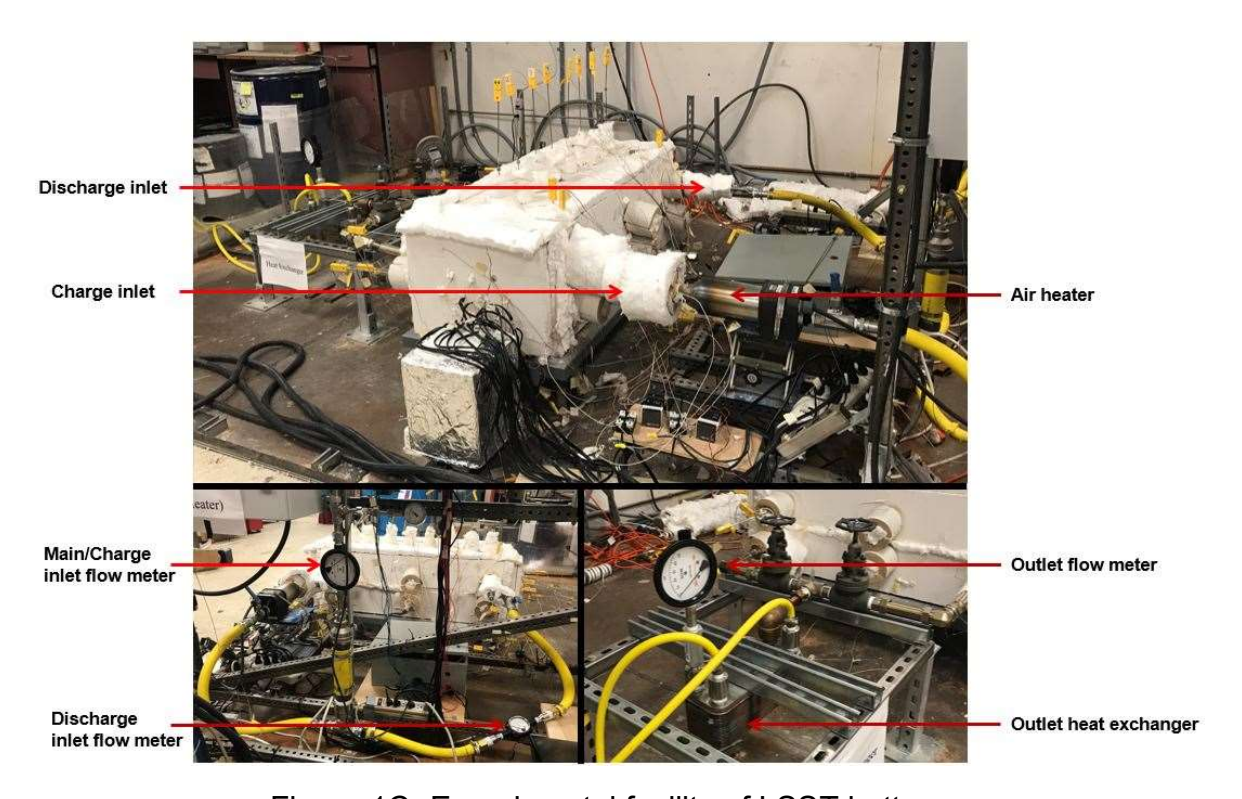


Figure 1C- Experimental facility of LSST battery

At the beginning of thermal charging, a steady HTF flow was established, where the flow rate was measured by the main inlet flow meter. If the flow rate by outlet flow meter was within acceptable range (less than 10% different from inlet flow meter measurement), the air heater was turned on to charge the LSST battery to elevated temperatures (600°C,400°C). The heat exchanger on the outlet of LSST battery cooled down the exhaust air to ensure safe operation. The LSST battery was charged with different mass flow rates (35,30 SCFM) of HTF as different test cases. When the system was charged to around 500°C, the discharging process started by supplying a 60°C HTF at 35,30, and 25 SCFM flow rates. Performance parameters were then calculated based on temperature measurements.

Charge/Discharge rate

The charge/discharge rate attained in all test cases are shown below:

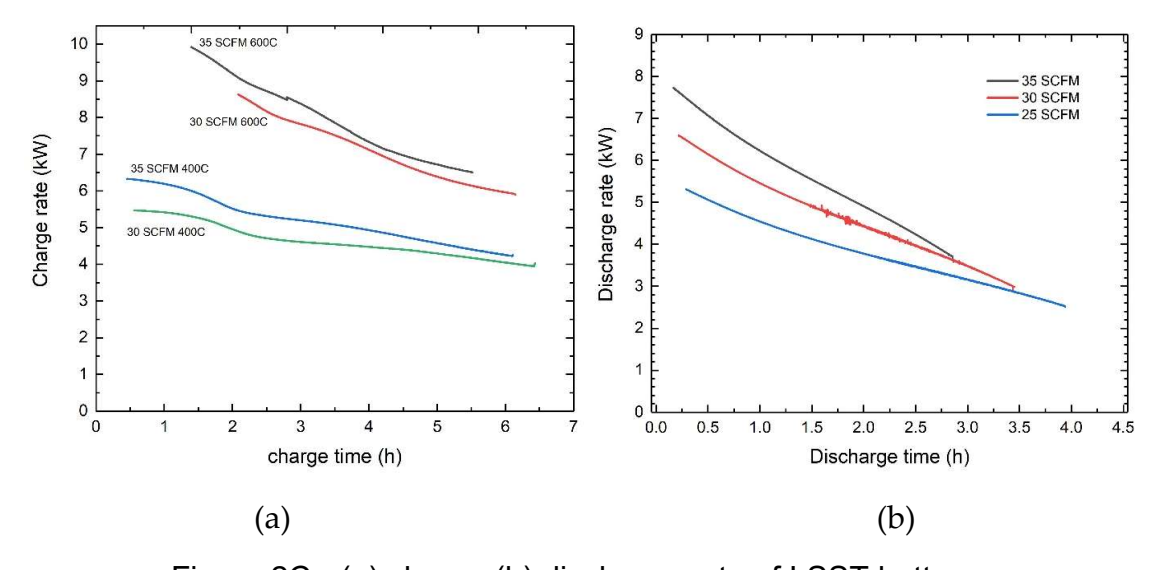


Figure 2C - (a) charge (b) discharge rate of LSST battery

The highest charge rate is around 10kWh and 6.5 kWh with 600°C and 400°C HTF respectively. With Increasing charge time, the system was charged to a higher temperature, where HTF is losing its ability in supplying energy, leading to a decrease in

charge rate. Although, a higher flow rate of HTF leads to a decrease in residence time, a higher charge rate was still attained compared to lower flow rate at both inlet temperatures due to higher rate of energy supply. At the beginning of charging process, there was a time period when temperature of HTF rise from room temperature to desired 600°C or 400°C. Therefore, the charge rate and following exergetic efficiency of charging are shown after the HTF temperature reaches desired values.

The highest discharge rate is around 8kW, with the highest flow rate, and can drop to around 4kW. Similar to the charging process, the discharge rate is higher with higher flow rate

Exergetic efficiency

The exergetic efficiency of each charging condition was also captured during the experiment.

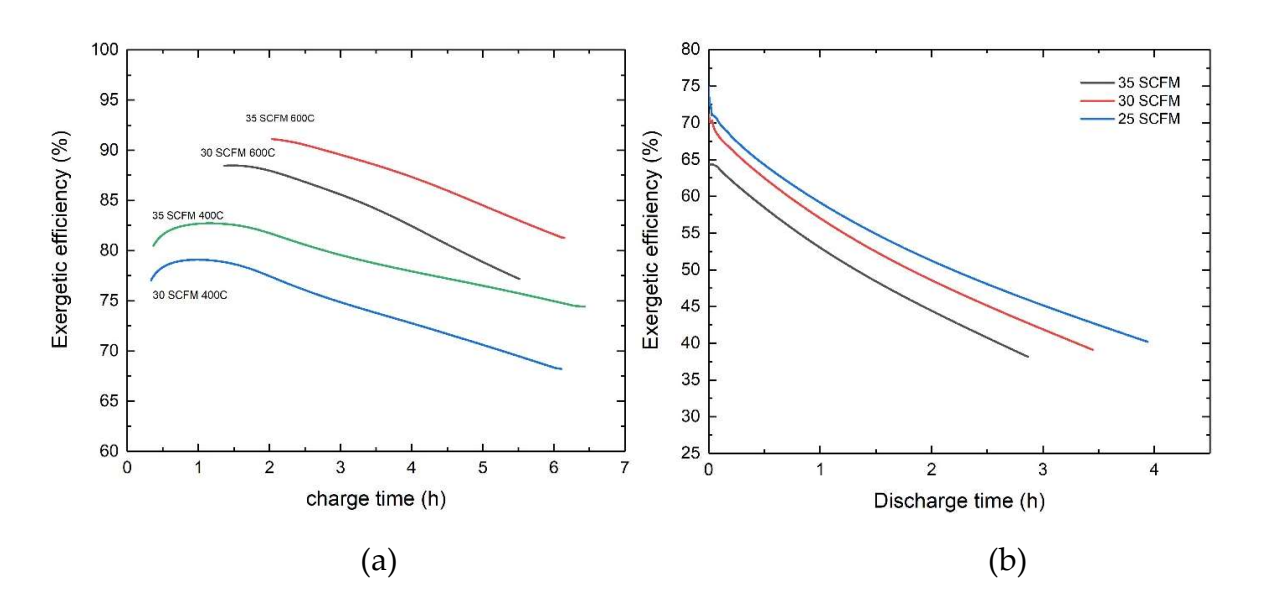


Figure 3C - Exergetic efficiency during (a) charging (b) discharging

According to Fig.3C (a), the highest exergetic efficiency during charging is around 90% and drops to around 80% with 600°C HTF. With 400°C HTF, it is between 85% to 70%. As seen from Fig.3C (b), the highest exergetic efficiency during discharging is around 75% and drops to around 40%. The exergetic efficiency decreased during charging/discharging process because less exergy could be absorbed by the system while the system temperature was approaching charging/discharging temperature. It is observed that a lower charging temperature yields lower exergetic efficiency initially, because HTF carried less exergy so that same amount of exergy destruction by pump work occupied larger portion of the total exergy. But at the end of the charging process, it intersects with the one obtained by higher charging temperature with higher flow rate

of HTF. This is due to larger exergy destruction from higher pump work associate with higher flow rate.

To demonstrate the effect of pump work on exergetic efficiency in current scaled system, the exergetic efficiency is calculated excluding the exergy destruction. Fig.4C (a) and (b) show exergetic efficiencies during charge/discharge without considering pump work.

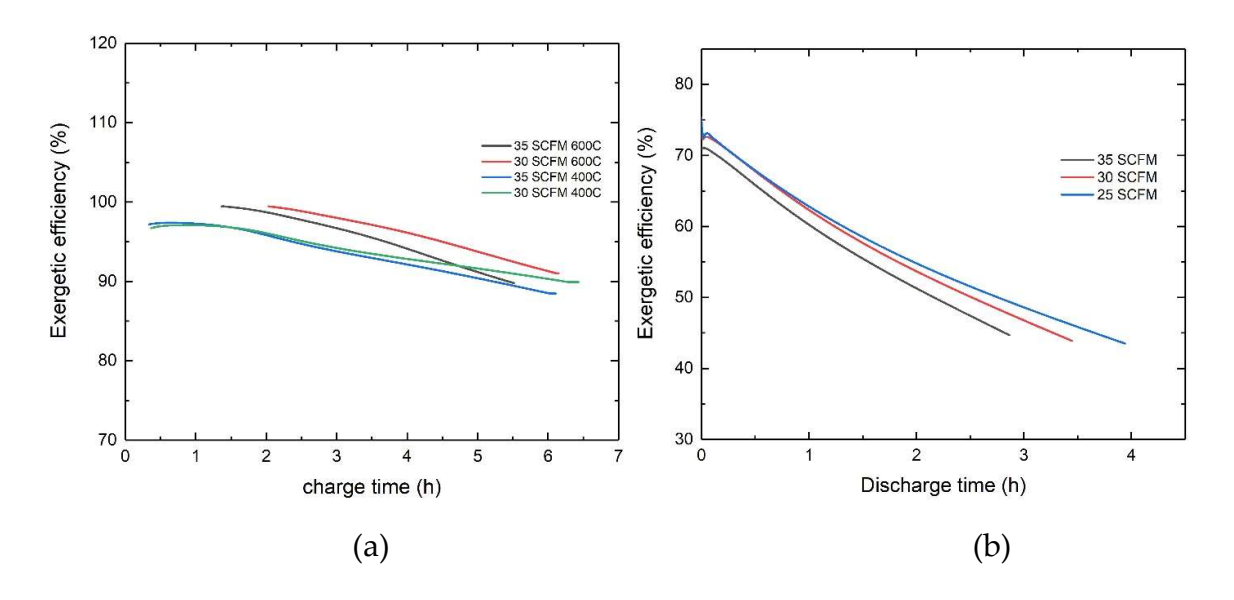


Figure 4C - Exergetic efficiency without pump work during (a) charging, (b) discharging

Without considering exergy destruction due to pump work, charge exergetic efficiencies of different test cases fall much closer to each other with initial values near 100%. This is because initially, without significant heat loss, system exergy should be the same as exergy supplied by HTF. During discharging, gaps between exergetic efficiencies of all three cases are reduced significantly as well. According to the definition,

without pump work, $\dot{m}_{f,d}$ cancels out, so that exergetic efficiency during discharging only depends on $T_{f,out}$. If each discharging case started when the system was charged to the same state, their exergetic efficiencies should share the same initial value. However, exergetic efficiency still decreases faster with higher discharge flow rate because $T_{f,out}$ decreases faster. Therefore, the flow rate still indirectly affects the exergetic efficiency but to a much lower extend.

It is concluded that in the LSST, the pump work plays significant role when considering exergetic efficiency as a performance parameter. Therefore, monotonically increasing the flow rate of HTF is not ideal when exergetic efficiency needs to be maintained high for a long period of time.

Roundtrip efficiency

The roundtrip efficiency during discharging was estimated by summing all energy carried out from the system by HTF and divided by the total energy of the system before the discharging process starts. Fig.5C shows the roundtrip efficiencies of three conditions with different discharge flow rates.

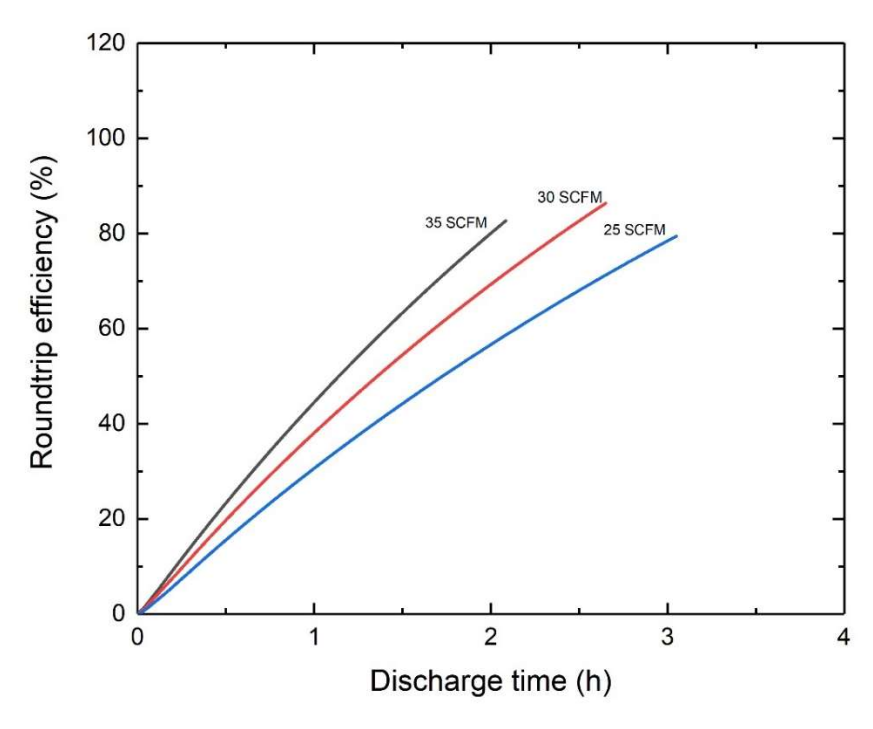


Figure 5C - Roundtrip efficiency during discharging

Since the system is charged and discharged to similar temperature for all conditions, their roundtrip efficiencies reach similar values of around 80%. A higher flow rate leads to a steeper increase of the roundtrip efficiency because a higher discharge rate carries out energy faster. Due to complexity of the system, system temperature can only be estimated by temperature measurements at limited locations. Therefore, there are uncertainties exist in the estimated total system energy which is highly likely to be lower than reality that yields a higher roundtrip efficiency. But the trend and influence of the flow rate on such performance parameter is believed to be valid.

Appendix D: On-sun pilot demonstration of SulfurTES system

The on-sun demonstration is in a similar configuration as lab-scale demonstration but higher in the storage capacity. 4-inch tubes are used as sulfur container with 1 meter in length. One prominent difference compared to lab-demonstration is the incorporation of longitudinal baffle that extends from one end to the other crossing all latitudinal baffles (Fig 1D (b)), shown in Fig 1D (c). The assembled tube bundle is seen in Fig 1D (d).

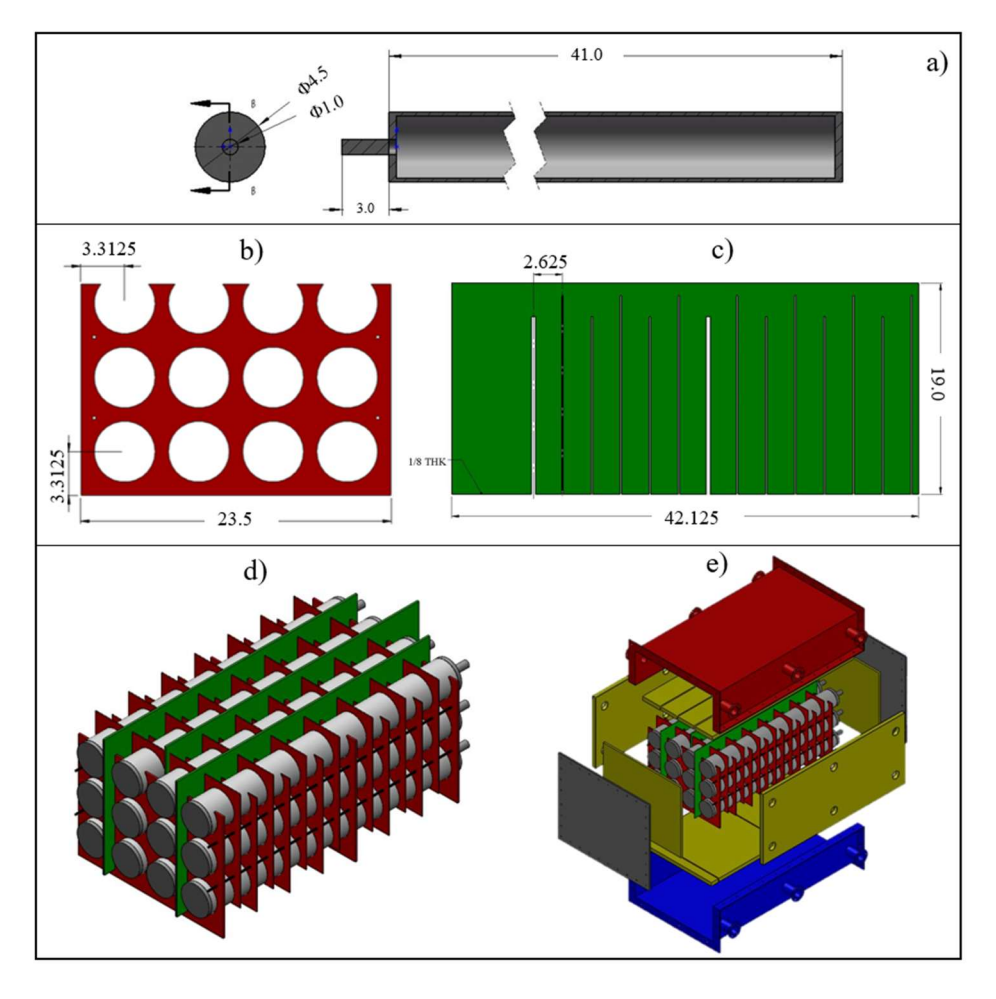


Figure 1D - Pilot demonstration system design

The incorporation of longitudinal baffle provides an additional measure in flow separation that increases the flow velocity, which leads to enhanced shell side heat transfer performance and overall system performance.

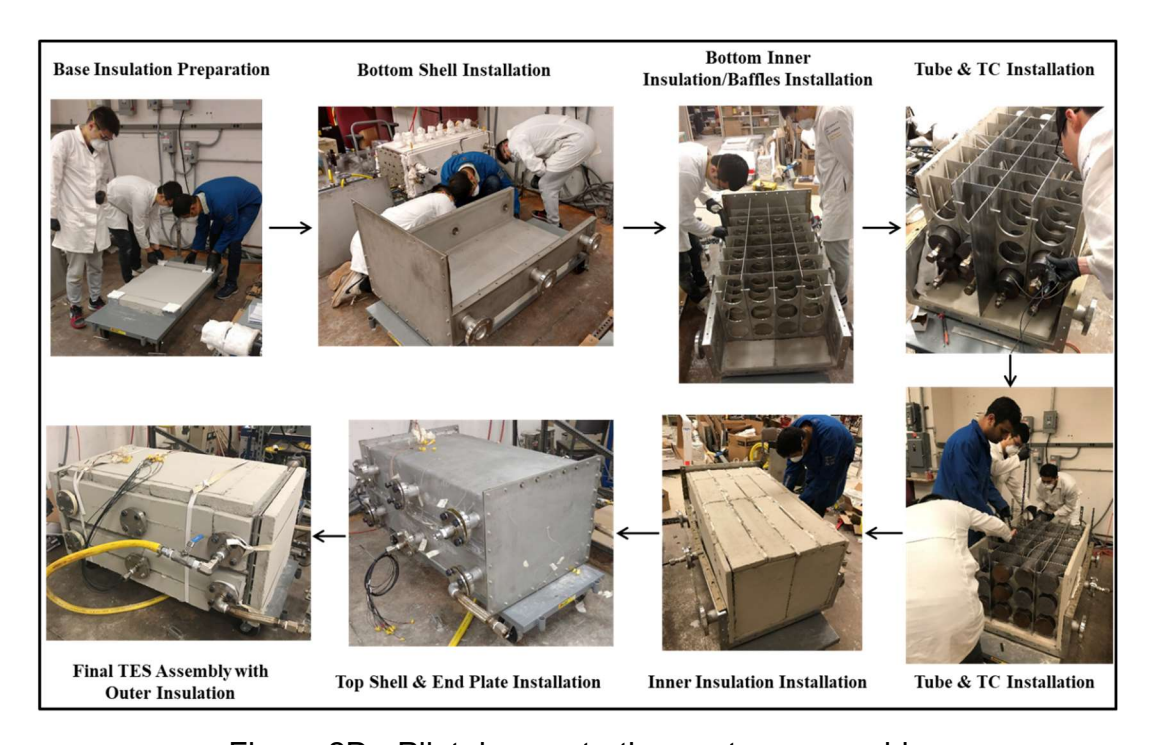


Figure 2D - Pilot demonstration system assembly

The process of system assembly is presented in Fig 2D. It begins by applying a layer of insulation on the bottom of lower shell. Then, both latitudinal and longitudinal baffles are laid on the bottom shell. Tubes are insert into baffle holes and covered by a layer of inner insulation. The system is closed by installing the top shell. Finally, the entire system is covered by another outer layer of insulation to minimize heat loss.

Thermocouples are welded at various locations within the tube bundle to capture axial temperature variation during experiment.



Figure 3D - Parabolic dish collector by TSS,Inc.

The parabolic solar dish collector is provided by TSS,Inc, shown in Fig 3D. the parabolic dish is installed on a circular track. A solar irradiation sensor and a motor compose the control and actuation system that ensures the solar collector is always directly pointing to the sun during operation. A heat receiver is hanging at the focal point of the collector. Cold air is supplied to the receiver to capture the heat, and flow into SulfurTES for during charging.

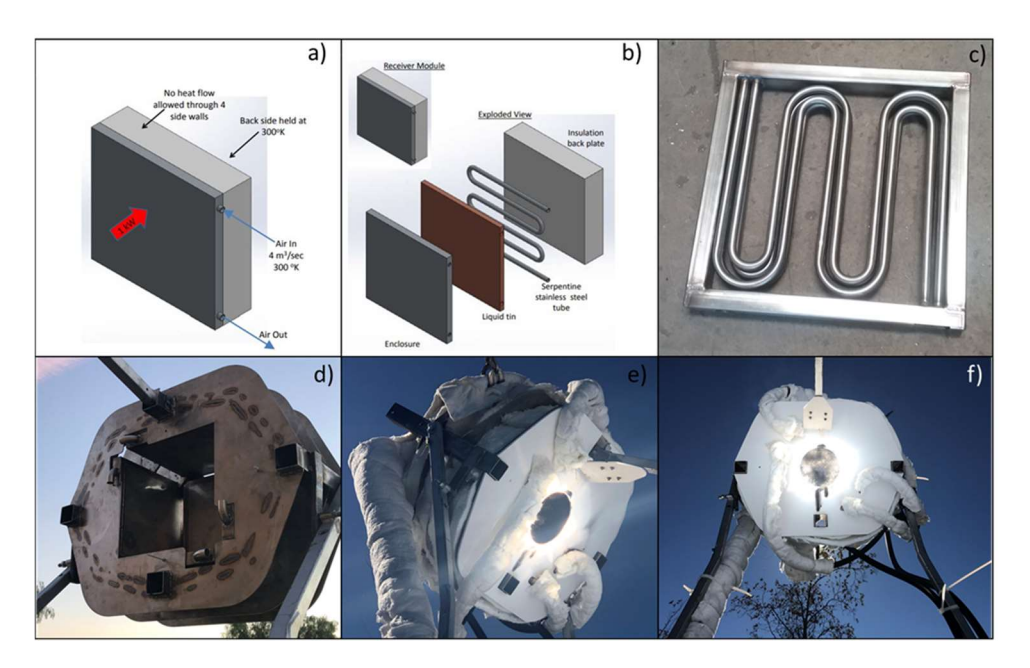


Figure 4D - Receiver design and assembly

The receiver is composed by 5 rectangular panels, each embedded with two parallel HTF pipes, shown in Fig 4D. During operation, the solar irradiation will be reflected into the hole on the front surface of receiver, heating up the cavity between 5 panels, and consequently, the air flowing within each panel.

An air conduit is routed from the receiver to the charging inlet of SulfurTES. The air conduit is anchored along the supporting structure of receiver, so it moves along with the receiver without entanglement. A heavy layer of insulation is also applied to the conduit to minimize heat loss. Fig 5D presents the completed test setup after connecting SulfurTES with the dish collector.



Figure 5D - SulfurTES integrated with dish collector

Fig 6D shows the team members who dedicated time and effort in achieving the successful demonstration, from both UCLA energy and innovation lab and TSS,Inc. From left to right: Mr. Kaiyuan Jin, Mr. Yide Wang, Professor Richard Wirz, Mr. Stephen Wyle, Dr. Amey Barde, Dr. Alan Spero,



Figure 6D - Project team

References

- 1. Rauser, Casandra, et al. "Southern California Clean Energy Innovation Ecosystem Roundtable Report." (2016).
- 2. Stekli J, Irwin L, Pitchumani R. Technical Challenges and Opportunities for Concentrating Solar Power With Thermal Energy Storage. ASME. J. Thermal Sci. Eng. Appl. 2013;5(2):021011-021011-12. doi:10.1115/1.4024143.
- 3. Clark, P.D. and N.I. Dowling, Capture of solar energy using elemental sulfur. Journal of Sulfur Chemistry, 2004. 25(1): p. 7-11.
- 4. Wirz, R., E., Stopin, A., P., P., Louis, A., T., Lavine, A., G., Kavehpour, H., P., Lakeh, R., B., Furst, B., I., Bran, G. and Garcia-Garibay, M., A., The Regents Of The University Of California. High-density, high-temperature thermal energy storage and retrieval, 2014; U.S. Patent Application 14/475,479.
- 5. Turchi, Craig S., Judith Vidal, and Matthew Bauer. "Molten salt power towers operating at 600–650° C: Salt selection and cost benefits." Solar Energy 164 (2018): 38-46.
- 6. Glatzmaier, G. Developing a cost model and methodology to estimate capital costs for thermal energy storage. No. NREL/TP-5500-53066. National Renewable Energy Lab. (NREL), Golden, CO (United States), 2011.
- 7. Laing, Doerte, et al. "Test results of concrete thermal energy storage for parabolic trough power plants." Journal of Solar Energy Engineering 131.4 (2009): 041007.
- 8. Mehos, Mark, et al. On the Path to SunShot-Advancing Concentrating Solar Power Technology, Performance, and Dispatchability. No. NREL/TP-5500-65688 SAND-2016-2237 R. EERE Publication and Product Library, 2016.
- 9. Sarbu, Ioan, and Calin Sebarchievici. "A comprehensive review of thermal energy storage." Sustainability 10.1 (2018): 191.
- 10. Raade, Justin W., and David Padowitz. "Development of molten salt heat transfer fluid with low melting point and high thermal stability." Journal of Solar Energy Engineering 133.3 (2011): 031013.
- 11. Zavattoni, S. A., et al. "High temperature rock-bed TES system suitable for industrial-scale CSP plant–CFD analysis under charge/discharge cyclic conditions." Energy Procedia 46 (2014): 124-133.
- 12. Zanganeh, Giw, et al. "Packed-bed thermal storage for concentrated solar power–Pilot-scale demonstration and industrial-scale design." Solar Energy 86.10 (2012): 3084-3098.

- 13. Zanganeh, G., et al. "Design of packed bed thermal energy storage systems for high-temperature industrial process heat." Applied energy 137 (2015): 812-822.
- 14. "Pebble Stone, Pebble Stone Suppliers and Manufacturers at Alibaba.com" Available online: https://www.alibaba.com/showroom/pebble-stone.html
- 15. Yang, Zhen, and Suresh V. Garimella. "Thermal analysis of solar thermal energy storage in a molten-salt thermocline." Solar energy 84.6 (2010): 974-985.
- 16. Xu, Chao, et al. "Sensitivity analysis of the numerical study on the thermal performance of a packed-bed molten salt thermocline thermal storage system." Applied Energy 92 (2012): 65-75.
- 17. Sharma, A.; Tyagi, V.V.; Chen, C.R.; Buddhi, D. Review on thermal energy storage with phase change materials and applications. Renew. Sustain. Energy Rev. 2009, 13, 318–345.
- 18. Abhat, A. Development of a modular heat exchanger with integrated latent heat storage. In Germany Ministry of Science and Technology Bonn; Report No. BMFT FBT 81-050; Institut fuer Kemtechnik und Energiewandlung e.V.: Stuttgart, Germany, 1981.
- 19. Ge, H.; Li, H.; Mei, S.; Liu, J. Low melting point liquid metal as a new class of phase change material: An emerging frontier in energy area. Renew. Sustain. Energy Rev. 2013, 21, 331–346.
- 20. Su,W.; Darkwa, J.; Kokogiannakis, G. Review of solid–liquid phase change materials and their encapsulation technologies. Renew. Sustain. Energy Rev. 2015, 48, 373–391.
- 21. Sharma, R.K.; Ganesan, P.; Tyagi, V.V.; Metselaar, H.S.C.; Sandaran, S.C. Developments in organic solid–liquid phase change materials and their applications in thermal energy storage. Energy Convers. Manag. 2015, 95,193–228.
- 22. K. Nithyanandam and R. Pitchumani, "Cost and performance analysis of concentrating solar power systems with integrated latent thermal energy storage," Energy, vol. 64, pp. 793–810, Jan. 2014.
- 23. Agyenim, Francis, Philip Eames, and Mervyn Smyth. "Heat transfer enhancement in medium temperature thermal energy storage system using a multitube heat transfer array." Renewable energy 35.1 (2010): 198-207.
- 24. Gharebaghi, Maryam, and I. Sezai. "Enhancement of heat transfer in latent heat storage modules with internal fins." Numerical Heat Transfer, Part A: Applications 53.7 (2007): 749-765.
- 25. Bai, F., et al. "Economic evaluation of shell-and-tube latent heat thermal energy storage for concentrating solar power applications." Energy Procedia 69 (2015): 737-747.

- 26. Kerskes, H.; Mette, B.; Bertsch, F.; Asenbeck, S.; Drück, H. Chemical energy storage using reversible solid/gas-reactions(CWS)—Results of the research project. Energy Procedia 2012, 30, 294–304.
- 27. Fujii, I.; Tsuchiya, K.; Higano, M.; Yamada, J. Studies of an energy storage system by use of the reversible chemical reaction: CaO + H2O\$Ca(OH)2. Sol. Energy 1985, 34, 367–377.
- 28. Lavine, Adrienne S., et al. "Thermochemical energy storage with ammonia: Aiming for the sunshot cost target." AIP Conference Proceedings. Vol. 1734. No. 1. AIP Publishing, 2016.
- 29. Chen, Chen, et al. "Design and optimization of an ammonia synthesis system for ammonia-based solar thermochemical energy storage." Solar Energy 159 (2018): 992-1002.
- 30. Jin, K.J "Thermofluidic characterization of sulfur-based thermal energy storage system". Diss. UCLA, 2019.
- 31. Tuller, W., Freeport Sulphur Company. The sulphur data book. McGraw-Hill book company, Inc., 1954.
- 32. Wirz, Richard E., et al. "Thermal Energy Storage with Supercritical Fluids." Final Scientific/Technical Report, DE-AR0000140,2016
- 33. Wirz, Richard E., et al. "Low-Cost Thermal Energy Storage for Dispatchable CSP." Final project report, California Energy Commission, 2018
- 34. Nithyanandam, K., et al. "Charge and discharge behavior of elemental sulfur in isochoric high temperature thermal energy storage systems." Applied Energy 214 (2018): 166-177.
- 35. Barde, Amey, et al. "Demonstration of a low cost, high temperature elemental sulfur thermal battery." Applied Thermal Engineering 137 (2018): 259-267.
- 36. T. E. W. Schumann, "Heat transfer: A liquid flowing through a porous prism," *J. Frankl. Inst.*, vol. 208, no. 3, pp. 405–416, Sep. 1929.
- 37. M. Lacroix, "Numerical simulation of a shell-and-tube latent heat thermal energy storage unit," Sol. Energy, vol. 50, no. 4, pp. 357–367, Apr. 1993.
- 38. A. Modi and C. D. Pérez-Segarra, "Thermocline thermal storage systems for concentrated solar power plants: One-dimensional numerical model and comparative analysis," Sol. Energy, vol. 100, pp. 84–93, Feb. 2014.
- 39. C. Xu, Z. Wang, Y. He, X. Li, and F. Bai, "Parametric study and standby behavior of a packed-bed molten salt thermocline thermal storage system," Renew. Energy, vol. 48, pp. 1–9, Dec. 2012.

- 40. G. Angelini, A. Lucchini, and G. Manzolini, "Comparison of Thermocline Molten Salt Storage Performances to Commercial Two-tank Configuration," Energy Procedia, vol. 49, pp. 694–704, Jan. 2014.
- 41. S. S. Mostafavi Tehrani, R. A. Taylor, K. Nithyanandam, and A. Shafiei Ghazani, "Annual comparative performance and cost analysis of high temperature, sensible thermal energy storage systems integrated with a concentrated solar power plant," Sol. Energy, vol. 153, pp. 153–172, Sep. 2017.
- 42. Strasser, Matthew N., and R. Paneer Selvam. "A cost and performance comparison of packed bed and structured thermocline thermal energy storage systems." Solar Energy 108 (2014): 390-402.
- 43. Mahfuz, M. H., et al. "Performance investigation of thermal energy storage system with Phase Change Material (PCM) for solar water heating application." International Communications in Heat and Mass Transfer 57 (2014): 132-139.
- 44. "Tubular Exchanger Manufacturers Association, Inc (TEMA)." [Online]. Available: http://www.tema.org/. [Accessed: 06-Dec-2018].
- 45. J. Taborek, Shell-and-tube heat exchangers, Heat Exchanger Design Handbook, vol. 3. New York, NY: Hemisphere Publishing Corporation, 1988.
- 46. T. L. Bergman, F. P. Incropera, D. P. DeWitt, and A. S. Lavine, Fundamentals of Heat and Mass Transfer. John Wiley & Sons, 2011.
- 47. S. Patankar, Numerical Heat Transfer and Fluid Flow. 1980.
- 48. J. Taborek, Shell-and-tube heat exchangers, Heat Exchanger Design Handbook, vol. 3. New York, NY: Hemisphere Publishing Corporation, 1988.
- 49. Bell, K., Chisholm, D., and Cooper, A., 1983, Heat Exchanger Design Handbook, Hemisphere Publishing Corporation.
- 50. K. Nithyanandam, A. barde, and W. Richard, "Heat Transfer Behavior of Elemental Sulfur for Low Temperature Thermal Energy Storage Applications," 2017.
- 51. "NIST Chemistry WebBook, Standard Reference Database Number 69." [Online]. Available: https://webbook.nist.gov/chemistry/.
- 52. "Stainless Steel Grade 316 (UNS S31600)," 2018. [Online]. Available: https://www.azom.com/properties.aspx?ArticleID=863.
- 53. R. A. W. M. Henkes, F. F. Van Der Vlugt, and C. J. Hoogendoorn, "Natural-convection flow in a square cavity calculated with low-Reynolds-number turbulence models," Int. J. Heat Mass Transf., vol. 34, no. 2, pp. 377–388, Feb. 1991.
- 54. M. A. Rosen, "Appropriate Thermodynamic Performance Measures for Closed Systems for Thermal Energy Storage," J. Sol. Energy Eng., vol. 114, no. 2, pp. 100–105, May 1992.

- 55. M. Shinn, K. Nithyanandam, A. Barde, and R. E. Wirz, "Sulfur-based thermal energy storage system using intermodal containment: Design and performance analysis," *Appl. Therm. Eng.*, vol. 128, pp. 1009–1021, Jan. 2018.
- 56. S. Jegadheeswaran, S. D. Pohekar, and T. Kousksou, "Exergy based performance evaluation of latent heat thermal storage system: A review," Renew. Sustain. Energy Rev., vol. 14, no. 9, pp. 2580–2595, 2010.
- 57. R. Domański and G. Fellah, "EXERGY AS A TOOL FOR DESIGNING AND OPERATING THERMAL STORAGE UNITS," J. Power Technol., vol. 81, no. 0, pp. 23–45, 1995.
- 58. M. J. N. Wills, D. Johnston, and A. E. R. E. Harwell, "A new and accurate hand calculation method," in 22nd National Heat Transfer Conference, HTD, vol. Vol. 36.
- 59. Thulukkanam, Kuppan. Heat exchanger design handbook. CRC press, 2013.
- 60. Desu, Raghuram Karthik, et al. "Mechanical properties of Austenitic Stainless Steel 304L and 316L at elevated temperatures." Journal of Materials Research and Technology 5.1 (2016): 13-20.
- 61. Nederstigt, Pim. "Real Gas Thermodynamics: and the isentropic behavior of substances." (2017).
- 62. Wright, Steven A., et al. "Operation and analysis of a supercritical CO2 Brayton cycle." Sandia Report, No. SAND2010-0171 (2010).
- 63. Rochau, G. E., Pasch, J. J., Cannon, G., Carlson, M., Fleming, D., Kruizenga, A., ... & Cycles, S. C. B. NP-NE Workshop# 2–August 4, 2014.
- 64. Gong, Y., and I. A. Matthews. "Tropical Report: Analysis of radial compressor options for supercritical CO2 power conversion cycle." Report No: MIT-GFR-034 (2006).
- 65. Dostal, Vaclav, Michael J. Driscoll, and Pavel Hejzlar. A supercritical carbon dioxide cycle for next generation nuclear reactors. Diss. Massachusetts Institute of Technology, Department of Nuclear Engineering, 2004.
- 66. Angelino, Gianfranco. "Carbon dioxide condensation cycles for power production." Journal of Engineering for Power 90.3 (1968): 287-295.
- 67. Ranjan, Devesh. Fundamental study of key issues related to advanced sCO2 Brayton cycle: Prototypic HX development and cavitation. No. 14-6670. Georgia Inst. of Technology, Atlanta, GA (United States), 2018.
- 68. Iverson, Brian DeVon, Joseph Gabriel Cordaro, and Alan Michael Kruizenga. Thermal property testing of nitrate thermal storage salts in the solid phase. No. SAND2011-3710C. Sandia National Lab. (SNL-NM), Albuquerque, NM (United States); Sandia National Laboratories, Livermore, CA, 2011.
- 69. Herrmann, Ulf, Bruce Kelly, and Henry Price. "Two-tank molten salt storage for parabolic trough solar power plants." Energy 29.5-6 (2004): 883-893.

- 70. Pacheco, James E., et al. "Final test and evaluation results from the solar two project." Report No. SAND2002-0120, Sandia National Laboratories, Albuquerque, NM 45 (2002).
- 71. "Coastal Hitec Heat Transfer Salt", Coastal Chemical Co., L.L.C. Available: http://stoppingclimatechange.com/MSR%20-%20HITEC%20Heat%20Transfer%20Salt.pdf
- 72. "System Advisor Model (SAM)", National Renewable Energy Laboratory. Available: https://sam.nrel.gov/
- 73. Biencinto, Mario, et al. "Simulation and assessment of operation strategies for solar thermal power plants with a thermocline storage tank." Solar Energy 103 (2014): 456-472.
- 74. Kumana, Jimmy D. "Essentials of Steam Turbine Design and Analysis." Chemical Engineering Progress 114.8 (2018): 29-37.
- 75. R. Don, "Foundations for Cylindrical Storage Tanks," Int. Soc. Soil Mech. Geotech. Eng., 1961.
- 76. PENN STAINLESS, "Budget quote," 10-Apr-2017.
- 77. U.S. Bureau of Labor Statistics, "Producer Price Index by Commodity for Metals and Metal Products: Cast Iron Scrap," FRED, Federal Reserve Bank of St. Louis, 01-Dec-1986. [Online]. Available: https://fred.stlouisfed.org/series/WPU101213.
- 78. "SS304 Tube, SS304 Tube Suppliers and Manufacturers" at Alibaba.com,2019 [Online], https://www.alibaba.com/showroom/ss304+tube.html?fsb=y&IndexArea=product_e n&CatId=&SearchText=ss304+tube&isGalleryList=G
- 79. "Intermodal Container, Intermodal Container Suppliers and Manufacturers at Alibaba.com" Alibaba, 2018. [Online], Available: https://www.alibaba.com/showroom/intermodal+container&isGalleryList=G
- 80. "DFMA Product Costing and Simplification." [Online]. Available: https://www.dfma.com
- 81. "System Advisor Model (SAM)", National Renewable Energy Laboratory. [Online]. Available: https://sam.nrel.gov/
- 82. Schuknecht, Nathan, Jennifer McDaniel, and Harrison Filas. "Achievement of the \$100/m2 parabolic trough." AIP Conference Proceedings. Vol. 2033. No. 1. AIP Publishing, 2018.
- 83. Turchi, C., Mehos, M., Ho, C. K., and Kolb, G. J., 2010, "Current and future costs for parabolic trough and power tower systems in the US market," SolarPACES 2010.

- 84. "The Sunshot 2030 Goals" U.S. Department of Energy. [Online]. Available: https://www.energy.gov/sites/prod/files/2018/05/f51/SunShot%202030%20Fact%20Sheet.pdf
- 85. Parthiv Kurup, Craig S. Turchi, "Parabolic Trough Collector Cost Update for the System Advisor Model (SAM)", National Renewable Energy Laboratory, Task No. CP13.3510, 2015.